CFD simulation to analyze the added mass and drag behavior of a semi-submersible wind turbine floater when subjected to a forced oscillatory motion.

Santiago Salcedo Velasquez

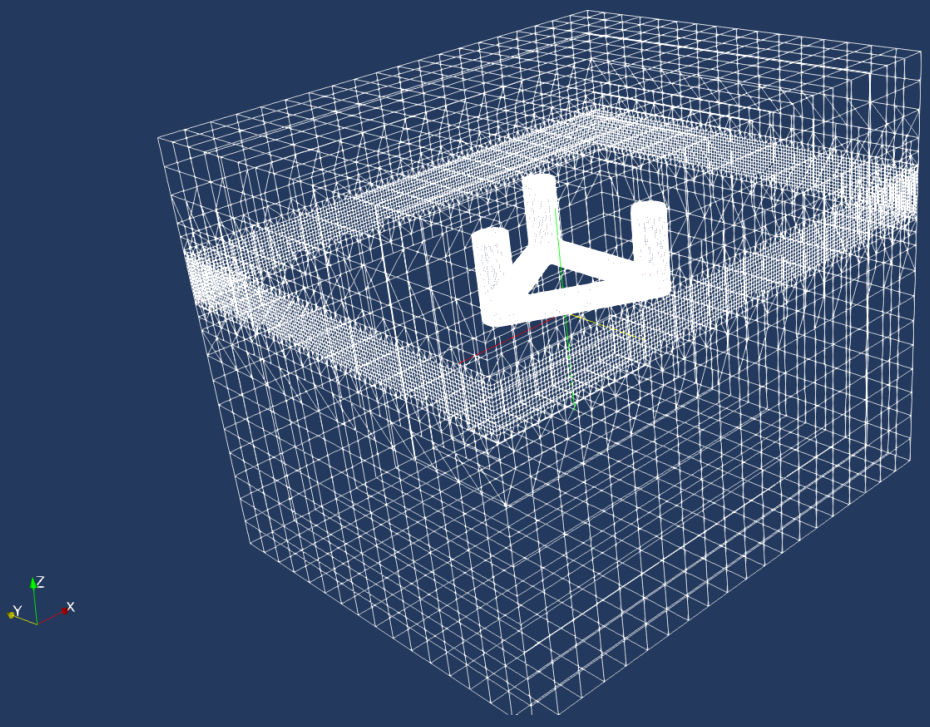

TU Delft

CFD simulation to analyze the added mass and drag behavior of a semi-submersible wind turbine floater when subjected to a forced oscillatory motion.

Thesis report

by

Santiago Salcedo Velasquez

to obtain the degree of Master of Science
at the Delft University of Technology
to be defended publicly on October 24, 2023 at 12:00

Thesis committee:

Chair:	Dr. Axelle Viré
Supervisors:	Dr. Likhitha Ramesh Reddy
	Dr. Axelle Viré
External examiner:	Dr. Oriol Colomés Gené
Place:	Faculty of Aerospace Engineering, Delft
Project Duration:	November, 2022 - October, 2023
Student number:	5455103

Faculty of Aerospace Engineering · Delft University of Technology

Preface

This master's thesis marks the end of my studies in Sustainable Energy Technology at the Technical University of Delft. Throughout my academic journey, I've been deeply passionate about sustainability and the role of renewable technologies in addressing the global challenge of the energy transition. This thesis represents my commitment to advancing our understanding of sustainable energy solutions. The path to completing this research was not without its challenges, but through these obstacles, I experienced significant personal and academic growth. With the support of my friends and family, I persisted through the demanding phases of this project.

I am particularly grateful to my supervisor, PhD. Likhitha Ramesh Reddy, for her invaluable guidance and support throughout the thesis journey. Her feedback and insights played an essential role in shaping this research. I thank Dr. Axelle Vire for chairing the committee and her supervision. I am also grateful to Dr. Oriol Colomes Gene for being part of the committee. Lastly, I want to express my deepest gratitude to my friends and family, especially Alejandro, Sebastian, and my parents, for their unconditional support and encouragement. Their belief in my capabilities has been a driving force in my academic pursuits.

Santiago Salcedo Velasquez
Delft, 2023

Abstract

Sustainable and renewable energies are essential in achieving climate targets set by the Paris Agreement and Sustainable Development Goals (SDGs). Floating offshore wind turbines (FOWTs) represent an innovative technology with considerable potential to contribute to these goals. However, being a relatively new technology, FOWTs pose challenges that must be addressed to enhance their development. To speed up FOWT installation and optimize their design, accurate numerical simulation tools are essential, particularly mid-fidelity models, which use less computational time but require precise hydrodynamic characteristics to be tuned. These tuning parameters are obtained with experimental tests or with Computational Fluid Dynamics (CFD) simulations.

This thesis aims to analyze the added mass and drag coefficients of the MaRINET2 semi-submersible wind turbine floater when subjected to forced oscillatory motion, utilizing a validated CFD model. To achieve the objective, a nonlinear Navier Stokes numerical model was developed within the open-source CFD software OpenFOAM. The interFoam solver was employed for the simulations. A mesh convergence study identified an optimal mesh configuration, balancing computational efficiency with result accuracy. Two types of simulations were conducted: free decay simulations for model validation against University of Strathclyde (UoS) experimental data and forced oscillatory simulations to compute added mass and drag coefficients under varying oscillation parameters.

It was found that heave added mass is sensitive to both oscillation amplitude and period, while heave drag coefficients displayed minimal influence at shorter periods. For high-amplitude oscillations, surge drag coefficients remained stable across oscillation periods, yet longer periods increased coefficients for mid and low amplitudes. Pitch added mass coefficients remained unaffected by oscillation amplitude but increased with longer periods. Comparing these hydrodynamic parameters with two reference papers revealed both similarities and discrepancies in trends. It is challenging to attribute these discrepancies only to floater geometry due to the lack of specific experimental data for this floater.

Keywords
Semi-submersible floater, FOWTs, CFD, added mass, drag coefficients, free decay simulations, forced oscillations simulations, OpenFOAM, MaRINET2 semi-submersible.

Contents

Nomenclature

List of Abbreviations

3DOF	Three Degrees of Freedom
6DOF	Six Degrees of Freedom
CFD	Computational Fluid Dynamics
CoB	Center of Buoyancy
CoM	Center of Mass
DES	Detached Eddy Simulations
DNS	Direct Numerical Solution
FLS	Fatigue Limit State
FOWT	Floating Offshore Wind Turbine
GHG	Green House Gases
GWEC	Global Wind Energy Council
IEA	International Energy Agency
LES	Large Eddy Simulation
LWT	Linear Wave Theory
MULES	Multidimensional Universal Limiter for Explicit Solution algorithm
NSE	Navier-Stokes equation
OC4	Offshore Code Comparison Collaboration Continuation
OC5	Offshore Code Comparison Collaboration, Continued with Correlation
OC6	Offshore Code Comparison Collaboration, Continued with Correlation, and unCertainty
PFT	Potential Flow Theory
PIMPLE	PISO Multiple Phase Explicit algorithm
PISO	Pressure Implicit with Splitting of Operators
RANS	Reynolds Average Navier-Stokes
RAS	Reynolds-averaged stress
SDG	Sustainable Development Goals
SS	Semi-submersible
SST	Shear Stress Transport
STL	Stereolithography format
SWL	Still Water Level
TLP	Tension Leg Platform
UCC	University College Cork
ULS	Ultimate Limit State
UN	United Nations
UoS	University of Strathclyde
URANS	Unsteady Reynolds Average Navier-Stokes
VOF	Volume of Fluid
WPA	Water-Plane Area

Constants

ρ_w	Density of water 998.6 kg/m^3
g	Gravity 9.81 m/s^2

List of Symbols

α	Scalar function of VOF
λ	Scaling factor
λ	Wavelength
μ	Viscosity
ω	Specific rate of dissipation
ω	Wave angular frequency
ϕ	Pitch angle
ϕ	Velocity potential
ρ	Density
A	Reference Area

A	Wave Amplitude	I_{yy}	y Area moment of inertia
A_s	Water-Plane Area	k	Turbulence kinetic energy
C_a	Added mass coefficient	k	Wavenumber
C_d	Drag coefficient	M_H	Hydrodynamic moment
D	Distance from the CoM to SWL	M_K	Hydrostatic restoring moment
d	Water depth	p	Pressure
F_b	Buoyancy force	t	Time
f_d	Drag force	T_p	Time period
F_H	Hydrodynamic Force	u	Flow velocity
f_i	Inertia Force	V	Volume
F_K	Hydrostatic restoring forces	V_d	Displaced volume
H	Wave height	Z_b	distance form CoB to SWL
h	Height	$\dot{u}$	Flow acceleration
H_s	Significant wave Height	$\mathbf{u}$	Velocity vector
I_y	y Moment of inertia	$\mathbf{u}_r$	Compression velocity

List of Figures

List of Tables

1 Introduction

1.1. Current situation

1.1.1. Climate change and energy transition

Sustainable and renewable energies are key to achieving the Paris Agreement objectives and the Sustainable Development Goals (SDGs). Climate action to stop global warming and the deterioration of the environment is required. Lately, with growing concerns on climate change and environmental impacts, environmental consciousness is growing, leading people and countries to take action towards the energy transition [1]. Some of the actions taken by the United Nations (UN) to reduce global warming and to have a more environmentally friendly development are the Paris Agreement and the SDGs, respectively.

The energy transition aims to shift from conventional fossil fuel-based energy generation to renewable energy generation [2]. The transition represents an ongoing process that needs continuous research and development in several technologies. Solar and wind power generation are among the leading technologies driving this shift. These two innovative technologies offer economically and technically feasible alternatives to traditional fossil fuel-based energy generation [1]. This research project is focused on wind energy, especially in floating offshore wind turbines (FOWTs).

In December 2015, 195 countries adopted the Paris Agreement seeking to create a global framework for reducing greenhouse gases (GHG), cooperate to tackle climate change, and enhance sustainable development [3]. The Paris Agreement treaty strives to limit global mean temperature below 2°C above pre-industrial levels and aims to limit the rise to 1.5°C. The Agreement contains multiple emission reduction scenarios. The most ambitious one being the Net Zero scenario, which is also the desired outcome. At the same time, the UN adopted the SDGs as part of the 2030 agenda for sustainable development. The SDGs are 17 goals that call to action to work towards a sustainable future for all. Goals 7 and 13 focus on ”Affordable and clean energy” and ”Climate action”, respectively [4]. These are two of the main goals calling for action to combat climate change [5].

The Net Zero scenario aims to achieve a balance between the GHG emissions and their removal from the atmosphere, resulting in no net increase in atmospheric GHG concentrations. Figure 1.1, provided by the International Energy Agency (IEA), shows the estimated installed wind energy capacity required to achieve the net zero scenario by 2030. It also shows that a huge capacity increase is necessary to meet this target and also showcases that while onshore installed capacity (light blue) has existed for some time, offshore wind energy (dark blue) is a relatively new technology.

1.1.2. Offshore wind energy and FOWTs

Offshore wind energy is a developing technology with a significant potential to grow. However, nowadays, onshore wind energy has a higher installed capacity. The total wind energy installed capacity by 2021 was 830GW, which 7% corresponds to offshore wind energy [6]. Onshore wind is a mature technology, while offshore wind is a relatively new technology with promising expansion expectations. This is shown

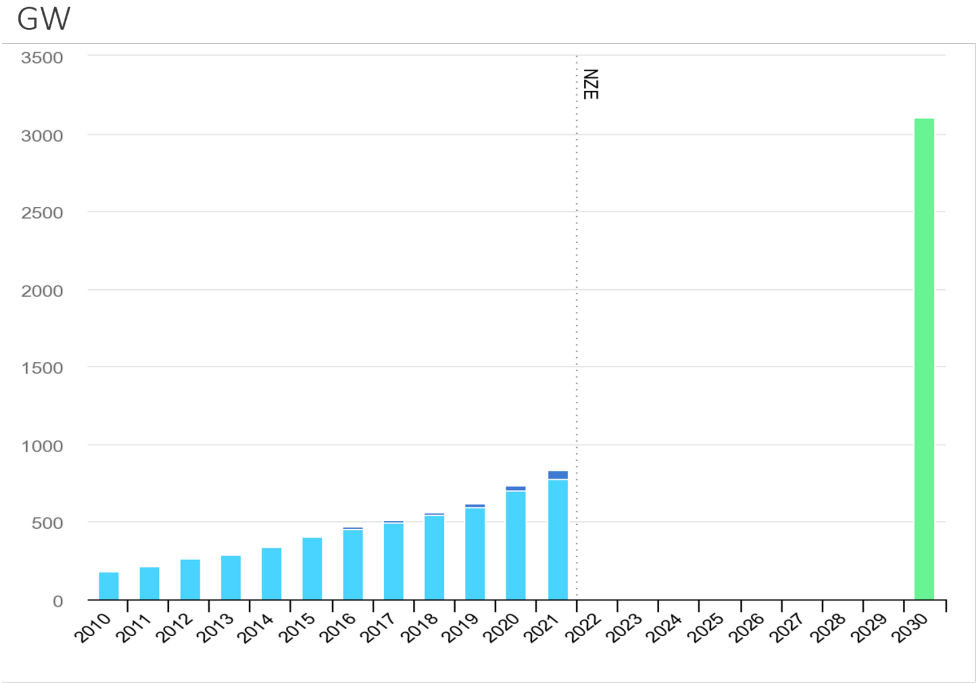

Figure 1.1: Wind power capacity in the Net Zero Scenario, 2010-2030 as of 2022. Taken from [6].

in the Global Wind Report 2022. The report indicates that new offshore wind installations in 2021 were 21.1GW, growing from 6.07GW in 2020. This is also seen in figure 1.2. On the other hand, the new onshore installations decreased from 2021 to 2020 [7, 8]. The two main advantages of offshore wind energy compared to onshore are that there is more space in the sea, and the wind is stronger and more consistent.

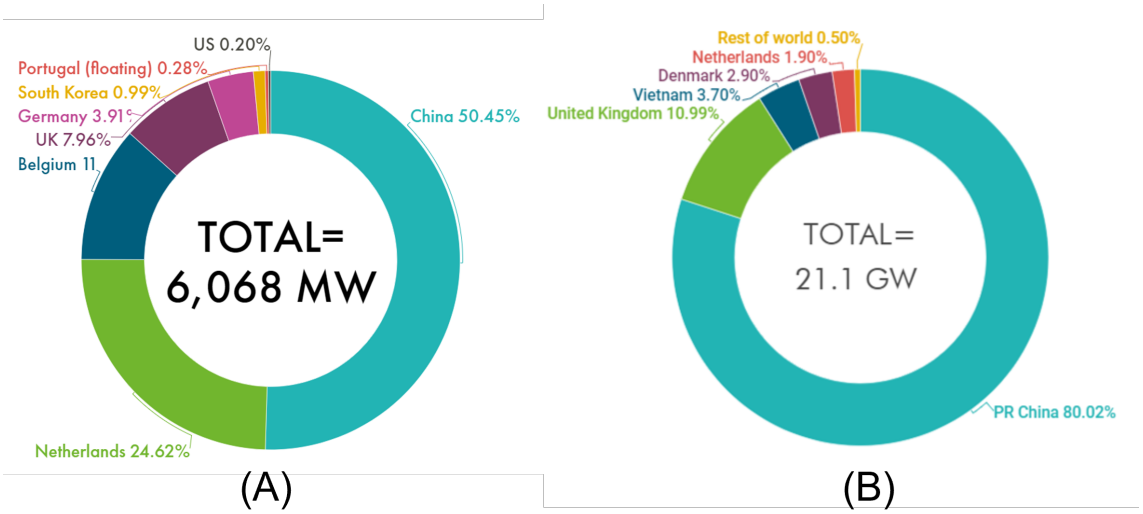

Figure 1.2: New offshore wind installations, (A) 2021, (B) 2022. Taken from [7, 8].

Offshore wind energy is divided into two groups; bottom fixed and floating. The type of foundation defines its classification. Therefore, the wind turbines have either a bottom fixed or a floating foundation. Currently, most offshore wind turbines are bottom fixed. Although floating wind turbines are a relatively new technology with promising growth expectations and several advantages, many challenges need to be solved to become an economically competitive option. The main advantage of FOWTs is that they seem to be the only economically feasible option for harnessing wind energy in deep waters, getting more consistent and faster wind, and not affecting visibility. They are assembled in port and then towed out to the site. This is important since installation in the port is simpler and cheaper [9].

FOWTs still need to solve many challenges. One of them is to accurately estimate the hydrodynamic loading on the floater when influenced by waves. It is important to obtain the hydrodynamic loads properly to compute the Fatigue Limit State (FLS) and the Ultimate Limit State (ULS) to ensure a safe floater design. To obtain the proper hydrodynamic load, the linear and nonlinear physical phenomena need to be considered. Chapter 2, will describe more in detail FOWTs in general and its three existing types.

1.2. Research Motivation

Floating offshore wind turbines (FOWTs) are crucial in the energy transition [1]. The efficient design and reliable performance of FOWTs are key to their success in harnessing wind energy in deep waters. To achieve this, accurate hydrodynamic simulations are needed during the design phase, providing insights into the complex interactions between FOWTs and their dynamic environments.

Numerical models represent a cost-effective and less complex means of collecting hydrodynamic loading and essential floater parameters compared to physical experiments [10]. However, to be truly informative and reliable, numerical models must be validated against experimental data. While full-scale prototype experiments are ideal for validation, their high costs make them rarely used. Instead, model-scale prototypes are often employed, even if they present limitations due to scaling issues [10].

Among the available numerical models, mid-fidelity tools are widely utilized, combining Potential Flow Theory (PFT) with Morison's equation to predict hydrodynamic behavior [11]. These models offer computational efficiency but tend to underestimate loads, particularly with nonlinear effects and low-frequency responses [12]. To optimize mid-fidelity tools, accurate hydrodynamic parameters, such as added mass and drag coefficients, are essential [13]. Calibration of these tools is achieved through experimental data or high-fidelity computational fluid dynamics (CFD) models based on Navier-Stokes equations (NSE). While CFD models provide superior accuracy, they come at the cost of computational complexity and resource intensity [12].

In light of enhancing FOWT installations to support a faster transition to sustainable energy sources, there is a growing demand for validated high-fidelity models. Therefore, the current research is driven by the need for validated high-fidelity models to understand the hydrodynamics in FOWTs and to find the proper hydrodynamic coefficients required to tune mid-fidelity models, ultimately advancing the design and performance of FOWTs.

1.3. Objective & Research Questions

1.3.1. Objective & main research question

Research Objective

The main objective is to analyze the added mass and drag coefficients of the MaRINET2 semi-submersible floater when it is subjected to a forced oscillatory motion with a validated CFD model.

Research Question

How do a semi-submersible floater's added mass and drag coefficients behave and vary under the influence of forced oscillatory motions with different amplitudes and frequencies?

1.3.2. Sub-research questions

To address the main research question and provide a structured understanding of the topic, the two following sub-questions have been formulated to guide the research and provide a clear path toward answering the primary question. Each sub-question has two follow-up questions to provide even more structure to the report.

Research Question 1

How is a CFD model setup and validated to simulate the MaRINET2 semi-submersible floater?

1.1. How are the mooring lines simulated to be able to validate the model?

1.2. How should the mesh be defined for the simulation to be grid-independent and achieve accurate results?

Research Question 2

How are the added mass and drag coefficient obtained from a CFD simulation?

2.1. What type of simulation is required to obtain the hydrodynamic parameters for different amplitudes and frequencies?

2.2. What methodology should be followed to obtain the added mass and drag coefficient from the simulation outcomes?

1.4. Approach

The research study uses the following approach to achieve the main objective and to answer the research questions stated above. First, a literature review is performed to understand which studies on the topic have already been done and to identify knowledge gaps that this thesis is fulfilling. Also, the literature review informs how to undertake the simulations.

Once the background information is known, a CFD model for the semi-submersible is built using the CFD software OpenFOAM to run the simulations. The model is constructed following previous papers and OpenFOAM tutorials. Finally, the model is used to run simulations and obtain the hydrodynamic drag coefficients of the floater.

The intended outcomes of the research study are a validated model and the hydrodynamic added mass and drag coefficients of the MaRINET2 semi-submersible floater. First, the validation is done with free

decay test simulations, which consist of applying an initial offset in different degrees of freedom and letting it decay to the resting position. For this type of simulation, the mooring lines are required. This type of simulation results are compared against a paper to validate the model. Then, the hydrodynamic coefficients are obtained with a different type of simulation. Forced-oscillation simulations are used to calculate the drag coefficient and the added mass. This simulation subjects the floater to an oscillatory motion, and with the results of the forces exerted on the floater, it is possible to calculate the hydrodynamic coefficients desired. This section presented a quick overview of the simulations to understand the approach followed in the report. The report explains each simulation, setup, boundary conditions, initial parameters, and results in detail.

1.5. Structure of the Report

This academic research report is structured as follows:

- Chapter 2 gives an overview of the background theory necessary to achieve the main objective of the research. The chapter provides background knowledge in FOWTs, hydrodynamics, and computational fluid dynamics (CFD).
- Chapter 3 shows the most recent studies of similar or related topics to understand the research gap.
- Chapter 4 shows the numerical model used to calculate the hydrodynamic coefficients and the forces acting on the floater. The chapter explains the numerical model, including the governing equation, the boundary conditions, and the setup of the simulations performed. The chapter also gives a detailed explanation of the Mesh, the mesh generation method used, and a mesh convergence analysis.
- Chapter 5 presents the validation of the model against a paper and the simulation results after the post-processing.
- Chapter 6 presents the conclusion and expresses if the objective is achieved and the research questions answered. In addition, it provides recommendations and gives a path for future work and research.

2

Background Knowledge & Theory

This chapter aims to give an overview of the background theory necessary for achieving the objectives of the research. This chapter helps determine the starting point of the project by providing the background knowledge on the most important aspect of the research in three sections. The first section 2.1 introduces floating offshore wind turbines (FOWT), their types, characteristics, advantages, and disadvantages. Section 2.2 explains the hydrostatics, the waves theory, and the hydrodynamics required for the research. Finally, section 2.3 explains the study's starting point by providing a brief overview of computational fluid dynamics (CFD) and the governing equations used.

2.1. Floating offshore wind turbines (FOWT)

Offshore wind energy is a developing technology with promising expansion expectations, with new wind power installation of 21.1 GW globally in 2021, more than triple compared to 2020 installations [8]. Some of the evident advantages of offshore against onshore wind energy are stronger and more consistent winds in the sea, and there is more space offshore. These two advantages have been the major reasons for the rapid growth of offshore wind. Other reasons such as cost reduction, government support, technological advances, environmental concerns, and market demand have also contributed to the market's rapid growth. Offshore wind energy is now regarded as a competitive technology in electricity generation, expected to be the primary energy carrier by 2025, where it is expected that at least 70% of energy production should come from renewable sources [5].

It is important to distinguish that there are two groups in offshore wind energy; bottom fixed and floating sub-structures. FOWT is a relatively newer technology with optimistic growth expectations and advantages but with challenges. Bottom-fixed offshore wind turbines have one significant limitation; they can not be installed in very deep waters with the current deepest installation being 58.6m [14]. Most of the world's water depths are above 90m; even the North Sea, which is considered relatively shallow, has an average depth of 90m [15]. Therefore, bottom fixed solutions are restrained to a limited area of the sea. A possible alternative to the bottom-fixed offshore wind turbines depth limitation are FOWTs. This section introduces the most important points to consider regarding FOWT, subsection 2.1.1 explains the different mooring systems, and then subsection 2.1.2 presents the current main types of floaters.

2.1.1. Mooring system

FOWTs are anchored to the seabed rather than being fixed on land; these anchors and the lines that connect them to the floater are the mooring systems. This section explains the working principle, the advantages, and the disadvantages of each of the three existing mooring systems; these are shown in figure 2.1. The cost and complexity of the mooring systems depend on two factors, the length of the lines and the type of anchors used [16].

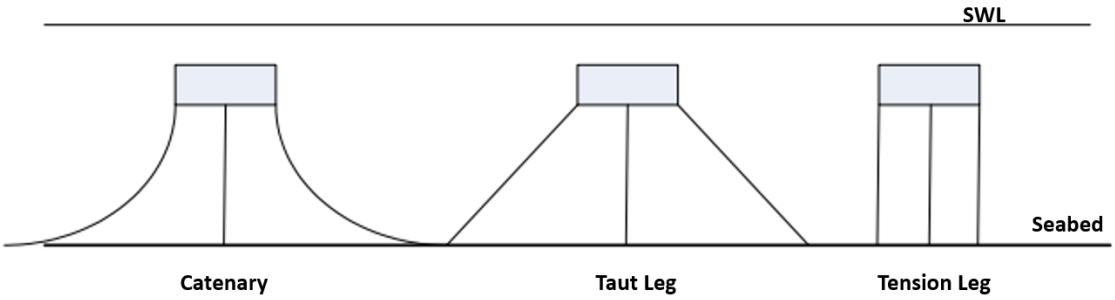

Figure 2.1: Types of mooring systems. Modified from [17].

Catenary mooring lines typically use drag-embedded anchors and are commonly used for semi-submersible platforms and spar buoys. The primary function of this mooring system is to keep the floater in place since the substructures can achieve hydrodynamic stability by themselves [18]. As seen in Figure 2.1, the catenary mooring system has the longest lines of the three options; therefore, the main disadvantage is that it has a large footprint and that the long mooring lines have a high line cost. Another disadvantage is the increased platform dynamics since a large part of the floater is near the SWL [18]. However, the main advantage is that the mooring system experiences only horizontal loads, resulting in simple and low-cost anchors with inexpensive installation and low complexity [17].

The second mooring system is the Taut Leg, considered a middle point or a combination of the other two mooring systems. It is less common than the others since it joins the disadvantages of both. The Taut Leg system needs to resist vertical and horizontal loads, requiring expensive and complex anchors. Also, due to the fact that the mooring lines are not entirely vertical, they are longer and more costly than Tension Leg systems [18, 17].

The third type of mooring system is Tension Leg used in Tension Leg Platforms (TLP). This system normally uses suction pile anchors that support the required vertical loads. This system must maintain constant tension between the anchors and the platform; this exposes it to much higher vertical loads than the other two mooring systems [16]. The advantages of the Tension leg mooring system are that the mooring lines are vertical, resulting in shorter lines, and the platform is more stable in pitch and roll. However, the main disadvantage relies on the requirement to support high vertical loads; therefore, the anchors are complex and costly, sometimes resulting in a higher overall cost, especially in shallow waters [17].

The second component of the mooring system is the anchors. There are different types of anchors, including but not limited to suction piles, drag-embedded, and driven piles. Several types of anchors work with more than one mooring system. A detailed explanation of each anchor is possible; however, it is out of the scope of this research and hence not detailed here.

2.1.2. Type of wind turbines floaters

FOWTs consist of three main components, the wind turbines, the floater, and the mooring system. There are many floater designs and prototypes in the market, yet they can be classified into three main groups based on their primary physical principle of achieving static stability [16]. Figure 2.2 shows the three groups, these are Spar Buoy, Semi-submersible (SS), and TLP from left to right. The perfect floater doesn't exist, but each has several advantages and disadvantages. The benefits translate into complexity and cost reduction, while the disadvantages are the technical limitations of each technology. In the following section, the three types will be analyzed, describing the main characteristics, advantages, disadvantages, and limitations of each one.

Figure 2.2: Type of wind turbines floaters, Spar Buoy, Semi-submersible, and Tension Leg Platform. Taken from [19].

Spar Buoy:
Spar buoys floaters/foundations are relatively long and narrow vertical cylinders, as shown in 2.2, with length/height above 100m and diameters above 10m [20, 21]. Most of the structure is under Still Water Level (SWL). The spar buoys use ballast as the primary physical static stability principle; this means that the center of gravity is below the center of buoyancy, creating resistance against overturning moments [18]. Having the center of gravity below the center of buoyancy is achieved by adding ballast weight at the bottom of the cylinder. Spar buoys use catenary mooring lines anchored to the seabed to keep them in place.

The main advantages of spar buoys are that their design is relatively simple, reducing complexity; their stiffness in translational motions; their corrosion resistance since most of the structure is underwater, and that they require simple anchors [16, 22]. The main disadvantages are the buoyancy tank is more expensive as it needs a lot of material; that the installation is on-site, that the floater is sensitive to rotational motions, that longer mooring lines are needed, and that changes to the turbine design are required [16]. The main limitation of spar buoys is water depth dependence; they need water depths higher than 100m [23].

Semi-Submersible:
This type of floater has the characteristic of having a huge semi-submerged platform that provides stability and buoyancy; part of the platform is also above SWL. Many designs could be classified as semi-submersible; some examples are barges, the OC6-DeepCwind with a middle column where the wind turbine tower is installed, and the MaRINET2 with the turbine's tower on one of the buoyancy tanks columns [13, 24]. The MaRINET2 floater is the one simulated in this research paper.

Semi-submersible floater's stability comes from the principle of distributed buoyancy or weighted water plane area. The physical principle consists of covering a wide area of water to avoid overturning [25].

There are many types of semi-submersible floaters. The semi-submersible floater mentioned previously consists of three buoyancy cylinder tanks in an equilateral triangle arrangement, and they have heave plates for additional stability. Figure 2.3 shows the model for clarity. Semi-submersibles are generally kept in place with catenary mooring lines anchored to the seabed.

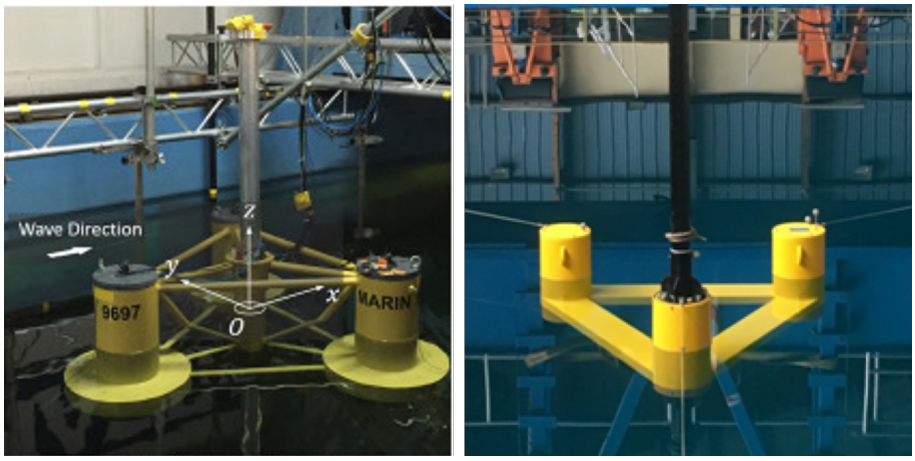

Figure 2.3: Semi-submersible prototypes, OC6-DeepCwind (left) and MaRINET2 (right). Taken and modified from [24, 12].

As Butterfield et al. [16] shows, the main advantages of semi-submersible floaters are: installation since they can be onshore or dry docks and then towed out to the site using conventional tugboats, maintainability and decommissioning are more straightforward since they have extensive experience from offshore oil & gas, and that they do not need complex anchors [17]. Two other significant benefits are that semi-submersible floaters are relatively independent of wind turbine weight and water depth. The disadvantages compared to the other types of floating substructures are that they have higher corrosion, longer mooring lines, more complex designs with more buoyancy tanks, and finally, since a large part of the structure is near the water surface, they are highly wave-sensitive; hence, the wind turbine might need modifications or redesign due to the large motions and forces [16]. The wave sensitivity of semi-submersible platforms is one of the main motivators for this study since there is a need for more complex models to be appropriately analyzed, for example, numerical CFD models.

Barges can be considered semi-submersible floaters since part of the platform is underwater, and part is above water. They are flat-bottomed platforms, and like semi-submersibles, barges provide stability and buoyancy to the wind turbine with the same physical principle, distributed buoyancy [25]. However, they may have less buoyancy or stability than other semi-submersible platforms. Therefore, barges are more cost-effective for shallow water near-shore projects and calm seas.

Tension leg platform:
This type of foundation is a floating platform held in place by vertical mooring lines. The floater is a shallow structure; most is underwater except for the connection between the foundation and the wind turbine tower, as seen in 2.2. The mooring lines' tension achieves the platform's stability [18].

Of the three types of floaters, TLP is the most stable; it has low rotational motions and has the lowest impact on the wind turbine dynamics. Also, because most of the structure is underwater, it has low wave sensitivity and low corrosion. Furthermore, the required mooring lines are shorter because they are vertical [16]. Finally, the structure is cheaper since it requires less material and is relatively smaller [26]. TLPs main drawbacks are that they require complex anchors that harm the seabed, that the onsite installation is hard, and that they are highly dependent on the wind turbine weight [16, 18]. TLPs are more water depth dependent than semi-submersible but less than spar buoys.

In summary, the three types of wind turbine floaters gain stability from the three physical principles; however, they mainly rely on one [16]. The technologies are still relatively new; hence, the market has yet to choose a favorite option as it has for 3-blade wind turbines. The choice between the three types still depends on many factors, such as cost, complexity, water depth, wind conditions, installation difficulty, mooring lines, etc. Likewise, there are three mooring systems catenary, taut leg, and tension leg. The catenary system is commonly used for semi-submersible platforms and spar buoys, the taut leg is not usually used, and the tension leg mooring system is used for TLP. Selecting the best FOWT substructure is a trade-off between the floating platform's dynamics and the extra cost and complexity of the mooring system [18].

2.2. Hydrodynamics of FOWTs

It is important to briefly summarize some pertinent hydrodynamic concepts to make the following report on FOWTs easier to understand. The main concepts of hydrodynamics are explained in this section. The section is divided into four subsections, starting with the six degrees of freedom (6DOF) all floating structures are subjected to, then a section on basics of hydrostatics, followed by a section on waves, and finally, a hydrodynamics section. Understanding these four hydrodynamics concepts makes it easier to understand the complex dynamics of FOWTs and their interaction with the surroundings.

2.2.1. Floating motion

All floating objects have six degrees of freedom [25, 27]. The semi-submersible floater of this report is assumed to be a rigid body, meaning that it has six degrees of freedom and no relative motions. Figure 2.4 shows the convention used in FOWTs, to name the motions. Surge is the translational motion in the x axis; normally, it is in the same direction as the waves and the wind. Heave is the translational motion in the z axis for up and down movements. Finally, pitch is the rotational motion along the y axis. These three degrees of freedom (3DOF) are the ones of interest in this report since they are commonly the most relevant for FOWTs, and due to the symmetric geometry of the floater in the y-direction.

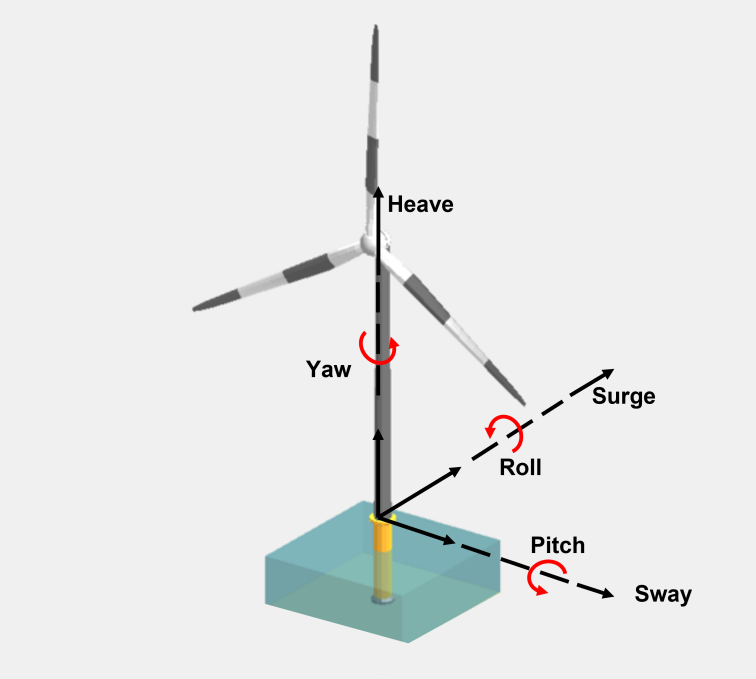

Figure 2.4: Six degrees of freedom of a FOWT.

2.2.2. Hydrostatics

As the name states, hydrostatic is a branch of fluid mechanics where the static behavior of a submerged structure in a fluid is studied, meaning that it is not moving and is in equilibrium. In this particular case, it refers to the semi-submersible substructure floating in the water. If all the forces acting on the floater are in equilibrium, this is called static equilibrium, which means that the addition of all the forces equals zero.

The first force that comes into play is the buoyancy force pushing upward. This force is responsible for the object not to sink and stay afloat. Physically, it comes from integrating the hydrodynamic pressure acting on the structure, the hydrodynamic pressure from the Bernoulli equation [25]. The buoyancy force acts at the center of buoyancy, which is not necessarily the same as the center of mass. The center of buoyancy is the geometrical center of the submerged part of the floater. The hydrostatic force is equal to the buoyance force when static conditions are assumed. The second force is the gravitational force which is pushing downwards. It is caused due to the mass of the floater. The static equilibrium is achieved when all the forces are in equilibrium. The following two equations show the simplified form of the buoyancy force and the linearised Bernoulli equation that represents the static equilibrium:

$$F_b = \rho g V_d \tag{2.1}$$

$$p - p_0 = -\rho \frac{\partial \phi}{\partial t} - \rho g z \tag{2.2}$$

where F_b is the buoyancy force, ρ the fluid density, g the gravitational constant, V_d the volume displaced by the floater, p pressure, p_0 atmospheric pressure. Moreover, the first component of the right side of the equation represents the dynamic pressure, and the second is the hydrostatic pressure [28].

The second important hydrostatic concept is hydrostatic stability. This concept explains the restoring motion to come back to the equilibrium point. The equilibrium point is when the center of mass (**CM**) and the center of buoyancy (**CB**) are aligned. Stability is the ability of the floater to return to its equilibrium point after a disturbance due to a force or a moment [29]. The disturbance causes a heel angle causing the miss alignment between **CM** and **CB** as shown in figure 2.5. From the figure is possible to see the stability lever arm, which is the distance from **CM** to Z, and the metacentre M, which is the point of intersection between both vertical buoyancy forces with the heeling angel and without it [29]. The stability principle is explained in detail for each floater in subsection 2.1.2. Still, in summary, for semi-submersibles, the volume of the columns provides buoyancy, and the water plane area provides stability. For the spar buoy, the ballast makes the structure's center of mass below the center of buoyancy, providing stability. For the TLP, the stability is given by the morning lines [16].

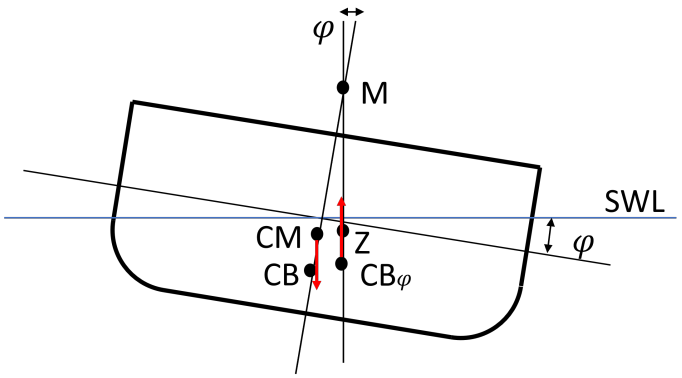

Figure 2.5: Floating objects stability. Modified from [30].

2.2.3. Waves

Even though waves are out of the scope of this report, it is important to mention them since FOWTs are subjected to waves during their entire lifetime, and they are vital for the design process to properly calculate the Fatigue Limit State (FLS) and the Ultimate Limit State (ULS). ULS is a stress limit used to design the floater and the wind turbine to resist extreme conditions and loads. A probabilistic extreme stress extrapolation is performed to obtain the ULS of a structure, which consists of performing load cases of severe cases to get a limit allowing the appropriate design for the site conditions [31]. However, the probabilistic extreme stress extrapolation requires site condition data.

The FLS is more complex because a structure subjected to variable stresses and cycling loading for a long period can also fail even though it never exceeds the yield stress; this is called fatigue. The FLS is the limit for the critical condition where the structure fails due to progressive damage. To determine the FLS, simulations of frequent load cases are required, like the normal operation conditions of the wind turbine. The results of these simulations are rearranged in histograms, and then the number of cycles in a lifetime is compared to the number of cycles until failure. Finally, the damage of the particular load case is calculated, obtaining the total lifetime damage and the FLS [31]. Therefore, for both design parameters, it is important to have a good estimate of the loading acting on the wind turbine and the floater, and the main cause of loads are wind and waves; thus, this review of ocean waves.

There are different types of ocean waves, each classified by its generation process. The three most common are briefly described in this section. The first type and most common are wind waves, which are generated from the direct interaction between the wind and the water surface and occur in the air-water interface. These waves are shaped by the intensity and duration of the wind, giving rise to a range of sizes and energies [32]. Wind waves stand out as the most relevant for the loads' calculation of wind turbine floaters.

Swell waves are the second type of ocean wave. These long-period waves, created by distant storms, travel enormous distances carrying energy while retaining a regular and uniform appearance. Tidal waves are generated by the gravitational force of the moon and the sun. These waves are periodic and more predictable than the other two. They are mainly relevant for structures in coastal and near-shore areas. Throughout the subsequent paragraphs, the focus is centered on wind waves.

Wind waves can be further classified into regular, bichromatic, and irregular waves. Regular waves are sinusoidal and can be represented easily with mathematical equations. Bichromatic waves are the result of merging two waves with different frequencies. It is possible to analyze them by the principle of superposition. Irregular waves are the most common waveform. Irregular waves are generated by the influence of multiple waves, making them random and unpredictable [32].

Regular wind waves can be analyzed with linear wave theory (LWT). The main advantage of it is that it allows superposition. With LWT, complex waves can be represented as the superposition of multiple sinusoidal waves of different frequencies [33]. As the figure 2.6 shows, it is possible to define a wave in LWT in time and spatial domain. The dispersion relation shown in equation 2.3 correlates the frequency with the wave number, allowing to analyze the wave in the time or spatial domain [29]. The following three equations show the dispersion relation, the wave number, and the wave frequency:

$$\omega^2 = kg \tanh(kh) \tag{2.3}$$

$$k = \frac{2\pi}{\lambda} \tag{2.4}$$

$$\omega = \frac{2\pi}{T_p} \tag{2.5}$$

where ω is the wave angular frequency, g the gravitational constant, k the wave number, h the vertical distance from the seabed to the wave's trough, λ the wavelength, and T_p the time period.

Waves analyzed with LWT have several parameters that characterize them; these parameters are seen in Figure 2.6, where H is the wave height, distance from crest to trough, amplitude A is half of the wave height, λ which is the wavelength, T_p the time period, both are the distance from peak to peak; finally, d is the water depth measure from the SWL to the seabed. LWT is a simplified way to describe the motion of a wave; however, it has limitations since waves are complex phenomena that can contain nonlinearities.

A common non-linearity is breaking waves, which depend on the crest instability, the water depth, and the wavelength. In deep water, this nonlinearity is not that present, which is very convenient for floating wind turbines. When the wavelength is seven times smaller than the water depth, it is considered deep water [29].

A second common no-linearity in waves is when there is a high steep wave, this means that to be able to use LWT requires a small wave steepness, meaning that the wave height should be relatively small compared to the wavelength. The ratio between the wave height and wavelength can be used to measure the wave's nonlinearity; the smaller the number, the more the wave presents a more linear behavior [33].

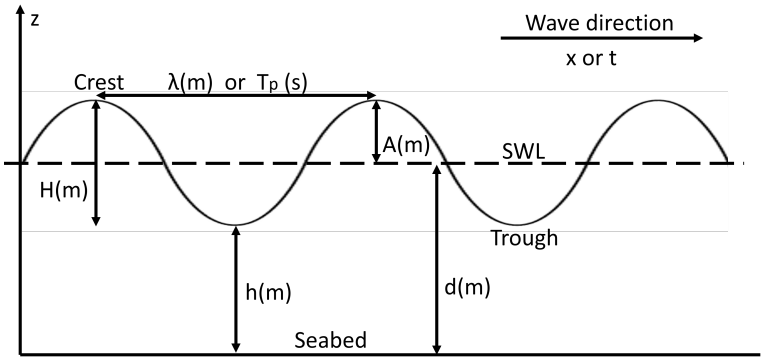

Figure 2.6: Regular wave representation.

2.2.4. Hydrodynamics

Hydrodynamics is the branch of fluid mechanics that studies the motions and loads of the fluid caused by the floater or a force. In hydrodynamics, the floater and the fluid are not in equilibrium, making the analysis much more complex than for hydrostatic and requiring computational models to determine the desired parameters. The studies of fluid motions and loads can have different difficulty levels depending on the assumption and the desired accuracy of the results.

For the analysis of a structure subject to waves, if linearity is assumed, it is possible to decompose the situation into two smaller problems due to superposition. Then the two separate results are added to obtain the final results. The problem is divided into radiation, where the floater oscillates in still water, and diffraction, where the floater is fixed, but there are waves [25]. Computational models are required if linearity can't be assumed due to irregular waves or viscous effects like heave plates.

For this report, the relevant hydrodynamic interactions are between the floater and its surroundings, including water and air. The interaction between the floater and the waves creates loads and forces with three types of main loads present; these are the following:

1. Excitation loads are applied on the floater by incident waves. These are very important loads for the design of the wind turbine and the floating foundation.

2. Radiation loads are caused by the floater's motions. They radiate waves away from the floater. Added mass and damping effects are present in this type of load.
3. Drag loads are caused by viscose effects and non-linearities. They become highly relevant for semi-submersible floaters, especially because the heave plates increase the viscous effects.

In the simulation of this report, the structure is considered a rigid body; therefore, the dynamics of the floater are represented and computed with the equation motions of Newtonian mechanics [34]. The following equation shows the equation of motion for the specific application of a floating object when considered as a rigid body.

$$(\mathbf{M} + \mathbf{A})\ddot{x}(t) + \mathbf{B}\dot{x}(t) + (\mathbf{C} + \mathbf{K})x(t) = F_{ext}(t) \tag{2.6}$$

where **M**, **A**, and **B** are the physical mass, added mass, and damping matrices, respectively. **C** and **K** are resorting matrices; the first represents the hydrostatic stiffness, while the second is due to the mooring lines. Moreover, $\ddot{x}\ (t)$ is acceleration, $\dot{x}\ (t)$ is velocity, $x\ (t)$ is the displacement, and $F_{ext}(t)$ the external forces exerted on the floater; the four components are expressed as a function of the time. The shown motion equation is particular for a floating object since the simplest motion equation does not include the matrices **A** nor **C**.

The added mass is a necessary term to describe a floating object's dynamics accurately. It is caused by the interaction between the floating object and the fluid because the floating object moves in the liquid, causing the fluid to be displaced; as a result, the fluid exerts a force on the object. This extra force makes the floater behave as if it has extra mass. It is a phenomenon that comes from dynamic pressure present in all objects submerged or partially submerged in a fluid [25]. Furthermore, for bodies with a relatively high volume, compared to their mass, like offshore constructions, the added mass effects are particularly important; especially at higher dynamic fluid conditions. Finally, it is given in a matrix since it's a mathematical representation of the impacts caused by each degree of freedom of the floater.

The first force that comes into play is the buoyancy force pushing upward. The damping matrix **B** is a six-by-six matrix representing the damping forces and moments the floating substructure encounters as it flows through the water. The matrix is six by six to represent each DoF. The damping matrix quantifies energy dissipation from the system due to the viscosity and the relative velocity of the object and the fluid. Added mass and damping are highly dependent on the geometry of the floater, waves, fluid properties, water depth, and proximity of the air-water interface [13].

Furthermore, the restoring components are divided into two matrices; the hydrostatic stiffness is related to the variation of displaced volume, hence, to the buoyancy force. The second matrix represents an addition to the restoring forces due to the mooring lines. Depending on the type of floater, this matrix gains a lot of relevance. For example, for a TLP floater, this matrix is essential to accurately predict the floater's dynamics since many motions are involved, such as heave, surge, and pitch. On the other hand, for a SS floater, it is important to have a closer and more realistic dynamic behavior of the structure. Still, the relevance is much smaller since surge is the only motion contributing to the mooring line tension.

Finally, drag coefficients are the last relevant hydrodynamic parameter required for understanding this thesis. The drag coefficient is a dimensionless variable that quantifies the drag force experienced by an object moving through a fluid, and it depends on the fluid properties and the shape of the object. The drag force is caused by frictional effects and pressure variations in the surrounding fluid, and it causes the submerged or floating object to encounter resistance when moving through a fluid. The drag force always opposes the direction of motion or slows the object's movement; therefore, the drag coefficient analyses the motion's resistance of objects through a fluid, and since the floater is in constant movement, the drag coefficients play an essential role in the dynamics [25]. It is possible to assume that the drag coefficient and the damping matrix are the same since they have some similarities, such as their fluid-structure interactions; however, they are different concepts. The damping matrix quantifies the energy dissipation

due to viscous effects in the equation of motion while the drag coefficients are used to calculate the drag forces, which relate to the resistance to movement in the fluids.

2.3. Models and computational fluid dynamics (CFD)

Hydrodynamic solutions and the motion behavior of a structure submerged in a fluid are challenging to calculate due to their complex dynamics; hence, numerical models are commonly used to reach a solution. There are different models, and the appropriate model selection depends on the level of physics, assumptions, problem complexity, and the accuracy desired for the results. Commonly, models are classified by their fidelity to achieve accurate results; however, models with a higher fidelity use more computational resources. This section gives an explanation of how to choose the proper model for tackling the problem, then a brief explanation of PFT, Morison's equation, and CFD. The explanations only apply to time domain tools, frequency domain solvers such as WAMIT, which are faster than time domain solvers [35], can be used, but they are more complex and out of the scope of this research.

The decision to determine which model to use is based on the physics complexity of the problem. The most common parameter to take into account is the viscosity. Since viscosity is not linear, it increases the complexity of the problem. Therefore, if the fluid is inviscid or the viscosity effects are neglected, an exact solution and theoretical approximations are possible. In this case, using PFT models is a good decision because the computational time is faster, and the complexity of the problem is not high. On the other hand, if viscous effects are present and considered, an engineering solution must be used. The most common model is PFT in combination with Morison's equation; this can be a great solution for spar buoy floaters because they are slender, meaning that the diameter of the floater is smaller than the wave's wavelength [36]. However, semi-submersible floaters are not considered slender, and the models of PFT with Morison's equation tend to underpredict. Thus, a high-fidelity approach like CFD is used to achieve accurate results for semi-submersible floaters.

The PFT model is a numerical tool used to describe hydrodynamics and flow behaviors around submerged or semi-submerged bodies. PFT is used under the following assumptions:

1. **Inviscid**, no internal friction within the fluid
2. **Irrotational**, no vorticity or angular moments
3. **Incompressible**, density remain constant within the flow.

In PFT, the velocity field is derived from the gradient of the potential velocity allowing a simplification of the governing equation. Furthermore, velocity potential satisfies Laplace equations, representing the conservation of mass and the irrotational conditions [29]. The following two equations represent the governing equations of PFT:

$$\mathbf{u} = \nabla\phi \tag{2.7}$$

$$\nabla^2\phi = 0 \tag{2.8}$$

where **u** is the velocity field, ∇ is the gradient, ϕ the velocity potential, and ∇^2 is the Laplace operator. PFT is a great option if the assumptions stated above are fulfilled because of its low computational resources. However, it has limitations since it doesn't consider some physical phenomena, such as viscous effects. Therefore, it can not be used by itself when viscosity is present, and therefore an engineering approach is required.

Morison's equation is the most common engineering approach for understanding the fluid behavior and loads on offshore structures. It is a semi-empirical mathematical formulation used to approximate the loads as a function of inertia and drag; hence, it is used to estimate the structures' added mass and damping coefficients. Morison's equation is used to extend the PFT to achieve more accurate results since

it accounts for the extra viscous effect required for a more realistic simulation [11]. The coefficients depend highly on the geometry, so the method works well for some cases, like slender structures. The following equation presents Morison's equation:

$$f(t) = f_i + f_d = (1 + C_a)\rho V\dot{u} + \frac{1}{2}\rho C_d A u\,|u| \tag{2.9}$$

where $f(t)$ is the total force, t is time, f_i is the inertial force, and f_d the drag force. The inertial force is conformed by C_a, ρ, V, and $\dot{u}$, which are added mass, density, volume, and flow acceleration, respectively. The drag coefficients are conformed by the drag coefficient C_d, the reference area A, and the flow velocity u.

Morison's equation is widely used because it can achieve accurate results and uses low computational resources; however, it has limitations. Since it is an empirical engineering solution, it is only accurate for some instances, and the coefficients must be tailored with a higher fidelity simulation. It tends to underpredict loads for cases with complex geometries or non-linearities [11].

Therefore, when the submerged structure has a very complex geometry, the diameter is approximately the size of the wavelength, or there are non-linearities present, PFT with Morison's equation won't give accurate results, and a better approach is needed. Hence, when the problem has a higher level of complexity, a better method like CFD is used due to it being a high-fidelity model which achieves more accurate results at the cost of higher computational resources.

CFD is an iterative numerical model that solves the Navier-Stokes equation and archives accurate results for hydrodynamics and aerodynamics. A more detailed description of the CFD setup used for this thesis is given in chapter 4, and 4.2 is the incompressible Navier-Stokes equation, the governing equation for CFD models used here. CFD solves complex problems with complicated geometries, fluids of different densities and viscosities, and non-linear effects.

Another advantage of CFD is that it can consider turbulence. In many cases, fluids are assumed laminar for simplicity, or if the Reynolds number is low, the fluid is laminar. However, if the Reynolds number is high, adding turbulence through different turbulence models makes it possible to obtain a better physical representation and understanding of the problem. Since turbulence is a complex phenomenon challenging to simulate, it is simulated through turbulence models that have a good representation of the effects on the fluid.

There are different turbulence scales and models to choose from depending on which results are desired. Figure 2.7 shows the criteria for choosing the turbulence model. Reynolds Average Navies-Stokes (RANS) models are used for very complex models and geometries since they use less computational resources, but they only solve the equations for the mean steady solution and use the turbulence model for all turbulent scales; on the contrary, Direct Numerical Solutions (DNS) are used for uncomplicated problems due to the high computational resources required; however, they are used to examine in detail the physics in turbulence, and it can solve all three scales of turbulence [37].

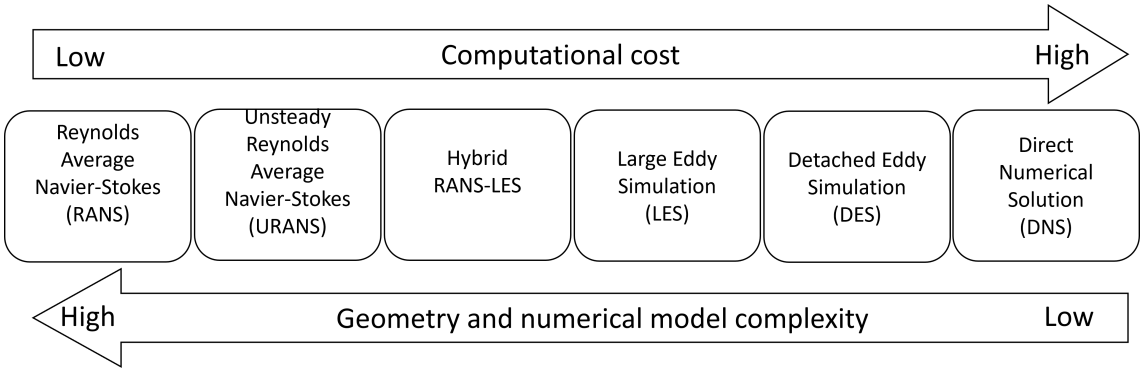

Figure 2.7: Turbulence models criteria diagram.

3

Literature Review

After reviewing the background information required to understand this research project, the literature review chapter aims to provide an analysis of the existing research and literature on CFD simulations and wave basin experiments for FOWT. This literature analysis aims to identify the knowledge gap this research could fill and to provide a theoretical and conceptual framework for the study.

To achieve the environmental targets set in the Paris Agreement and meet the SDGs, there is a need to accelerate the deployment of FOWTs. To facilitate this, it is important to enhance the efficiency and speed of the design phase. A few experiments and simulation models have been developed to improve and optimize the design phase of wind turbine floaters. However, given that FOWT is a relatively new technology, a substantial portion of the existing literature on floater structures draws from the oil and gas industry, as highlighted by Gueydon et al. [24] and Azcona et al. [38]. This presents a significant limitation in verifying and validating computer numerical models, as there is a lack of data due to the limited number of experimental wave-tank tests conducted so far.

In an attempt to address the issue, specific consortiums and initiatives have emerged to tackle the lack of empirical testing. The following are some of the initial wind turbine experiments conducted as model-scale prototypes. Koo et al. [39] experiments involved model setups corresponding to a 1/50 Froude scaling for three distinct floaters: a spar buoy, a semi-submersible, and a TLP floater, Stewart and Muskulus [9] conducted a wave-tank experiment involving the MARINTEK braceless semi-submersible, and Azcona et al. [38] performed a wave-tank experiment with a 1/40 scale model of the Concrete Star Wind Floater, which is a semi-submersible platform designed for a 6 MW wind turbine.

As emphasized by Koo et al. [39], the primary objective of these wave-tank experiments is to generate data on the motions and loads experienced by coupled floater and turbine systems. This empirical data is required for the validation and fine-tuning of numerical models. A significant initiative in this field is the Offshore Code Comparison Collaboration Continuation (OC4), introduced by Robertson et al. [40]. This international collaborative effort is dedicated to enhancing the reliability of numerical models utilized in offshore wind applications. The OC4 initiative introduced the DeepCwind semisubmersible floater design, which has been further employed in the OC5 and OC6 projects, with some adjustments in terms of mass and inertia, while retaining the same fundamental geometry, as mentioned by Wang et al. [13]. This initiative is highly relevant due to the amount of available data it provides. Consequently, due to the available data for comparison and validation, most numerical simulations involving semisubmersible floaters have adopted this particular floater as a reference point for their analysis.

As suggested by Stewart and Muskulus [10], full-scale prototypes would be the ideal method for validating models. However, their construction and operation are too expensive, and the existing experiments are often private and lack accessible data. For this reason, wave-tank scale experiments, as proposed by Stewart and Muskulus [10], are a viable alternative. Yet, they still have certain limitations, such as issues with scaling. Scaling prototypes presents a challenge that needs precision in multiple aspects, including mass, inertia, and the calculation of relevant forces. Typically, scaling employs the Froude number, which

accurately preserves hydrodynamic properties, but it is not optimal for aerodynamic properties since it produces a low Reynolds number as mentioned by Azcona et al. [38], and drag and lift are highly sensitive to the Reynolds number.

Furthermore, Gueydon et al. [24] supports that wave-tank testing offers several advantages over full-scale tests besides enabling numerical model validation. Wave-tank experiments are more efficient, cost-effective, and permit experimentation across a range of parameters. Additionally, they allow for independent testing of individual subsystems. However, wave-tank tests also come with drawbacks when compared to numerical methods, like the experimental uncertainties they present. To mitigate experimental uncertainties, standardization is proposed by [24] by conducting the same set of experiments in four different wave-basin facilities using identical scale models.

Numerical methods provide an alternative, complementing physical experiments with scale prototypes for obtaining hydrodynamic loads and essential floater parameters. Some of the earliest simulation models for semisubmersible floaters are the following. Bayati et al. [11] simulated the DeepCwind semisubmersible floater with a combined approach of using WAMIT and FAST and Rivera-Arreba [29] analyzed the response of the DeepCwind semisubmersible floater to nonlinear wave loading by two different numerical modeling tools and then compared both tools.

Different types of numerical models are employed to study hydrodynamic properties and load responses. As pointed out by Bayati et al. [11], currently, the most used modeling tools for these purposes are mid-fidelity models based on Potential Flow Theory (PFT) in conjunction with Morison's equation. PFT's assumption of inviscid flow limits the hydrodynamic damping, and Morrison's equation accounts for the viscous effect required for a more realistic simulation. Wang et al. [13] point out the significant advantage of mid-fidelity models, their relatively low computational resource requirements, and the potential for accuracy results when properly tuned. Rivera-Arreba [29] reinforces this point, highlighting that PFT-based models offer faster computations and reduced computational resource demands, making them highly suitable for preliminary design due to their cost-effectiveness.

Rivera-Arreba et al. [41] adds further insight, affirming that PFT models are computationally efficient and are well-suited for analyzing global dynamics. However, they exhibit limitations when nonlinearities, like when extreme conditions come into play. It is worth noting that all numerical models necessitate tuning and validation, as stated by Koo et al. [39]. However, the performance of mid-fidelity models can be significantly increased through careful adjustment of drag coefficients due to the dominance of viscous damping in the motion dynamics, as emphasized by Wang et al. [13].

As mentioned previously, mid-fidelity models are good simulation tools for assessing global dynamics. However, they tend to under predict hydrodynamic parameters when the effects of nonlinearity are present and perform inadequately in low-frequency responses, as highlighted by Wang et al. [12]. In their effort to enhance OpenFAST, the report discusses the adjustment of viscous drag forces near the waterline to address these limitations. Reddy et al. [42] also corroborates this observation, pointing out that mid-fidelity tools often under predict hydrodynamic loading. The dominating viscous effects in the simulations are one of the main reasons for the under prediction of the PFT models because Morison's equation uses a constant drag coefficient, which ignores the frequency and amplitude dependency of the hydrodynamic coefficients.

To properly fine-tune mid-fidelity models, Wang et al. [13] and Wang et al. [12] emphasize the necessity of obtaining the required parameters either from CFD simulations or experimental data. This reinforces the critical role of validated CFD models in improving mid-fidelity simulations' accuracy. Moreover, as suggested by Stewart and Muskulus [10], CFD models offer a cost-effective and less complex alternative than physical experiments, promoting their adoption. However, this does not imply that wave-basin laboratory experiments should be discontinued or that they are not required anymore. Instead, it emphasizes the importance of validating numerical CFD models against experimental data to ensure their reliability.

In light of the previous considerations and the need to enhance the design phase of FOWTs, several numerical and CFD simulations have been conducted to advance this technology. Some of these simulations are the following:

Pinguet et al. [43] conducted a free decay test on the DeepCwind semisubmersible floater employing the overset mesh method. Later Pinguet [44] combined the overset mesh method with the waves2Foam solver to compute forces and hydrodynamic responses of the DeepCwind semisubmersible under realistic wave conditions. Liu [45] developed a fully coupled high-fidelity CFD tool using OpenFOAM, enabling a detailed analysis of the aerodynamics, hydrodynamics, and moorings of the DeepCwind floater.

Furthermore, Wang et al. [13], as part of the OC6 project, utilized the DeepCwind semisubmersible to evaluate various CFD setups. These setups were validated through a free decay test employing PQ analysis against experimental data, demonstrating that CFD could effectively provide hydrodynamic coefficients to fine-tune mid-fidelity models. Also Reddy et al. [42] conducted a numerical CFD simulation using a forced oscillation test, aiming to determine the added mass and damping coefficients near the natural periods of the 1/50 scaled model of the DeepCwind semisubmersible floater. Reddy et al. [42] also highlighted how the PFT underestimated the hydrodynamic coefficients for heave, surge, and pitch.

All these experiments analyze various aspects and pursue different objectives. However, they share a common denominator: the use of the DeepCwind semisubmersible floater. Supporting the previous statement, most numerical simulations involving semisubmersible floaters employ this specific floater as a reference point for their analyses.

However, as emphasized by Wang et al. [13], hydrodynamic parameters such as added mass and drag coefficients strongly depend on floater geometry. For example, the damping in surge motion is sensitive to both the geometry and the amplitude of motions. Heave plates, a component of the floaters, significantly influence added mass coefficients in motion responses. The role of geometry in dictating hydrodynamic behavior is further supported by Philip, Seeninaidu, and Bhattacharya [46], who states that damping elements like heave plates are important components in offshore structures, serving to mitigate hydrodynamic responses and maintain them within acceptable limits.

Reddy et al. [42] further supports the importance of geometry and heave plates by noting that heave plates induce vortex shading, resulting in a domination of heave motion by viscous damping. Moreover, in alignment with the significance of geometry, Zhang and Ishihara [47] conducted a study specifically focused on the effects of geometric parameters on hydrodynamics parameters caused by the heave plates. This research concluded that various parameters of the heave plates, such as spacing ratio and diameter, have a significant influence on added mass and drag coefficients.

It is important to recognize that geometry highly influences hydrodynamics since the semi-submersible floater utilized in the current report is the EU H2020 MaRINET2. Previous researchers have undertaken similar simulations, such as Wang et al. [13], which evaluated several CFD setups validated with a free decay test. Reddy et al. [42] conducted forced oscillator simulations to obtain added mass and damping coefficients. Likewise, Li and Bachynski-Polić [48] employed CFD simulations with forced oscillatory motion to derive added mass and drag coefficients near the natural periods of surge, heave, and pitch motion. Importantly, all three of these studies focused on the DeepCwind semi-submersible floater.

However, the main objective of this report is to analyze the added mass and drag coefficients of the MaRINET2 semi-submersible floater when subjected to a forced oscillatory motion with a validated CFD model. This will lets us address the knowledge gap this research is fulfilling within the field of FOWTs. Since it is the first time a numerical CFD model for the EU H2020 MaRINET2 project floater has been constructed. It marks the initial research to extract added mass and drag coefficients through simulations across varying frequencies and amplitudes for this specific floater.

The numerical model established here is validated against results from the wave-basin experiments presented by Gueydon et al. [24]. Subsequently, the validated model is used to obtain added mass and drag coefficients for the MaRINET2 floater. These coefficients obtained may offer insights for comparative analyses with existing research, enabling an assessment of both similarities and differences. Additionally, these hydrodynamic coefficients facilitate the tuning of mid-fidelity numerical models based on PFT and Morison's equation. Such models, although computationally efficient, need fine-tuning to yield accurate results.

4

Numerical Method & Mesh

After reviewing the background theory and the previous studies on similar topics, it is possible to continue with a detailed explanation of the numerical method used for the simulations performed for this report. Hence, the objective of this chapter is to describe the methodology, the numerical model setup, and the mesh used in this research study. For that, the chapter is divided into four sections; first, section 4.1 presents the governing equations of the numerical model. Section 4.2 describes the numerical setup, including numerical domain, boundary conditions, mooring lines, numerical schemes, and turbulence model. Then the simulations' mesh is described in detail in section 4.3. Finally, the mesh convergence study results are shown and analyzed in section 4.4.

4.1. Governing equations

Navier-stokes equations and the continuity equation properly describe the interaction between the floater and the fluids. This iterative process needs CFD numerical models to achieve a solution since there is no analytical solution for this [29]. The solver used is inteFoam, a solver inside the OpenFOAM CFD software. InterFoam uses the finite volume method and a volume of fluid (VOF) model for two incompressible Newtonian fluids; therefore, the governing equations for the simulation are the fundamental equation for incompressible flow, which are presented as follows, the continuity equation 4.1 and the incompressible Navier-Stokes equation 4.2:

$$\nabla \cdot \mathbf{u} = 0 \tag{4.1}$$

$$\rho \left(\frac{\partial \mathbf{u}}{\partial t} + (\mathbf{u} \cdot \nabla)\mathbf{u} \right) = \rho \mathbf{g} - \nabla p + \mu \cdot \nabla^2 \mathbf{u} \tag{4.2}$$

where ∇ is the gradient operator in the three dimensions x, y and z, $\mathbf{u}$ is the velocity vector, ρ is the fluid density, t is the time, $\mathbf{g}$ is the gravitational constant, p the pressure and μ the fluid viscosity. For a better understanding of equation 4.2, it can be divided into three groups. The first two groups are on the left of the equal sign, and the third group is on the right side of the sign. The first group is the mass indicated or represented by the density of the fluid, then the second group is the acceleration, which contains two components: the change in velocity over time and the fluid's speed and direction. These groups are equal to the third group, which is the forces. The forces group is composed of the gravity, the pressure gradient, and the viscous forces, respectively, and the term $\nabla^2 \mathbf{u}$ is the Laplacian. Furthermore, interFoam uses the VOF method, which is used to differentiate the density ρ and the viscosity μ between the two fluids in the simulation as an interface tracking algorithm since, in reality, the two fluids are different and must be differentiated. These two parameters are given with the following two equations:

$$\rho = \alpha \rho_w + \rho_a (1 - \alpha) \tag{4.3}$$

$$\mu = \alpha\mu_w + \mu_a(1-\alpha) \tag{4.4}$$

where α is a scalar between 0 and 1, a denotes air, and w refers to water. Hence, from the equations, if α = 0, the fluid is air, and α = 1 is water. However, there are cells in the air-water interface where 0 < α < 1, here the volume fraction is obtained with the following equation:

$$\frac{\partial\alpha}{\partial t} + \nabla\cdot(\mathbf{u}\alpha) + \nabla\cdot(\mathbf{u_r}\alpha(1-\alpha)) = 0 \tag{4.5}$$

where $\mathbf{u}_r$ is the compression velocity, an artificial velocity field that points toward the free surface [49]. Equation 4.5 plays an important part in the VOF method since it is the equation that allows the air-water interface to be properly defined for the numerical solution [42].

4.2. Numerical Set-up

As seen from the previous chapter 3, experimental data or a high-fidelity tool is necessary to obtain the hydrodynamic added mass and drag coefficients. However, this research study only focuses on the numerical tool. It uses a CFD model as the high-fidelity numerical solution and compares the model results against experimental data from previous research, reported in Gueydon et al. [24] paper. As mentioned in section 4.1, the numerical solution is based on the combination of the Navier-Stokes equation and the mass conservation equation. The Navier-Stokes equation is a mathematical equation representing the conservation of momentum, and it is used to describe the motion of fluids.

OpenFOAM is the CFD software of choice since it is open-source software; it contains a wide range of solvers and has been used before in several similar simulations. Furthermore, OpenFOAM includes meshing tools for complex geometries and an efficient discretization method allowing the conservation properties and the solution's stability. In addition, the selected solver within OpenFOAM is interFoam. It is used because it fulfills all the requirements for the simulation. It is a solver for two incompressible, isothermal, and immiscible fluids, water and air [50]. The simulation is incompressible because air is considered incompressible at low speeds; it is isothermal due to temperature remaining the same, and finally, immiscible because the water and the air won't mix together.InterFoam uses the volume of fluid (VOF) method as an interface tracking algorithm to distinguish between the two fluids and allows optional mesh motion [51]. The following subsections explain the numerical domain, the boundary conditions, the mooring lines, the numerical schemes, and finally, the turbulence model used.

4.2.1. Numerical domain

In general, all CFD solvers are very Mesh dependent; this is also the case for inteFoam. For that reason, the mesh is discussed in section 4.3 in a detailed way. However, some details of the numeral domain are given here.

As previously stated in the literature review, chapter 3, validating the numerical models against experimental wave basin data is vital to determine if the model works properly. Therefore, the model is intended to be validated against the data obtained by the University College Cork (UCC) and the University of Strathclyde (UoS), reported in the report by Gueydon et al. *Round Robin Laboratory Testing of a Scaled 10 MW Floating Horizontal Axis Wind Turbine* [24]. Ideally, to make the best comparison, the rectangular numerical domain should be the same size as one of the two wave tank dimensions; however, the wave tank dimensions are too big, and if the entire domain were used, the CFD simulation would use an incredibly high amount of computational resources; thus, a smaller domain was used. Table 4.1 presents the dimensions of the UoS and UCC wave tank and the dimensions of the domain used in the numerical CFD simulations. Finally, the wave tank z-direction value represents the depth of the basins. Yet, for the CFD simulation, it is the entire z-direction domain, including the region under and above water.

Table 4.1: UCC, UoS wave tanks and CFD simulation dimensions. Wave thanks dimensions taken from [24].

Parameters	UCC wave tank	UoS wave tank	CFD simulation
x-direction or Length (m)	35	76	8
y-direction or Width (m)	12	4.6	6.4
z-direction or Depth (m)	3	2	3.2

It was decided to use this domain size because it is considerably smaller than the UCC and the UoS wave tank, greatly reducing the simulation's computational resources required. Nevertheless, the mesh domain must be manageable because it is important to have a large enough mesh to fit the mooring lines. The mooring system selected is the small mooring system of the Gueydon et al. [24] paper with a horizontal span of 4.5m. Moreover, the accuracy of the results is affected by the domain size. A big enough mesh is desired to avoid the boundary affecting the results; however, it can not be too big because a bigger mesh implies higher computational resources. For those two reasons, this domain size was chosen. It is bigger than the mooring system span and has sufficient space, so the boundaries do not affect the results' accuracy. Figure 4.1 Shows the numerical domain, and figure 4.2 shows the sizes from the different wave basins reported in Gueydon et al. [24] paper. The figures show the two wave basins of interest and their important differences in size.

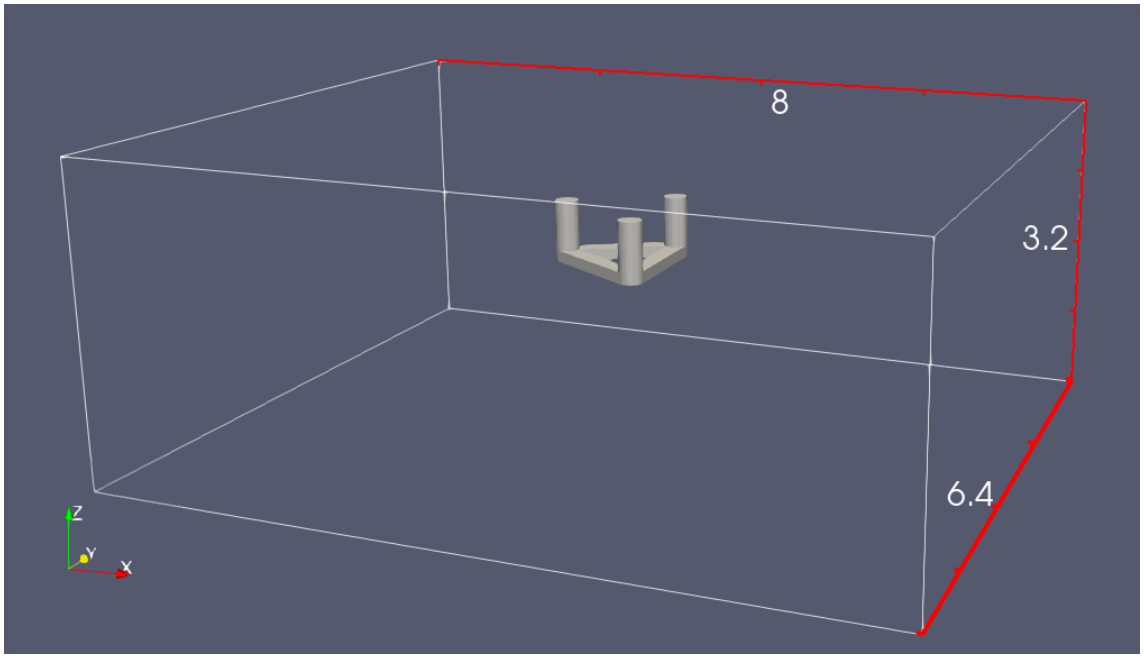

Figure 4.1: Numerical domain representation.

4.2.2. Boundary conditions

Even though initial conditions are an essential part of the set-up of a numerical model simulation, they can vary considerably from simulation to simulation; therefore, they are described and explained in chapter 5 where the two different types of simulations are presented. On the contrary, the boundary conditions are similar for both types of simulations and their many load cases. This subsection displays the boundary conditions used in the numerical model.

The boundary conditions are the rules for understanding how the numerical domain behaves due to interacting with its surroundings. Since it is a rectangular domain, it must have at least a minimum of six boundary conditions, one per each side: front (inlet), back (outlet), up (atmosphere), bottom, right, and left.

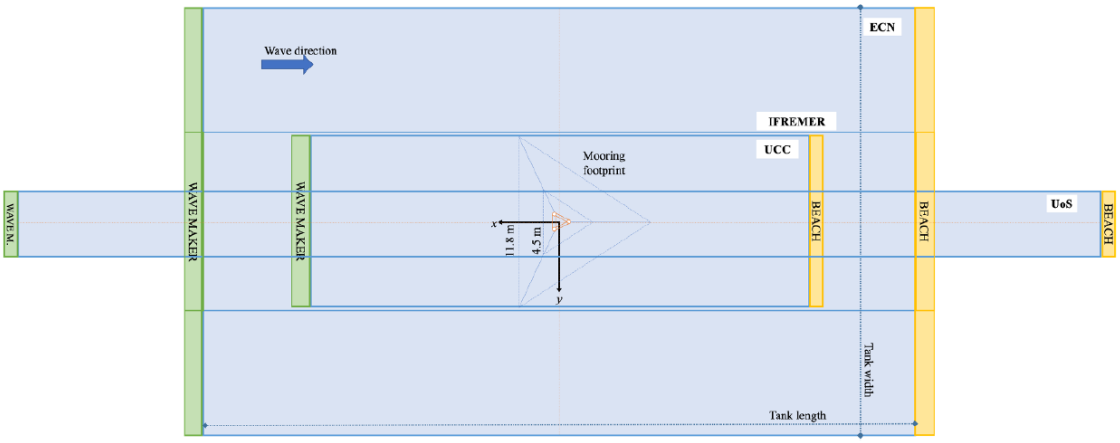

Figure 4.2: Wave basins sizes. Taken from [24].

However, there are seven boundary conditions for this particular numerical model since the SS floater geometry is also considered one. The boundary conditions of the numerical model are presented in table 4.2, where it is possible to see the type of boundary condition, their coordinate location in the mesh, and the rules for the three most important parameters.

Table 4.2: Numerical CDF model boundary conditions. Dimensions presented in model scale.

Boundary	Location (m)	Boundary Type	Velocity	Pressure	Volume Fraction
Semisubmersible					
floater	(0,0,0)	Wall	No slip	Fixed flu	Zero Gradient
Inlet	x=4	Wall	Slip	Zero Gradient	Zero Gradient
Outlet	x=-4	Wall	Slip	Zero Gradient	Zero Gradient
Atmosphere	z=1.6	Pressure Outlet	Pressure inlet outlet	Atmospheric	Zero
Bottom	z=-1.6	Wall	Slip	Zero Gradient	Zero
Rigth wall	y=3.2	Wall	Slip	Zero Gradient	Zero Gradient
Left wall	y=-3.2	Wall	Slip	Zero Gradient	Zero Gradient

The first boundary is the SS floater geometry, placed in the middle of the domain where the z-direction center point is in the SWL. This boundary field is highly relevant because it is the point of interest in these simulations since the desired outcomes are the loads the floater experiences.

Furthermore, the boundary field bottom, right wall, and left wall can be grouped in one class called walls since all the parameters except the coordinates are the same. This boundary class is called walls because it is what it represents: a wall with no slip. Moreover, the inlet and outlet fields are also considered walls for this particular numerical model because there are no waves or wind input in the simulations; however, the inlet normally describes how the fluid water or air enters a computational domain and the outlet how it exits. The outlet is also usually the point of interest. Finally, the last interaction with the surroundings is the field *Atmosphere*, the top part of the domain. This boundary is a pressure outlet type, meaning an actual force is exerted on the top. The force exerted on the top is the atmospheric pressure; furthermore, at the upper edge of the domain, there is only air; hence, the volume fraction of zero represents that the fluid at that point is air, and there is no water-air interface there.

All the boundary fields, except the *Atmosphere* and *Bottom*, have a volume fraction of *zero gradient*, meaning that there is an air-water interface at some point of the boundary field because a change from zero to one occurs. The air and the water extended in all the x and y ranges of the domain; hence, the

fluid interface is set in the z-direction. The setFields utility defines the initial volume fraction (α); thus, the SWL in the simulations. As mentioned in the subsection 4.1, if $\alpha = 0$, the fluid is air, and if $\alpha = 1$ is water; hence, the way setField works is by setting α value to one in a selected box from the bottom boundary to the SWL which is in the 0 coordinate of the z-axis.

4.2.3. Mooring lines

As mentioned in chapter 2, the FOWTs' substructure comprises the floater and the mooring systems. There are three ways to model the behavior of mooring lines: first, with a static model that only uses constant loads. second, they can be simulated with a quasi-static model considering the mooring lines as a linear spring. Finally, a dynamic model where the lines are discretized and modeled as a chain [29].

Remember that the mooring lines are used in the free decay test for model validation; thus, a certain level of accuracy is required to validate the model. Therefore, the mooring lines can not be ignored under any assumption. Likewise, the static model is discarded due to its low accuracy and representation of reality. Yet, a dynamic model is also not recommended, even though it might be the most accurate because it is too complicated and computationally expensive. Hence, it was decided to model the mooring lines as a linear spring with a quasi-static model, which has been used previously in different papers and has proven to work appropriately [13, 29, 42].

Even though the most common morning system for SS floaters is catenary, the way it is modeled and simulated in this study is by using an aerial mooring system as similar as possible to one presented in the paper of Gueydon et al. [24]. The paper's experiments used two different compositions of mooring lines; the UCC used an aerial mooring system with a spread of 11.8m, and the UoS wave basis implemented a smaller design with a 4.5m spread. This study decided to use the small aerial mooring system because there is data to compare and because it represents a smaller numerical domain, meaning fewer computational resources. Furthermore, the morning lines spread is one of the reasons for using the size of the numerical mesh presented in table 4.1 since the anchors of the mooring lines need to be inside the domain, too.

The linear spring quasi-static model is implemented in OpenFOAM in this research by using the *sixDoFRigidBodyMotion* solver within the dynamicMesh dictionary. This approach simulates the mooring lines as an external force that restrains the solver. The solver needs general floater parameters like mass, moments of inertia, and center of mass that are strictly required for the simulation. However, it is also possible to add extra components to build in the simulation as desired; for this, there are two options to add constraints or restraints.

The constraint inputs are used when it is desired in the simulation to stop one or more degrees of freedom completely and only simulate the desired DoF. For example, if the interest is to analyze the heave motion without any other movement, surge and pitch should be eliminated or stopped, which is done in the constraints section. However, this is not desired here, so this section is kept the same. On the contrary, the restrain section is modified since the mooring line parameters are input here to be considered an external force. This section requires the number of mooring lines with their stiffness, damping, rest length, anchor coordinates, and floater attachment coordinates. Furthermore, the restain section also specifies that the mooring lines will be simulated as linear springs as the following equation:

$$F = kx \tag{4.6}$$

where F is the forces exerted by the mooring lines, k is the stiffness with a value of 21.1N/m, and x is the distance difference from the rest length to the actual position. The resting length is 1.86m, and the damping is 0, as mentioned in the Gueydon et al. [24] paper, it is simulated as a pure linear spring.

4.2.4. Numerical Schemes

Numerical schemes are sets of algorithms used in CFD when dealing with complex mathematical problems governed by differential equations such as the ones presented in subsection 4.1, equations 4.1, 4.2, and 4.5. Given the absence of exact analytical solutions for these equations, an iterative process with numerical schemes is required. They are used in the iterative process necessary for approximating solutions by discretizing the problem domain. Within CFD, there are four types of grid discretization, but OpenFOAM solvers use finite volume methods, a discretization approach that involves balancing fluxes between control volumes to ensure mass conservation and simplifies the handling of boundary conditions [29]. The choice of a numerical scheme involves a trade-off between accuracy and computational cost. More accurate schemes often require finer grids and more computational resources.

But how are these numerical schemes implemented within the OpenFOAM framework? The process involves specifying the schemes to be used in the *fvSchemes* and *fvSolutions* files [52]. In this context, the specific numerical schemes employed for the simulations in this report are detailed in table 4.3. The selection of these schemes was guided by the methodology outlined in the work of Reddy et al. [42], where similar simulations were conducted. This ensures that the numerical schemes employed here align with established practices within the field.

Table 4.3: Numerical schemes used in the simulations.

Scheme type	Solver or scheme selected
Time derivative scheme	Euler
Spatial domain	Finite Volume Method
Gradient scheme	cellLimited Gauss linear
Divergence scheme	Gauss linear
Laplacian scheme	Gauss linear limited 0.33
Interpolation Schemes	Linear
Surface normal gradient scheme	Limited 0.33
Pressure velocity coupling	PIMPLE: nCorrectors 3, nNonOrtogonalCorrectors 3, nOutCorrectors 1
Interface capturing scheme	MULES
sixDoFRigidBodyMotion solver	Newmark solver
Acceleration relaxation factor	1.0

4.2.5. Turbulence Model

The turbulence model used throughout the simulations is the final missing part to describe the setup. For some applications like aerodynamics, the turbulence model selection is highly relevant since it can have a high impact on the results. In FOWTs, turbulence and turbulence models become of high relevance in high wind conditions since they affect the floater loading, and the mooring lines tension is dependent on the model used [53, 54]. In this case, the simulations are only of the floater, and due to the low Reynolds, the turbulence model has a low effect on the results, as presented in the following two papers where it is mentioned that the response is very similar for laminar and different turbulence models [13, 55]. However, the main use of the turbulence model in this case is to model any vortices in the water. Furthermore, the papers also note some motions are more sensitive to different models than others.

The selected turbulence model is the $k-\omega\ SST$, which is part of the RANS turbulent models group. Figure 2.7 is used as criteria for choosing this particular model. The geometry and numerical model used in the simulations are already complex; furthermore, the turbulence model has a low impact on the results; hence, LES, DES, and DNS models, which are very computationally demanding, are discarded. On the other hand, RANS models like $k-\omega$ or $\epsilon-\omega$ are also discarded because they only solve for the mean steady solution [37]. So, the options are reduced to RANS with the SST or a Hybrid RANS-LES model. Moreover, another reason for choosing the $k-\omega\ SST$ is because it has been used for very similar applications in

Wang et al. [13] and Tran and Kim [27, 55] papers, and the results show to agree with the experimental tests.

The $k-\omega\ SST$ is a two-equation eddy-viscosity turbulence model used in CFD; it was introduced by Menter in 1994. The model is based on the $k-\omega$ model, and it is composed of two transport differential equations that combine to a certain point the best part of the $k-\omega$ and the $k-\epsilon$ turbulence models, leading to better results as mentioned in Menter [56] paper. The model is a good option since it can handle many turbulence flows and complex ones that interact with solid boundaries, like the SS floater. It allows a wide range of turbulence flows since it behaves as the $k-\omega$ in the inner layer of the boundary layer and as $k-\epsilon$ in the outer region near the walls where the $k-\epsilon$ model is known to perform well [56].

OpenFOAM allows three types of simulations: laminar, Reynolds-average stress (RAS), and LES. Laminar simulations don't use any turbulence model, and LES was previously discarded. The $k-\omega\ SST$ is implemented by selecting RAS modeling inside the turbulence properties dictionary and then selecting the $k-\omega\ SST$ model [57]. After that, the initial conditions of k and ω are needed for each patch. K and ω are the turbulence kinetic energy and the specific dissipation rate, respectively. As a remark, each path is a boundary condition; hence, the model has seven patches. The wall functions available in OpenFOAM are used for the SS floater patch, so it can be considered a wall boundary type as seen in table 4.2.

4.3. Mesh

The previous section gave a detailed description of the numerical model used for the simulations. It showed the steps taken to perform the simulations and mentioned that the solver interFoam performance and stability depend on the mesh quality and refinement. Thus, this section jumps into a detailed description of the mesh used for the simulations. The section is divided into two subsections. First, the method used to generate the mesh is explained and discussed in subsection 4.3.1. Then the simulation's mesh is presented in detail, including the refinement areas, in subsection 4.3.2.

4.3.1. Mesh generation method

The main two reasons for choosing OpenFOAM are that it is an open-source CFD software and because it includes several simulations and meshing solvers. The meshing solver selected for the simulations is *dynamicFvMesh* solver, which works with the dynamic mesh method principles. The mesh generation method used for the simulations is the dynamic mesh method. As explained in the previous chapter, during the two types of simulation performed in this research study, a rigid body is offset and released into a decay test, or the same rigid body is forced to oscillate in one degree of freedom at the time. Therefore, to maintain the high quality of the mesh, it is necessary that the mesh changes during the simulation. Then the reasons behind choosing *dynamicFvMesh* solver are that it is compatible with physical models like interFoam, it allows the motion of a rigid body during the simulation, the solver allows the mesh to change during the simulation, and the results are more accurate than with static meshes. However, dynamic meshing also has a few disadvantages and limitations; it has more requirements than static meshes, during the simulation, it is harder to achieve stability, it is very time-consuming, and it uses a lot of computational resources. Finally, coming back to the working principle of the dynamic mesh solver, the way the mesh changes during the simulation is based on deformation, meaning that the number of cells remains the same during the entire time, but the cells become smaller or bigger. The main advantage of establishing the mesh change in deformation is that the initial orthogonality of the mesh is conserved, as mentioned in Rivera-Arreba [29] thesis.

Although the concept of the mesh changing during the simulation without altering the number of cells remains the same for both types of simulations, the way it is done in the *dynamicFvMesh* solver is different. For the free decay test, the main solver uses a sub-solver called *sixDoFRigidBodyMotion* that contains many parameters, like the center of mass, the innerDistance, the outerDistance, moments of inertia, constraints, and restraints, which are the model mooring lines. The two important parameters for the mesh morphing are innerDistance and outerDistance. These two parameters describe the morphing of the mesh during the simulation. The cells between the floater edges and the innerDistance move with the floater as one body, meaning they remain constant during all the simulations. On the other hand, the cells

between the innerDistance and the outerDistance are the cells that change in size during the simulation. It is important to size both parameters correctly, the first to avoid simulation stability problems and the second to reduce computational resources used. Since morphing uses high resources, having all the mesh domain morphing is not desirable, and having changes only in the regions close to the simulation's points of interest is optimal. The values used for the simulations are 0.025 and 0.5 for inner and outerDistance, respectively.

The forced oscillator simulation uses the *displacementLaplacian* solver inside the dynamicMesh dictionary; this solver requires a diffusivity function to define motion to the floater, and the one used is the inverse distance from the floater. It was selected because it has been used in previous papers [42]. Finally, the initial parameter that makes the floater oscillate during the forced oscillatory simulations is set in the point displacement initial condition.

Now that the description of the solver used in the dynamic mesh dictionary is done, let's go in-depth into how the dynamic mesh method in OpenFOAM works. It consists of two main steps:

1. **Background mesh generation:** The initial background mesh is generated with the *blockMesh* utility. In this utility the following essential parameters are defined:
    - Domain size in 3D.
    - Patches with their location and boundaries type.
    - Cell expansion ratios.
    - Base cell size, which is the size before refinement.
2. **Refinement around the floater:** For this part the *snappyHexMesh* utility is used. It is a time-consuming and computationally intense step since it is an iterative process. In a broad overview, in this step, the floater is introduced into the simulation, and the background mesh is refined. This is done by following the four sub-steps:
    - Geometry.
    - Castellation.
    - Snapping.
    - Adding layers.

First, in the geometry section, the SS floater's geometry is introduced into the mesh; the file required is a stereolithography (STL) format. Furthermore, in this section, the refinement regions are defined. The refinement zones used for the final mesh are described in 4.3.2. The second step is castellation; here, some parameters are defined as the region's location to mesh (inside or outside the STL file), the refinement zones, and the level of refinement desired. In this step, the background mesh gets refined, the cells near the floater split, and the cells inside the floater's geometry get removed. On the third step of snapping, the castellated boundaries are moved to the floater surface, making the mesh more homogenous and with a better transition. Finally, the fourth step is adding layers to the mesh near the floater edges; this makes the mesh transition smoother and avoids convergence problems during the simulations [58].

4.3.2. Simulation's mesh and refinement zones

The preceding subsection explained the generated mesh method. This subsection details the specific aspects of the mesh utilized in the simulations, covering various elements, including the floater's geometry, the refinement regions, and the mooring lines' dimensions.

Floater's geometry

As mentioned before, the floater used for the simulations is the 1/60th scaled model of the MaRINET2 semi-submersible floater, the same used by Gueydon et al. [24]. The picture of this floater is shown on the right of figure 2.3. Furthermore, it is essential for the accuracy of the simulation to have the proper

parameters and dimensions of the SS floater; hence, this subsection shows in detail all the parameters of importance for the simulations. Most of the parameters were obtained directly from the reference paper, and the rest were calculated.

The dimensions of the geometry are the same as the ones shown in figure 4.3. From the figure, it is possible to see that the SS floater has three buoyancy cylinder tanks, called from now on columns for simplicity. The columns are in an equilateral triangle arrangement. The connections between the three columns are under the SWL all the time, and for the same reason, they are considered the heave plates of this floater. None of the simulations consider the wind turbine on the floater; however, it is assumed that the upstream column would be the one where the wind turbine tower should be installed. Furthermore, the figure also shows the desired simulation origin for x and y directions, which are located in the geometric center of the floater. For the z direction, the figure shows the origin at the bottom of the floater, but the origin used in the simulations and calculations is the SWL. So the (0,0,0) coordinates of the simulations for the x a y direction are in the geometric center of the floater and for z is in the SWL.

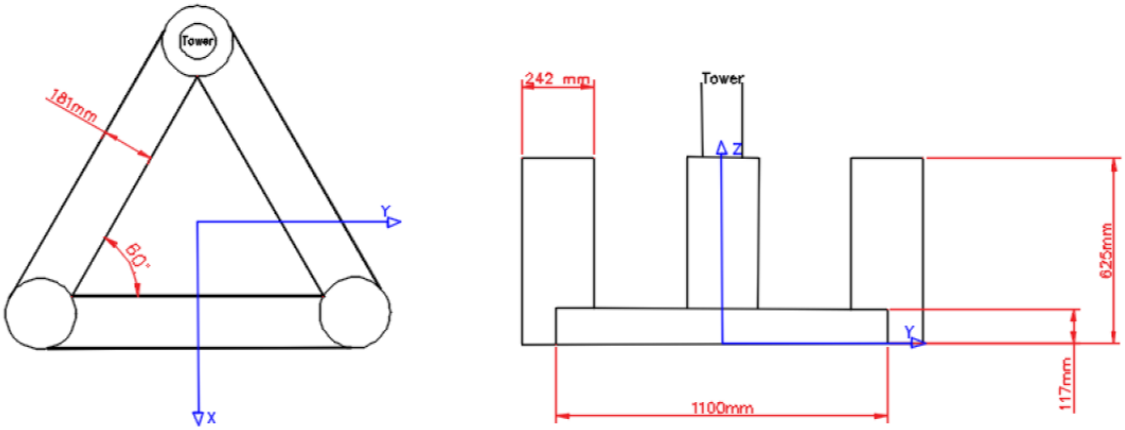

Figure 4.3: Floaters dimensions, in model scale. Taken from [24].

So far, most of the dimensions and parameters provided are in model scale; however, some parameters and results are more interesting to show on full-scale because they can be easier compared with previous and future studies. Thus, it is specified if the parameters are in the model or full-scale to avoid confusion. All the geometric properties are scaled up based on Froude scaling. This research study's scaling factor (λ) is 60 since the model floater is 1/60th of the real floater. All the Froude scaling conversion factors are presented in Islam, Jahra, and Hiscock [59] paper. However, Length, mass, time, force, and moment are the most used here. The following table shows the scaling factor of these five parameters. Finally, table 4.5 shows the dimensions and main parameters of the floater in model and full-scale.

Table 4.4: Main Froude scaling factor used in this report.

Parameter	Units	Scaling Factor	Scaling value
Length	m	λ^1	60
Mass	kg	λ^3	216x10^3
Time	s	$\lambda^{0.5}$	7.746
Force	N	λ^3	216x10^3
Moment	Nm	λ^4	12.96x10^6

Table 4.5: Floater parameters.

Parameters	Model-Scale	Full-Scale
Mass (kg)	118	25.488 tons
Center of gravity z (m)*	-0.205	-12.3
Moment of inertia (kgm^2)	(41.1, 43.9, 46.1)	(3.20,3.41,3.58)x10^{10}
Length x (m)	1.195	71.7
Width y (m)	1.342	80.52
Height z (m)	0.625	37.5
Floater above SWL (m)	0.200	12
Floater under SWL (m)	0.425	25.5
Water-Plane Area (WPA) (m^2)	0.138	497
Volume displaced by the floater (m^3)	0.115	24,923
Center of buoyancy z (m)*	-0.288	-17.28
Water-plane area moment of inertia about y (m^4)	0.0282	3.65x10^5
Projected area in heave (m^2)	0.626	2,254
Projected area in pitch (m^2)	0.486	1,750
Projected area in surge (m^2)	0.520	1,872

*Measure from the (0,0,0) point of the simulation. The z=0 is in the SWL.

Refinement zones

Refining the background mesh to ensure stable simulations and achieve precise outcomes is essential since the interFoam solver is highly mesh dependent. Consequently, this subsection extensively explains both the mesh itself and the refinement zones. However, before delving into the refinement zones specifically, it is good to establish some context regarding the selected mesh for the simulation. The rationale behind choosing this particular mesh is explained in section 4.4 during the mesh convergence study. The designated background mesh utilized in the simulations is characterized by a maximum cell size of 0.133m, thereby dividing the entire domain into 60, 48, and 24 cells along the x, y, and z directions, respectively, resulting in a total number of 69120 cells in the background mesh.

Moving forward with the mesh refinement, the snappyHexMesh utility can apply varying levels of refinement to different regions. In theory, the greater the level of refinement, the more accurate the results; following this reasoning, one might conclude there would be no need for specific refinement regions and instead rely on an extensively refined mesh with exceptionally small maximum cell sizes. However, this approach proves impractical as it would significantly increase the computational costs and time requirements; hence, it would not be optimal. Consequently, the utilization of refinement regions becomes essential as it allows for achieving a higher level of refinement near the zones of interest without incurring an excessive increase in computational resources. How does mesh refinement work in OpenFOAM? The higher the level of refinement, the lower the cell size is; basically, level 0 means the cell stays the same size as the cells from the background mesh. Level 1 divides the cell into four smaller cells, as seen in figure 4.4 for a 2D mesh, and for 3D meshes, the original cell is divided into eight cells.

Wang et al. [13] and Reddy et al. [42] suggest that the zones of interest are the regions near the floater, the heave plates, the air-water interface, and the columns. Therefore, the idea is to use similar regions of refinement like the ones shown on those papers; however, several things change since it is a different floater geometry and mesh. Table 4.6 and figure 4.5 show the refinement zones near the air-water interface and floater. These refinement zones are called boxes for simplicity. In this first refinement, there are four boxes of refinement. Box 1 extends over all the domain for x and y directions. In the z direction, the box goes $\pm$0.125m from the SWL; this covers the air-water interface region since 0.125m represents a wave with an amplitude of 7.5m at full-scale. Boxes 2 and 3 are similar to Box 1, but they extend a higher distance in the z direction and have a lower refinement level. They are needed mainly for a smoother

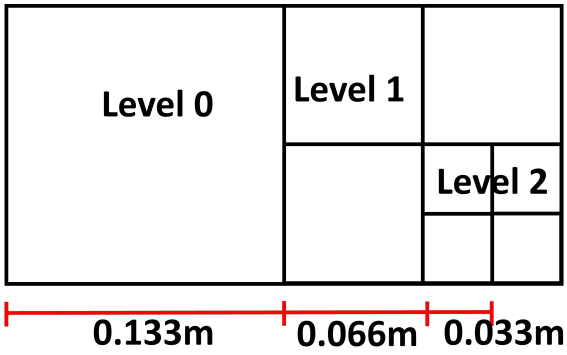

Figure 4.4: Level of refinement.

transition; finally, Box 4 is a cubic region near the floater that encapsulates it completely.

Table 4.6: Refinement zones near the air-water interface and the floater, model scale.

Refinement zones	x Range (m)	y Range (m)	z Range (m)	Level of Refinement
Box 1	All domain	All domain	[-0.125, 0.125]	3 or x/8
Box 2	All domain	All domain	[-0.200, 0.200]	2 or x/4
Box 3	All domain	All domain	[-0.325, 0.325]	1 or x/2
Box 4	[-0.909, 0.591]	[-0.750, 0.750]	[-0.500, 0.250]	3 or x/8

Table 4.6 shows the coordinates and the level of refinement of each box, then figure 4.5 shows a schematic of the same boxes and the way they are supposed to look around the floater. Finally, figure 4.6 shows a close-up of the floater of the actual mesh used for the simulations. In that figure, it is possible to see how the refinement zones look in the mesh and how gradually the cell's size becomes bigger from the SWL toward the rest of the mesh.

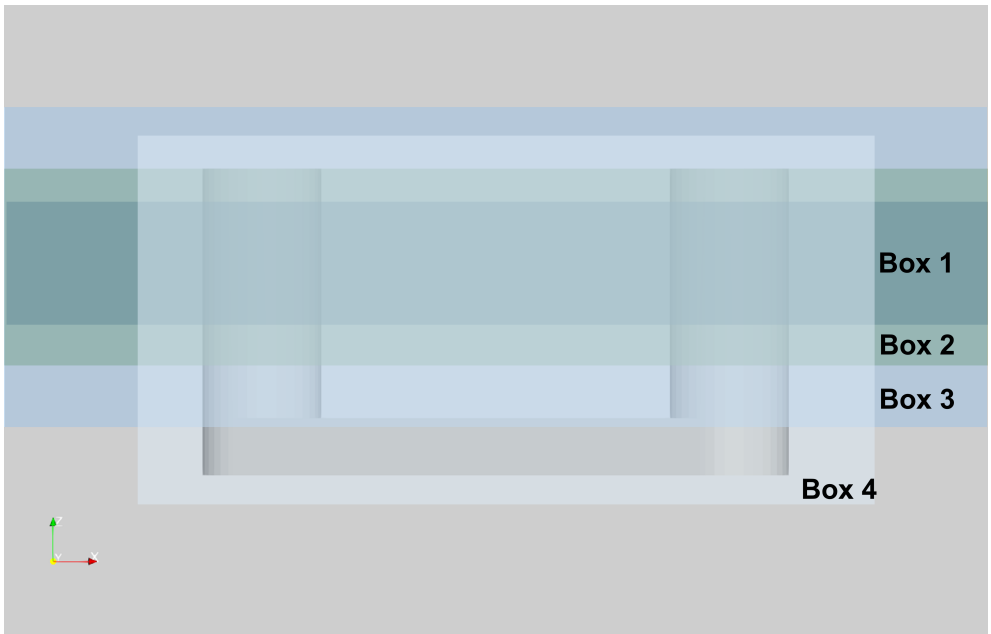

Figure 4.5: Refinement boxes.

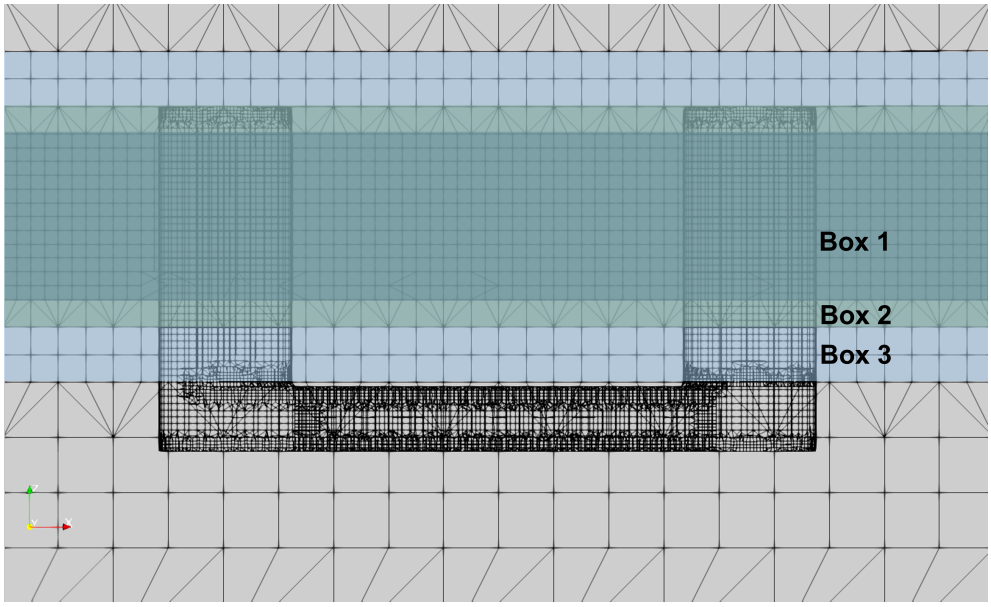

Figure 4.6: Refinement boxes in the mesh.

After performing that first mesh refinement to the regions explained in the previous table and figures, a second refinement is required. This one is to areas near the floater, and since they are highly relevant for the simulation, the level of refinement is also higher. Here a refinement level of 4 is used, leading to a cell size of 0.00833m in these regions. These zones coordinates are given in table 4.7. Furthermore, these coordinates are visually represented in figure 4.7 where it is possible to see that there are four regions, one for each column and one for the heave plates. Ideally, each heave plate should have its refinement zone, and it shouldn't be one for all three; however, two have a rotated axis of 30 degrees, making it harder to set up. Since the region is not that big, it was decided to use only one zone instead of three for simplicity.

Table 4.7: Refinement columns and heave plates near floater, model scale.

Refinement zones	x Range (m)	y Range (m)	z Range (m)	Level of Refinement
Upstream column	[-0.801, -0.469]	[-0.166, 0.166]	[-0.470, 0.245]	4 or x/16
Starboard colomn	[0.152, 0.484]	[0.384, 0.716]	[-0.470, 0.245]	4 or x/16
Port column	[0.152, 0.484]	[-0.716, -0.384]	[-0.470, 0.245]	4 or x/16
Heave plates	[-0.801, 0.484]	[-0.716, 0.716]	[-0.470, -0.263]	4 or x/16

Even though all the refinement zones have been shown, this is still not the final mesh used in the simulations. The mesh is still missing one last step of the *snappyHexMesh* utility. This final step is the addition of layers between the mesh and the geometry; this is required to make the cells transition more smoothly and to try to keep as much as possible hexahedra shape cells. The addition of layers is particularly useful in some regions like the edges or the heave plates where the introduction of the geometry can be abrupt, generating deformities in the mesh, meaning that the cells lose their hexahedra shape. Adding layers is set up in the *addLayersControls* inside the *snappyHexMesh* utility; it is an iterative process. In the controls, the following parameters are defined, the number of iterations, the maximum number of layers desired, and the expansion ratio of the layers. This last parameter makes each layer bigger and bigger from the floater to the rest of the mesh to make a smooth transition.

After the addition of layers, the final mesh used for the simulations is completed. The resulting mesh has approximately a total of 4.5 million cells, most of which are level 3 of refinement. Furthermore, 6 layers are added to the mesh near the floater edges after the adding layer iterations. Figure 4.8 shows a close-up in

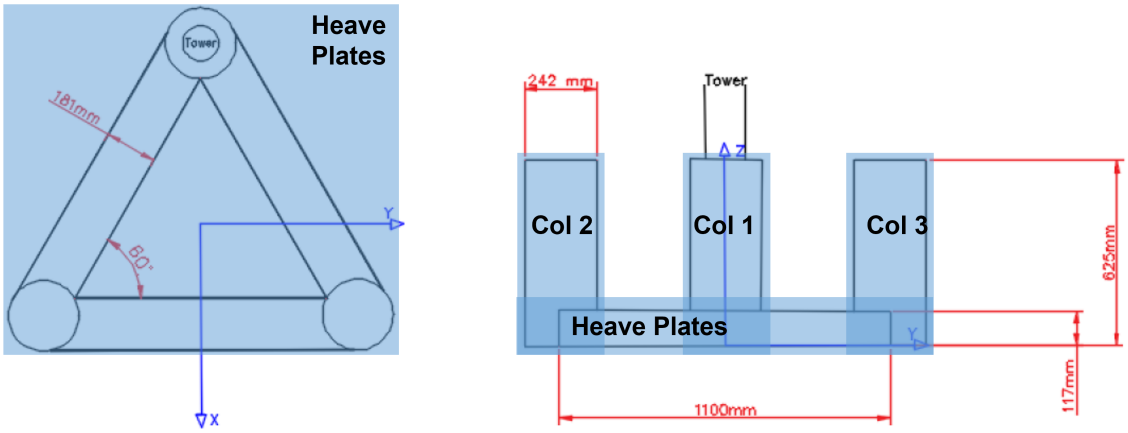

Figure 4.7: Refinement columns and heave plates. Taken and modified from [24].

the xz plane to the heave plate of the mesh. From the figure, it is possible to have a visual understanding of how the refinement zones and the addition of layers work; it is also possible to see the smooth transition from the floater to the rest of the mesh with the addition of layers. More figures of the mesh can be found in the appendix A.

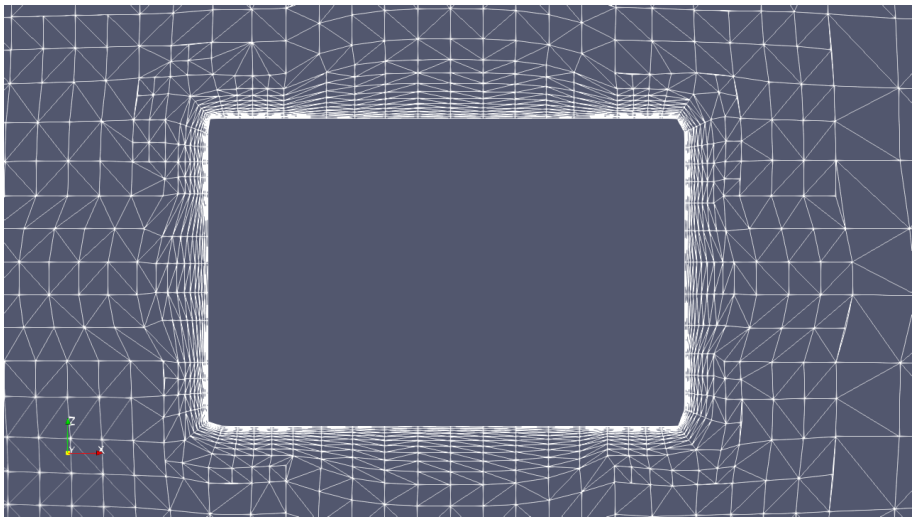

Figure 4.8: Addition of layers to the mesh. Close-up to the stern heave plate in the xz plane.

Mooring lines coordinates and dimensions

This final subsection about the simulation's mesh provides information concerning the coordinates and dimensions of the mooring lines without going into detail about how they were simulated since it was already discussed in subsection 4.2.3. It is important to bear in mind that the mooring lines are exclusively used in the free decay test for model validation, and they are not used in forced oscillatory simulations. However, once the mesh has been validated, it remains unchanged throughout both types of simulations. Thus, it must be ensured that the mesh has adequate dimensions to accommodate the small mooring lines described in the Gueydon et al. [24] report. In this regard, an aerial mooring system with a spread of 4.5m is considered, resulting in mooring lines with a rested length measuring 1.865m. Although the UCC wave tank experiments used the large mooring system setup, the UoS wave tank uses a small configuration. This allows the use of the small mooring system setup for the simulations saving considerably computational resources due to the reduction of the domain.

Table 4.8 shows the main parameters of the mooring lines and the coordinates from the anchor and the fairlead when the floater is in the initial position, and the mooring lines are unstretched. It is important to keep in mind two important points. First, this mooring system is an aerial mooring, which is not possible for a full-scale prototype since floaters are moored to the seabed; however, for the laboratory test and the simulations, it has several advantages, such as the simplicity of setting up for standardization. Second, in table 4.8, anchors refer to the restrain points of the mooring lines outside the floater, and fairleads are the connection of the mooring lines to the floater. Furthermore, figure 4.9 is a visual representation in 3D of the mooring lines attached to the floater; finally, the appendix A has more figures of how the morning should look.

Table 4.8: Mooring line coordinates and main parameters for the simulation.

	Fairlead			Anchor		
Coordinates	x (m)	y (m)	z (m)	x (m)	y (m)	z (m)
Upstream mooring line	-0.756	0	0.625	-2.621	0	0.625
Starboard mooring line	0.403	0.635	0.625	1.335	2.25	0.625
Port mooring line	0.403	-0.635	0.625	1.335	-2.25	0.625
Common Parameters						
Stiffness	21.1 N/m					
Damping	0 Ns/m					
Unstrech length	1.8648 m					

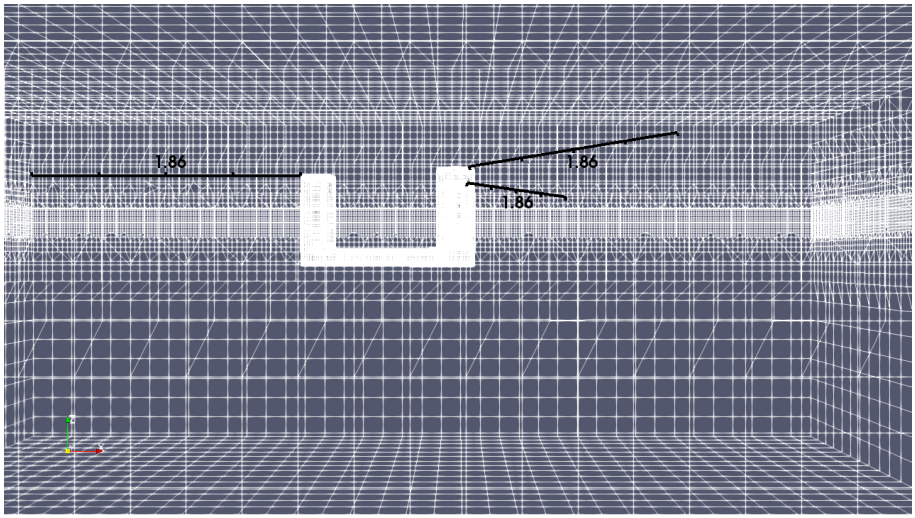

Figure 4.9: Visual 3D representation of the mooring lines in the mesh.

4.4. Mesh convergence study

This section presents a mesh convergence analysis, aiming to show the rationale behind selecting the mesh configuration mentioned above over alternatives with smaller or larger maximum cell sizes. The meshes compared within this study maintain consistent domain boundaries, refinement regions, and added layer controls outlined in the preceding section. Consequently, the main distinguishing factor among the meshes relies on the maximum cell size, directly influencing the total number of cells containing the mesh. By investigating and comparing these different mesh sizes, it is desired to get insights into their impact on the accuracy and the computational resources required for the simulations. By conducting this mesh convergence study, it is expected to justify the selection of the mesh configuration. This section first describes the simulations performed to obtain the mesh convergence results. Then the result of each of

the three desired degrees of freedom, heave, surge, and pitch, are presented. Finally, the discussion of the mesh selection is given.

This mesh study compares nine different meshes, and the parameters of each mesh are presented in table 4.9. Furthermore, the primary assumption of the study relies on the commonly accepted principle in numerical methods and CFD simulations: finer meshes typically yield more accurate results. Given this assumption and the absence of experimental data for comparison, the most refined mesh is designated as a reference point to evaluate the other meshes. Therefore, the most refined mesh has an error percentage of zero in all three motions.

Table 4.9: Parameters of the different meshes used in the convergence study.

Mesh name	# Cells	Larger cell size	# Cells per direction	Layers Added
Mesh 1	1.457x10^7	0.088	(90 72 36)	6.5
Mesh 2	1.002x10^7	0.100	(80 64 32)	6
Mesh 3	6.519x10^6	0.114	(70 56 28)	6
Mesh 4	4.496Ex10^6	0.133	(60 48 24)	6
Mesh 5	2.557x10^6	0.160	(50 40 20)	5
Mesh 6	1.543x10^6	0.200	(40 32 16)	4
Mesh 7	6.936x10^5	0.266	(30 24 12)	4
Mesh 8	2.281x10^5	0.400	(20 16 8)	4
Mesh 9	6.506x10^4	0.800	(10 8 4)	3

The main objective of this convergence study is to find the larger maximum cell sizes mesh that yields accurate enough results. If the results are not compromised with low accuracy, then it is possible to save considerable computational resources by having a larger maximum cell size which results in fewer total cells in the domain, as seen in the previous table.

The study is performed as follows: The simulations follow the forced oscillatory setup for all nine simulations. However, there are two variations. First, the mesh size changes in each simulation. Second, unlike the previous setup, the simulations are concentrated on a single load case. This specific load case shows the following initial conditions: an amplitude of 0.025m, an angular frequency ω of 3.1416 rad/s, and a simulation time of 8 seconds. This duration is chosen to ensure at least three valuable oscillations are captured, with the initial one typically disregarded due to transitional effects. It's important to note that all these values are in the model scale.

After performing the nine simulations per motion, a graph like the one shown in figure 4.10 is obtained. This specific graph is for heave; however, the surge and pitch graphs are very similar and can be found in the appendix B. This plot is normalized to two times the amplitude of the most refined mesh, **Mesh 1**, meaning that it oscillates from 0 to 1. The percentage error is calculated by dividing the absolute value of the average peak comparisons by the average peak value of the most refined mesh. The average peak comparisons is the difference between Mesh 1 and Mesh n average peak values. For a better understanding, the equation 4.7 shows the calculation. Finally, the average peak value is the peak average of the three useful oscillations, remembering that the first oscillation is disregarded due to transition problems.

$$\%error = \frac{|\textbf{Mesh}_\textbf{n} - \textbf{Mesh}_\textbf{1}|}{\textbf{Mesh}_\textbf{1}} x100\% \tag{4.7}$$

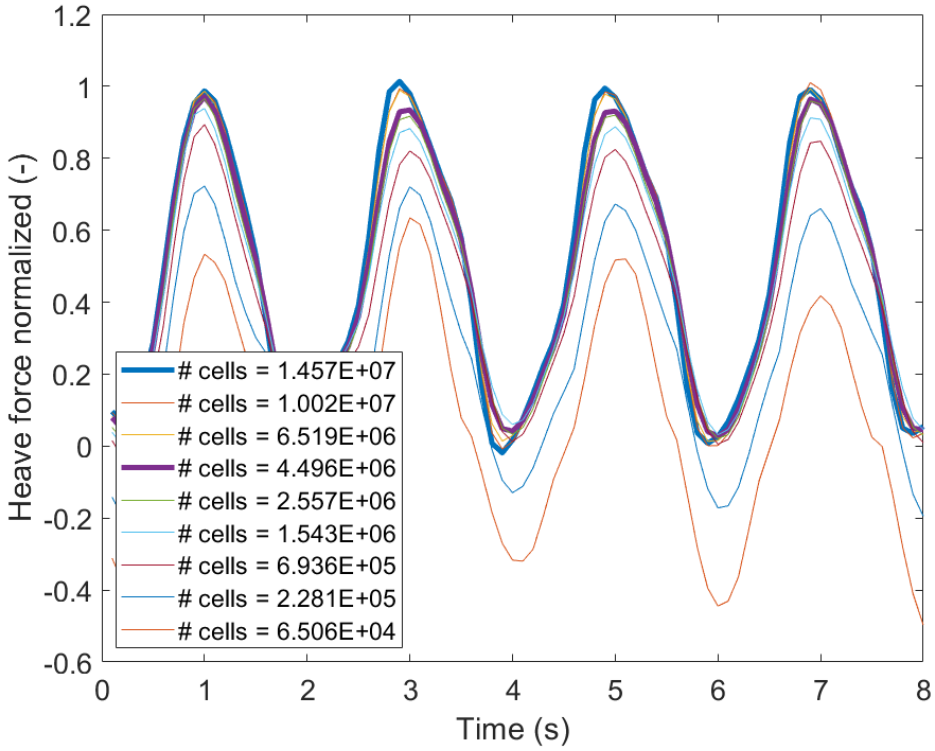

Figure 4.10: Heave mesh convergence simulations.

Figures 4.11, 4.12, and 4.13 show the results of the mesh convergence study for heave, surge, and pitch, respectively. The three figures show in the x-axis the final number of cells in the mesh after refinement with the *snappyHexMesh* utility, in the y-axis the percentage error, and the nine calculated points, one per mesh. From left to right, the points go from Mesh 9 to Mesh 1. It is possible to observe that under the assumption of comparing against Mesh 1, there is a clear trend showing that the finer meshes yield more accurate results; however, there are a few outlier points like Mesh 3 in pitch which has a higher percentage error than less refine meshes, also Mesh 4 in heave and Mesh 5 in surge present some slight deviation from the trend.

From the results presented in these graphs, heave is the motion out of the three that relies more on mesh quality, then pitch, and finally, surge is the less dependent. However, this only applies to this specific load case, and this analysis is used as a reference to decide which mesh to choose for the following simulations. As a side note, mesh quality ensures that OpenFOAM and interFoam algorithms converge to accurate solutions. While a more detailed study of mesh quality could provide valuable insights, the convergence test conducted here is good enough for this analysis.

Continuing with the discussion of the results, it must consider the outcomes of all three motions when selecting an appropriate mesh. Additionally, it is essential to define what can be considered ”accurate enough results”, with a general benchmark of typically accepting errors below 5%. However, it’s worth underlining that this acceptable margin is an assumption and can vary depending on the specific application. Consequently, while all meshes are suitable for surge simulations, the same cannot be said for heave and pitch, where the choice of mesh significantly impacts the accuracy of the results.

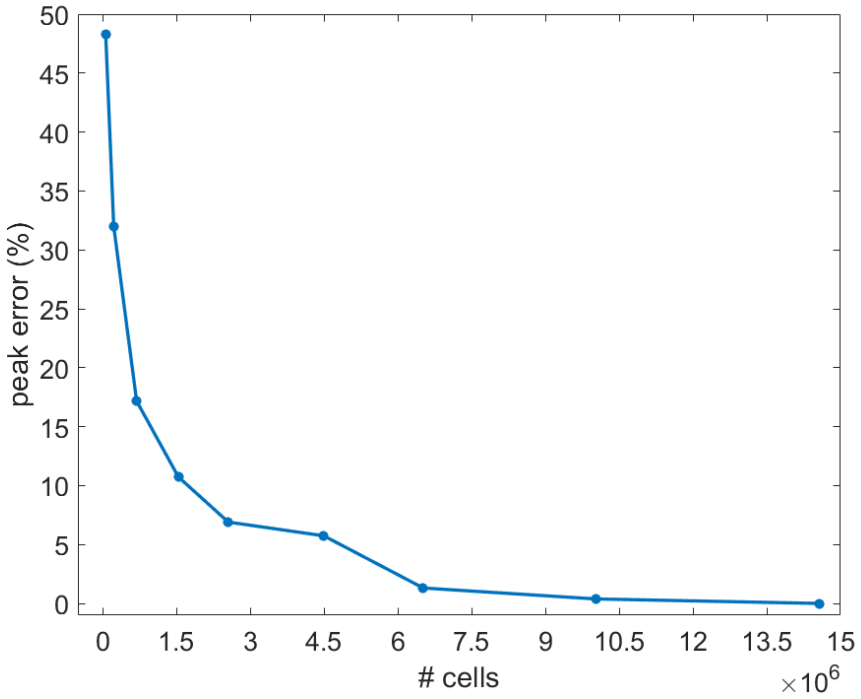

Figure 4.11: Heave mesh convergence, peak percentage error.

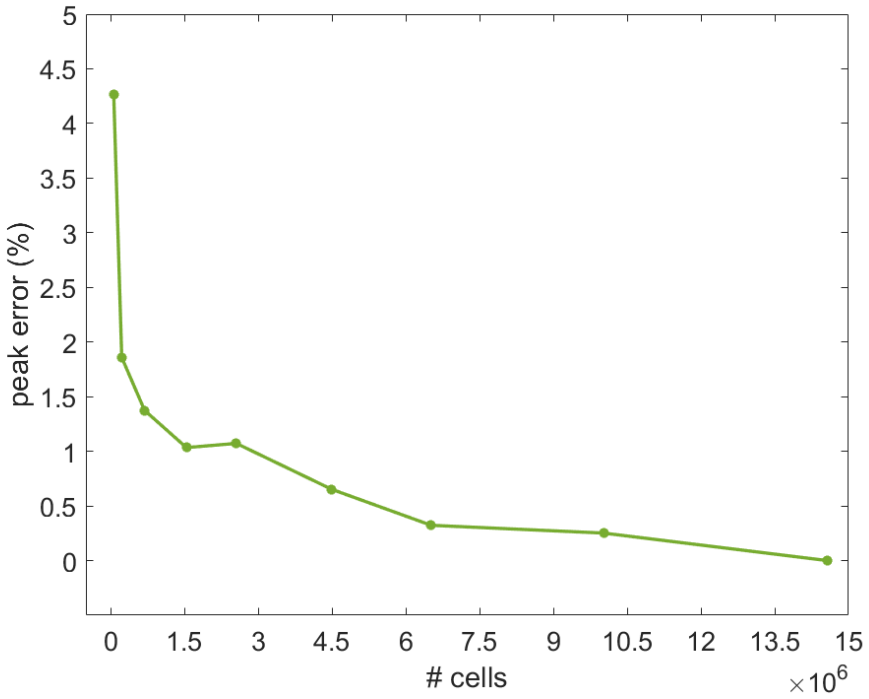

Figure 4.12: Surge mesh convergence, peak percentage error.

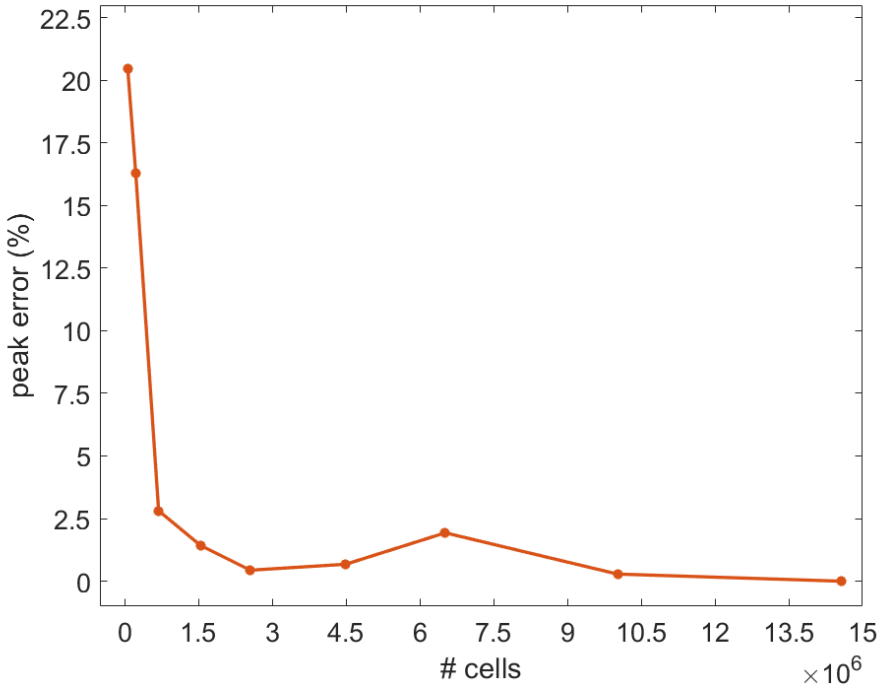

Figure 4.13: Pitch mesh convergence, peak percentage error.

Upon reviewing the results obtained from the three motons, it was decided that **Mesh 4** is the most suitable choice for the upcoming simulations. The rationale behind the decision is as follows:

Remember, the objective is to identify the least refined mesh that provides results within or close to the 5% error. As previously noted, all meshes produce errors below 5% for the surge motion, making them all acceptable options. However, when evaluating the results for pitch, the two less refined meshes are discarded since they don't meet the 5% criteria. With the heave motion results, the decision was reduced to choosing between Mesh 3 and Mesh 4. Mesh 4, besides being slightly above the 5% limit, stood out for two main reasons.

First, it has a considerable difference of 2 million cells less than Mesh 3, a significant factor affecting computational resource requirements and simulation time. Second, while Mesh 4 exhibited a slight deviation from the expected trend, it appeared to align more closely with the 5% error threshold if it followed the anticipated smooth trend.

According to these two considerations, it was decided that the slight extra percentage error in Mesh 4 was preferable to the additional computational resources demanded by the next refined mesh option. Therefore, Mesh 4 was selected as the most practical choice, even though it marginally exceeded the 5% error threshold in heave.

5

Model Validation & Forced Oscillation Results

After the detailed examination of the numerical model and the mesh configurations described throughout the preceding chapters, this chapter is dedicated to the presentation and discussion of the simulation results, utilizing the previously outlined setup and mesh specifications. This chapter is divided into two primary sections to give a structured overview of the findings. Section 5.1 focuses on the validation of the model by presenting the results of the free decay tests. The section also explains the stiffness calibration process used to validate the model. Section 5.2 presents the added mass and drag coefficients obtained from the forced oscillation simulations. These coefficients results are presented per motion.

5.1. Free decay test simulations & validation

The first type of simulations performed in this study are Free Decay Tests. These simulations' primary purpose is to validate the model against experimental data. As previously mentioned, the experimental data used to validate this study's model is from the experiments carried out in UoS wave tank facilities presented in the Gueydon et al. [24] paper. This section is structured in three subsections. The first subsection 5.1.1 explains what it is a free decay simulation and how to perform it on OpenFOAM. Then subsection 5.1.2 develops on the stiffness calibration of the mooring lines. Finally, subsection 5.1.3 presents the results obtained from the free decay simulations.

5.1.1. Free decay test

The free decay simulations are used to determine the natural frequency of the floater for a specific motion, and that natural frequency is used as a comparison to validate it. Therefore, if both natural frequencies (CDF model and wave tank experiments) are the same, the model works properly, or it can be stated that it is validated.

A Free decay simulation test is conducted in the following way: a moored floater is displaced from its equilibrium point by an offset distance value predefined, and then it is released to let it decay. Repeating this simulation for each DoF motion of interest is necessary, and the three DoFs of interest are heave, surge, and pitch. For pitch, instead of displacing the floater, it is offset at a certain angle and then released. The desirable outcome of the simulation is the natural frequency associated with each DoF. As the floater undergoes the decaying motion, it generates a sinusoidal oscillation with decreasing amplitude over time. The natural frequency can be calculated by obtaining the time intervals between two consecutive peaks of this sinusoidal shape motion since the time interval is the natural time period. Furthermore, the free decay tests can be used to determine the added mass and drag coefficients but only at the natural frequency.

These simulations are implemented in OpenFOAM by following the numerical set-up detailed in section 4.2 with a few additions or modifications. First, let's remember this simulation is a moored decay oscillation; hence, the mooring system is required. The mooring lines are placed in the dynamicMesh dictionary with

the *sixDoFRigidBodyMotion* solver as mentioned in the subsection 4.2.3. However, the dynamicMesh dictionary is used to set the mooring lines and the initial offset displacement of the floater before it is released to decay. The program inputs the initial displacement by moving the center of mass from its original point and for pitch by introducing a rotation matrix. This procedure is repeated for each motion with its respective modifications. Table 5.1 presents the initial parameters for each simulation case in model scale as it is input in OpenFOAM and full scale for reference. Finally, it is important to mention that the point displacement and the velocity initial values are kept as zero.

Table 5.1: Free decay test initial parameters. In model scale and full scale.

Motion	Initial Displacement		Simulation Time		Mooring line Stiffness
	Model scale	Full scale	Model scale	Full scale	Model scale
Heave	0.05 m	3 m	20 s	154.9 s	21.1 N/m
Surge	0.03 m	1.8 m	45 s	348.6 s	21.1 N/m
Pitch	5°	5°	25 s	193.6 s	21,1 N/m

5.1.2. Stiffness calibration

The model's validation process consists of comparing the natural frequency obtained in the CFD model and the experimental data obtained from the reference paper. The criterion for affirming the model's validity relies on the alignment of both natural frequencies. To achieve this validation, the first step is the determination of the proper stiffness for the mooring lines. This subsection presents the stiffness calibration procedure to identify the stiffness values that yield the closest agreement with the experimental data. Then, in subsection 5.1.3, the results from the free decay simulations, executed with the selected stiffness parameters, are presented for validating the model.

The reference paper by Gueydon et al. [24] provides two distinct configurations of mooring systems. In the context of this report, the smaller configuration was chosen due to computational resource constraints. This smaller configuration is the same employed in the UoS experiments; therefore, results are compared against the UoS results. Additionally, the reference paper presents three varying mooring line stiffness values. The calibration process conducts simulations with all three stiffness settings to determine which yields the most favorable outcomes. These three mooring line configuration values are detailed in table 5.2 for reference.

Table 5.2: Mooring lines configuration stiffness values.

Option	Wave basin	Stiffness	Damping	Unstrech length
A	Others	19.2 N/m		
B	UCC	21.1 N/m	0 Ns/m	1.8648 m
C	UoS	32.1 N/m		

After conducting the series of nine free decay simulations, three motions per different stiffness values, the natural frequencies were obtained as illustrated in Figure 5.1. This figure provides a visual representation of the findings in model scale, showing the CFD results in blue alongside the UoS experimental wave basin results in orange.

The figure shows that heave and pitch show minimal changes to different mooring line stiffness, while the surge motion demonstrates high dependence on this parameter. These CFD results align with the results shown in the reference report, wherein it is noted that heave and pitch exhibit relatively consistent behavior across various wave basin experiments while surge experiences variations. Additionally, the results highlight the relationship between mooring line stiffness and surge period length, showing that stiffer mooring lines correspond to shorter surge periods.

The lack of dependency on mooring line stiffness for heave and pitch motions can be attributed to specific factors. Firstly, the configuration of the aerial mooring lines is completely horizontal, primarily dedicated to keeping the SS floater in its position. Secondly, as mentioned in chapter 2, the stability of SS floaters comes from the principle of distributed buoyancy, with mooring lines primarily designed to address horizontal loads.

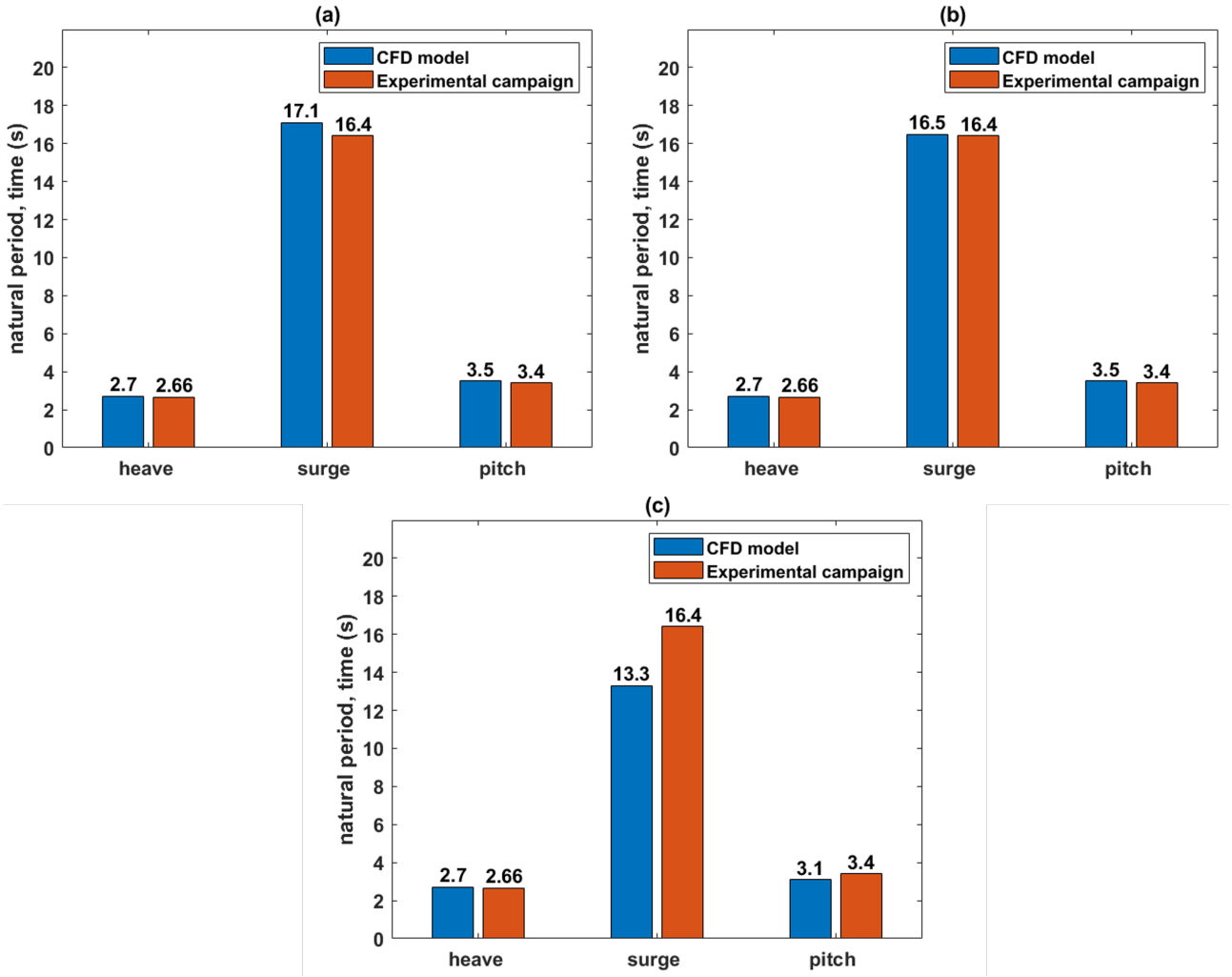

Figure 5.1: Comparison of the natural periods from the UoS wave tank experiments with the CFD simulations using different stiffness values. (a)19.2 N/m, (b) 21.1 N/m, and (c) 32.1 N/m

It was decided to validate the model using the mooring line stiffness value of 21 N/m. Figure 5.1 provides a visual representation, where graph (b) exhibits the closest alignment with the results from the UoS experiments. This alignment is particularly evident in the surge motion, with an error of less than 1%, and in pitch and heave, where the error remains under 3%. On the contrary, the stiffer mooring system graph (c) registers the highest error, with almost 19% in the surge motion. The subsequent subsection presents the results of the free decay simulations conducted with the selected mooring system.

5.1.3. Free decay simulations results

The following three figures 5.2, 5.3, and 5.4 display the outcomes derived from the free decay simulations of heave, surge, and pitch motions, respectively. Let's bear in mind that the results in these figures are in model scale. These graphs share a common structure: the x-axis signifies time measured in seconds. The y-axis presents motion. The main focus of the graphs is to capture the decaying trend from the initial

displacement and the time from one peak to another, which corresponds to the natural period of the motion.

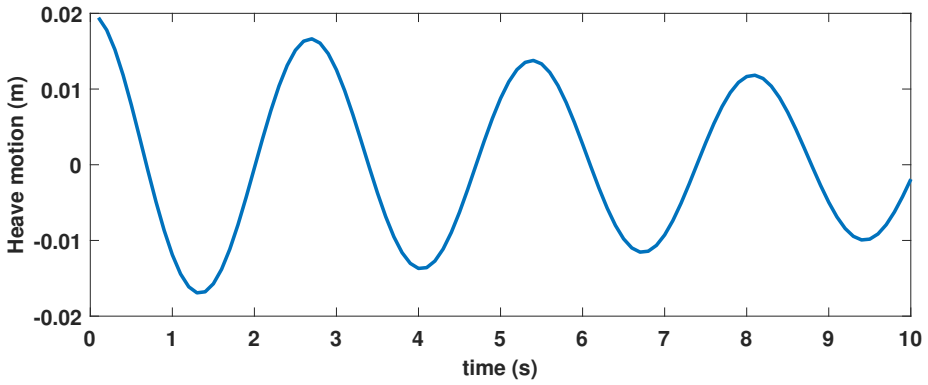

Figure 5.2: Heave decaying motion from the free decay simulation.

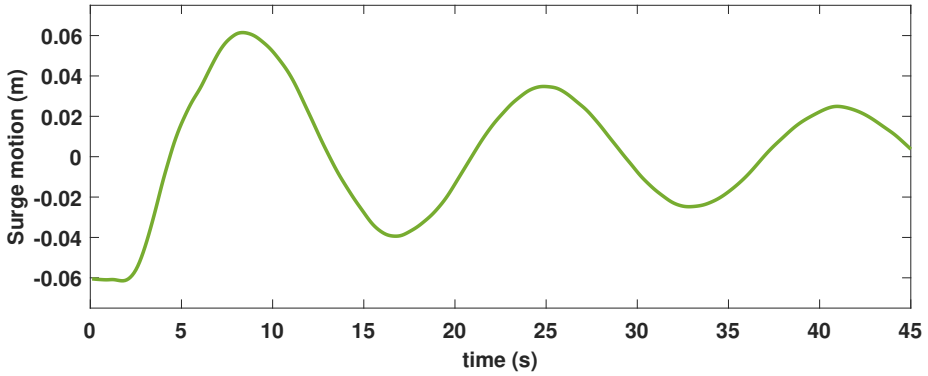

Figure 5.3: Surge decaying motion form the free decay simulation.

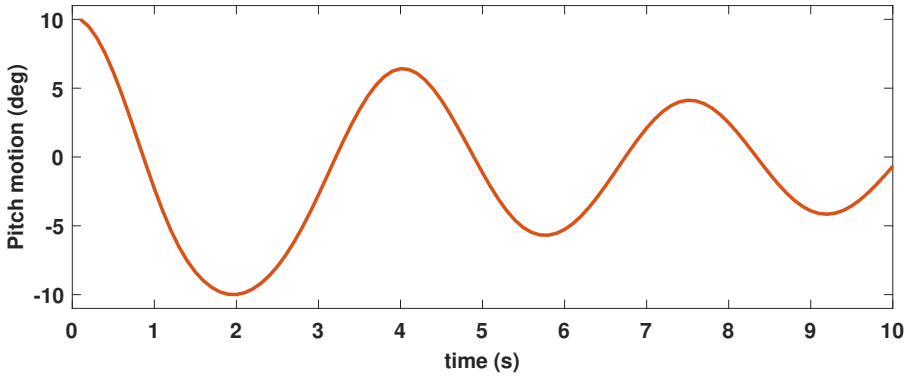

Figure 5.4: Pitch decaying motion from the free decay simulation.

The free decay simulations for heave and surge proceeded smoothly, yielding results as shown in the preceding figures, which clearly illustrate the expected trend of decaying oscillations. Surge and pitch simulations gave the same natural period for pitch motion. The information obtained from these figures defines the natural periods, as shown in figure 5.1 (b). These natural frequencies closely correspond to the values outlined in the reference paper. Based on these results, we can affirm the validation and that

the model is working. With this validation in place, It is possible to proceed to explore the results of the forced oscillation simulations.

5.2. Forced oscillatory simulations

After validating the model with the results of the free decay test, it is possible to conduct the second type of simulation performed in this study, the forced oscillatory simulation. While the previous subsection provides insight into the free decay test, this subsection explains the forced oscillatory simulations. The purpose of these simulations is to determine the added mass and drag coefficients of the SS floater, which is the main objective of the paper. This section is divided into three subsections. Subsection 5.2.1 explains what is a forced oscillatory test and how to simulate it in OpenFOAM. Then subsection 5.2.2 explains how to obtain the added mass and drag coefficients from the forced oscillatory simulations results. Finally, the forced oscillation results and the calculated added mass and drag coefficients are presented in subsection 5.2.3.

5.2.1. Forced oscillatory simulations description

A force oscillation simulation imposes a sinusoidal motion into the SS floater with a specific amplitude and frequency. By imposing this sinusoidal movement, it is possible to determine the added mass, drag coefficient, and more parameters for different frequencies compared to the free decay test, which only allows getting parameters for the natural frequency. However, like the previous simulations, forced oscillatory simulations must be performed per motions of interest. Furthermore, With this simulation type, it is possible to observe a clear advantage of CFD and numerical simulations over experimental tests since this type of test is relatively easy to perform by numerical simulations compared to a wave basin experiment. The sinusoidal motion of the floater is represented with a standard sine equation; it is shown in the following equation together with the relation between the time period and the motion angular frequency.

$$X(t) = A \sin(\omega t) \tag{5.1}$$

$$T_p = \frac{2\pi}{\omega} \tag{5.2}$$

where X(t) is the displacement in meters or degrees, depending on the motion, A is the amplitude, t is the time step, ω is the angular frequency, and T_p is the time period of the oscillation. Hence, the initial values required for this simulation are the amplitude and frequency.

5.2.2. Added mass and Drag coefficient calculations

After running the simulations with the numerical method, the outcomes are the SS floater motion and the total forces experienced by the floater. However, the interest is the added mass and drag coefficients, which are calculated by using the Fourier Averaged method in one time period of the hydrodynamic force or moment series. The following equations show the Fourier averaged coefficients as presented in Reddy et al. [42] paper. Equation 5.3 and 5.4 are used to calculate added mass for translational and rotational motion, respectively. Similarly, equations 5.5 and 5.6 are used to calculate the drag coefficient, the first for heave and surge, and the second for pitch.

$$C_a = \frac{1}{\pi \rho V_d \omega A} \int_0^T F_H(t) \sin \omega t dt \tag{5.3}$$

$$C_{a,\phi} = \frac{1}{\pi I_y \omega A} \int_0^T M_H(t) \sin \omega t dt \tag{5.4}$$

$$C_d = \frac{-3}{4\rho A_s \omega A^2} \int_0^T F_H(t) \cos \omega t dt \tag{5.5}$$

$$C_{d,\phi} = \frac{-3}{4\rho A_s D \omega A^2} \int_0^T M_H(t) \cos \omega t dt \tag{5.6}$$

where C_a and C_d are the added mass and drag coefficients per motion, ρ is the density, V_d displaced volume of the floater, ω the angular frequency, A the amplitude, I_y the y moment of inertia, A_s the projected area of the floater, D the distance from the center of mass to the SWL, F_H the hydrodynamic force, and M_H is the hydrodynamic moment. Furthermore, from the equations, it is also possible to see that the added mass is related to the component of the force in-phase and the drag coefficients with the out-of-phase.

However, the hydrodynamic force must be calculated before using the previous equations to calculate the coefficients. As mentioned in chapter 2 in subsection 2.2.4, the total force on the floater is composed of three elements: the hydrodynamic, the hydrostatic restoring, and the radiation-damping forces. However, according to Wang et al. [13] paper, the effects in SS floaters are dominated by viscous drag, and wave radiation can be neglected; hence, equation 5.7, 5.8, and 5.9 shows how to calculate the hydrodynamic forces for heave, surge, and pitch, respectively. It is important to mention that for pitch, instead of using hydrodynamic force, the hydrodynamic moment is used.

$$heave \rightarrow F_{H,33}(t) = F(t) - F_{K,33}(t) - F_b \tag{5.7}$$

$$surge \rightarrow F_{H,11}(t) = F(t) - F_{K,11}(t) \rightarrow F_{K,11}(t) = 0 \tag{5.8}$$

$$pitch \rightarrow M_{H,55}(t) = M(t) - M_{K,55}(t) \tag{5.9}$$

where $F(t)$ and $M(t)$ are the total forces and moments directly as outcomes from the simulation, the $F_{H,33}(t)$ is the specific hydrodynamic force of heave as $F_{H,11}(t)$ and $M_{H,55}(t)$ are for surge and pitch. Furthermore, F_b is the hydrodynamic force constant calculated with the floater's parameters as shown in equation 2.1. The 33 indicates the heave motion; it is the coordinates inside the six-by-six matrix of the 6DoF expressing the third column and third row. For surge, it is 11, and for pitch, it is 55. Finally, $F_{K,11}(t) = 0$ in surge motion, for heave and pitch are shown in the following equations:

$$F_{K,33}(t) = \rho g A_w z(t) \tag{5.10}$$

$$M_{K,55}(t) = pg(V_d Z_b + I_{yy})\phi(t) \tag{5.11}$$

where A_w is the water-plane area, $z(t)$, is the vertical location of the floater, V_d is the displaced volume, Z_b the vertical distance from the center of buoyancy to the SWL, which is the 0 coordinate of the simulation in the z-direction, I_{yy} is the area moment of inertia in the y-plane, and $\phi(t)$ the pitch angle of the floater [42].

After understanding the equations and methodology used to calculate the added mass and drag coefficients from the outputs of the CFD simulations, let's shift back the focus to the inputs used for the simulations. Tables 5.3, 5.4, and 5.5 present the load cases for heave, surge, and pitch simulated in the CFD numerical model, respectively. The tables show the total 30 different load cases performed, and the values are presented in model scale and full scale for reference and comparison; however, it is specified in which scale the values are.

These simulations' implementation in OpenFOAM are performed by closely following the model setup outlined in the previous section. However, two specific modifications or additions are required in the setup:

1. In the dynamicMesh dictionary, instead of using the *sixDoFRigidBodyMotion* solver, like in the free decay test, the *displacementLaplacian* solver is used. In this solver, diffusivity is the only parameter required, and there are no mooring lines. The Laplacian is used to impose sinusoidal motion in the forced oscillatory simulations.
2. The point displacement initial parameter must be modified. Rather than leaving the SS floater patch as a calculated type with an initial value of 0, an imposed oscillating displacement function is used. This function uses as input the parameters of the load cases; thus, the angular frequency $omega$ and the amplitude. Likewise, for pitch, the function used is an angular oscillating displacement, which has the same inputs plus the desired axis of rotation.

Table 5.3: Heave load cases for the Forced oscillatory simulations.

Load Case	**Amplitude (m)**		**Oscillation time (s)**		**Simulation time (s)**		**Angular frequency (rad/s)**
Scale	Model	Full	Model	Full	Model	Full	Model
H_1.1	0.025	1.5					
H_1.2	0.05	3	3.873	30	15	116.2	1.6223
H_1.3	0.125	7.5					
H_2.1	0.125	1.5					
H_2.2	0.05	3	5.164	40	21	162.7	1.2167
H_2.3	0.025	7.5					
H_3.1	0.125	1.5					
H_3.2	0.05	3	6.455	50	26	201.4	0.9734
H_3.3	0.025	7.5					

Table 5.4: Surge load cases for the Forced oscillatory simulations.

Load Case	**Amplitude (m)**		**Oscillation time (s)**		**Simulation time (s)**		**Angular frequency (rad/s)**
Scale	Model	Full	Model	Full	Model	Full	Model
S_1.1	0.025	1.5					
S_1.2	0.075	4.5	2.582	20	10.5	81.3	2.4335
S_1.3	0.150	9					
S_2.1	0.025	1.5					
S_2.2	0.075	4.5	6.455	50	26	201.4	0.9734
S_3.3	0.150	9					
S_3.1	0.025	1.5					
S_3.2	0.075	4.5	12.91	100	40	309.8	0.4867
S_3.3	0.150	9					
S_4.1	0.025	1.5					
S_4.2	0.075	4.5	19.365	150	60	464.8	0.3245
S_4.3	0.150	9					

Table 5.5: Pitch load cases for the Forced oscillatory simulations.

Load Case	Amplitude		Oscillation time (s)		Simulation time (s)		Angular frequency (rad/s)
Scale	Model	Full	Model	Full	Model	Full	Model
P_1.1	0.05m	3°					
P_1.2	0.125m	7°	2.582	20	10.5	81.3	2.4335
P_1.3	0.150m	9°					
P_2.1	0.05m	3°					
P_2.2	0.125m	7°	3.228	25	12	93	1.9468
P_2.3	0.150m	9°					
P_3.1	0.05m	3°					
P_3.2	0.125m	7°	3.873	30	15	116.2	1.6223
P_3.3	0.150m	9°					

5.2.3. Forced Oscillation Results

This subsection presents the added mass and drag coefficients calculated using the Fourier added method explained in subsection 5.2.1. The computation relies on the force and moment data extracted from the forced oscillation simulations. The subsection is divided into three parts, one per motion. It's important to note that all results showed in this section are presented in full scale, facilitating the comparison and analysis. Moreover, given that this is the first instance of conducting these simulations for the particular SS floater in this report, there exists no specific dataset available for a direct result comparison. However, it is still feasible to compare the findings against relevant research from other studies that have done similar simulations for different floaters. Such comparative analysis can provide valuable insights and context for the results.

Heave forced oscillation results

The added mass and drag coefficients of the nine load cases related to heave motion are presented in figure 5.5. The figure contains two graphs: on the left-hand side, the added mass results, while on the right side, the drag coefficients are displayed. Both graphs share a common x-axis, representing the oscillation period measured in seconds, while the y-axis shows the values for the added mass and drag coefficients.

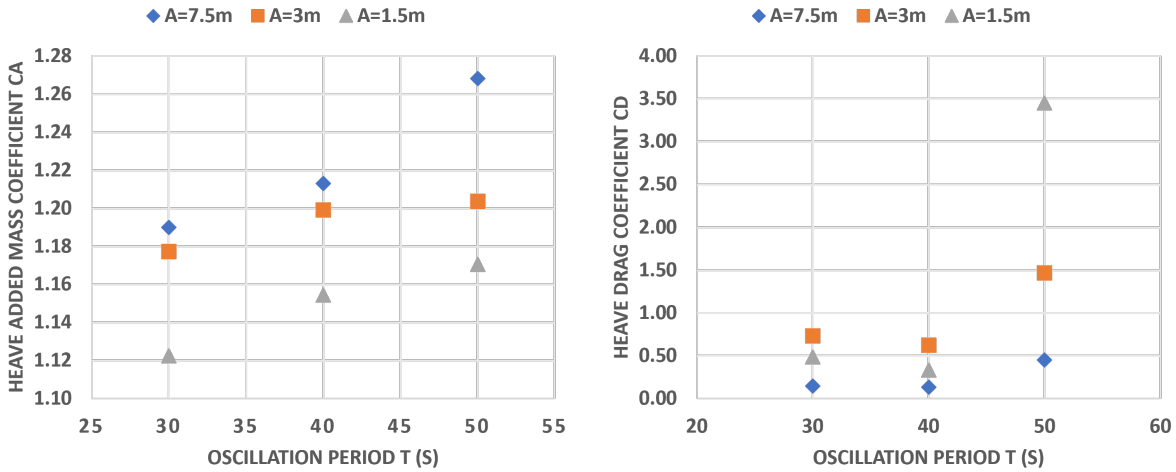

Figure 5.5: Heave added mass and drag coefficients.

The figure illustrates a consistent trend where the added mass coefficients increase in response to both the

amplitude and period of oscillation. This pattern holds true across all load cases, although the increase in the 40s to 50s load case for the amplitude of 3 meters is comparatively low in contrast to the other cases.

The results exhibit some alignment with the findings in Li and Bachynski-Polić [48]'s paper, as both studies indicate that the added mass coefficients tend to increase with greater oscillation amplitudes. However, there is a noticeable difference in terms of oscillation period behavior. In the referenced paper, the added mass remains relatively consistent across different oscillation periods, whereas in the current report, a significant increase is visible. It is worth noting that another study, Reddy et al. [42] paper, also found a similar trend of increased heave added mass coefficients with oscillation period. In this case, the periods simulated in Reddy et al. [42]'s paper are more closely aligned with those in the current report, providing additional context for the observations. Furthermore, the actual added mass values presented in figure 5.5 are similar to those in [48], with slightly smaller magnitudes. This variation can be attributed to the floater's differences, which have smaller heave plates making it less dominant to flow separation, which influences the magnitude of added mass coefficients.

The second graph within figure 5.5 provides the drag coefficient outcomes of the nine heave load cases. Upon an examination of the figure, it is possible to observe that larger oscillation amplitudes correspond to lower drag coefficients.

Furthermore, the oscillation period on drag coefficients does not show a clear trend. For the most part, shorter periods exhibit a relatively low influence on drag coefficients, with only minor fluctuations; however, for the case of T=50s, the drag coefficients experience a considerable increase. This anomaly could be interpreted in two ways: either the T=50s results represent outliers for heave drag coefficients, or these results are correct, and higher oscillation periods induce a considerable increase in these coefficients.

In light of these observations, comparing the findings with Reddy et al. [42] provides valuable insights. The referenced paper suggests that the oscillation period has minimal effects on drag coefficients. Therefore, when assessing the current report results, the T=50s points may indeed be outliers within the heave drag coefficient data. This difference suggests future exploration with more load cases.

Surge forced oscillation results

Twelve load case simulations were conducted for surge, and the corresponding added mass and drag coefficients are presented in figure 5.6. As with the heave motion, this figure is divided into two graphs, with the left side displaying the added mass data and the right side presenting the drag coefficients.

Upon examining the figure, it is visible that there is no distinct added mass trend concerning the oscillation period, as the trend initially exhibits a decrease followed by an increase. However, it is possible to observe a consistent increase in added mass with larger amplitude oscillations, indicating that oscillation magnitude influences the results.

When comparing the results with those of Li and Bachynski-Polić [48] paper, several key interest points emerge. First, the actual coefficient values of the current report are similar to those in the referenced paper, assuring that the results are well within the expected range. The present report coefficients exhibit slightly larger magnitudes, which can be attributed to the larger displaced volume inherent in the floater's design. However, there is a discrepancy in the trend observed for oscillation amplitudes, which may be attributed to the specific geometry of the floater. Further investigations are recommended to understand and detail the reason for these differences.

Furthermore, the results in Li and Bachynski-Polić [48] paper indicate a consistent increasing trend with oscillation period, which differs from the findings of the current report. Figure 5.7 was generated to explore this further, excluding the 20s load cases. Without these values, a clear increasing trend is visible, with the exception of one data point, potentially suggesting that the 20s load cases could be considered outliers.

One reason for being considered outliers could be their high-frequency nature, distinct from the reference paper, where the shortest period is 67s. Also, throughout the current report simulations, high-frequency forced oscillations presented certain problems across all three motions, which could further explain this disparity.

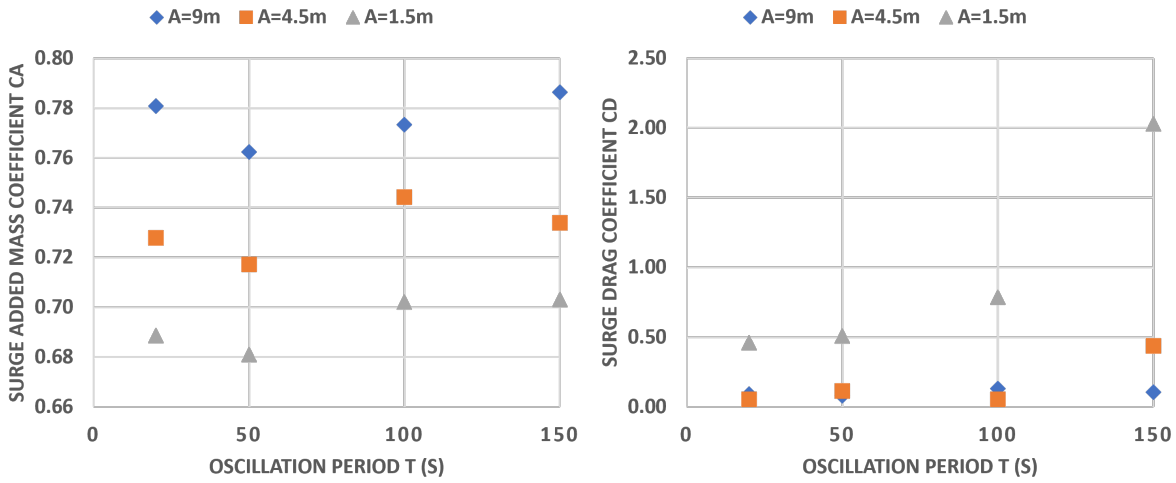

Figure 5.6: Surge added mass and drag coefficients.

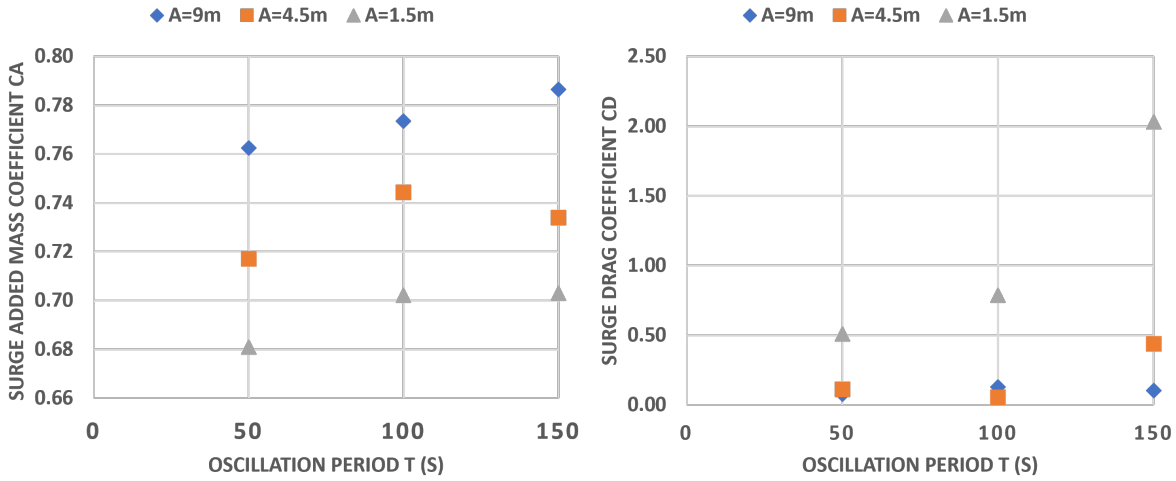

Figure 5.7: Surge added mass and drag coefficients without the 20 seconds data sets.

The results present a prominent trend within the context of surge motion drag coefficients. There is an increase in drag coefficients for low and mid-magnitude oscillation amplitudes when there is an increasing oscillation period. In contrast, when dealing with high oscillation magnitudes, the oscillation period has no effect on the coefficients. Additionally, it is observed that higher oscillation amplitudes correspond to lower drag coefficients, as shown in both figure 5.6 and figure 5.7.

The previous observations are in agreement with the findings in the two reference papers [42, 48]. In both cases, the two trends are clearly visible. First, higher oscillation amplitudes are consistently associated with lower drag coefficients, and second, there is an increase in drag coefficients as the oscillation period grows, except in high oscillation magnitudes where the effect is minimal. The alignment of these trends between the reference papers and this present study supports the results' validity and provides insight into

the behavior of surge coefficients for different conditions.

Pitch forced oscillation results

This subsection presents the added mass and drag coefficient results of the pitch motion, which marks the final component of the report. Figure 5.8 shows the outcomes in the same way heave and surge were presented, with added mass on the left and drag coefficients on the right.

When analyzing the added mass results of the figure, a distinct trend is visible. The graph illustrates a pronounced and consistent increase in added mass coefficients with oscillation period. A clear ascending trajectory characterizes this trend. Furthermore, the magnitude of the oscillations exerts minimal influence on the results, as seen from the data, since all the data points from one period have almost the same value.

Several interest points are observed when comparing with the findings in Li and Bachynski-Polić [48] paper. First, there is an evident contrast in the observed trend between the two reports. The results of figure 5.8 show a consistent increase in added mass coefficients as oscillation period increases, while the referenced paper reports a slightly decreasing trend. This discrepancy raises questions regarding whether the difference is attributed to the floater's geometry or to the simulation models employed and suggests that further investigation of the SS floater is required.

Conversely, an area of concordance between the two reports is the minimal effect of oscillation amplitude on the results. Both reports findings present a similarity in terms of the limited variation in added mass coefficients across oscillation magnitudes. Suggesting that the effects of the oscillation amplitude have a minimal effect on the pitch added mass coefficients.

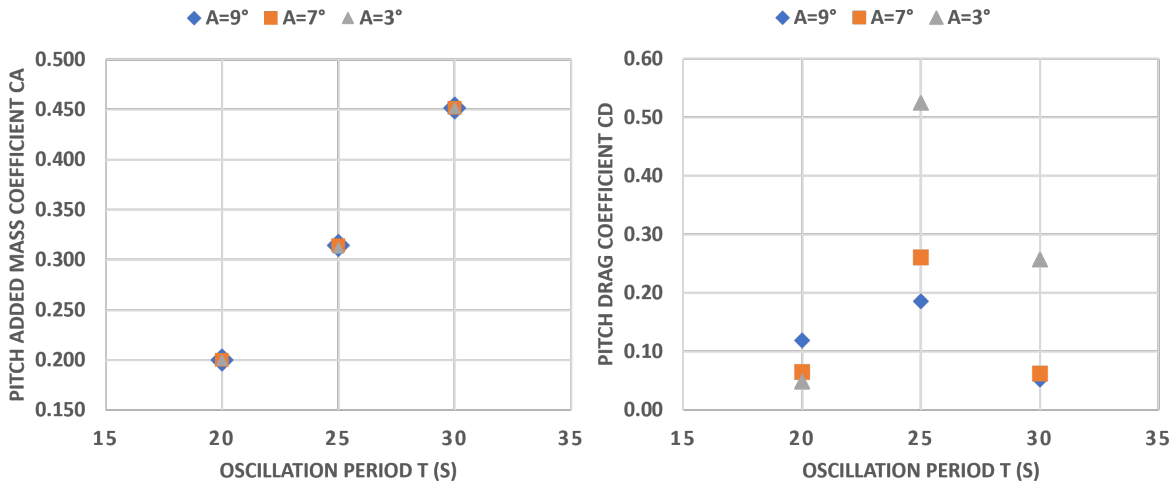

Figure 5.8: Pitch added mass and drag coefficients.

Finally, the pitch drag coefficient results are presented in the right graph of figure 5.8. This figure shows the behavior of drag coefficients for two specific oscillation periods, with an important observation: drag coefficients exhibit an increase at smaller angles. While this outcome was expected across all oscillation periods, the slight divergence observed might be attributed to numerical accuracy within the CFD model. Since the difference in the 20 second oscillation period values remains minimal among the three angle variations.

Moreover, there is no clear coefficient trend concerning the increasing oscillation period. In accordance with reference papers, a trend where drag coefficients remain relatively stable was expected, showing

neither increases nor decreases with changing oscillating periods. However, the results of this report differ from this expected trend since, as observed from the figure, a substantial increase is seen in the 25 seconds values, followed by a return to values that closely resemble their initial position.

A possible explanation for this unexpected increase is that 25 seconds corresponds to the natural frequency of the pitch motion. Consequently, the considerable increase in drag coefficients at this specific period value becomes more comprehensible. In light of this, it becomes apparent that the pitch drag coefficient exhibits minimal variation concerning oscillation period, except when it aligns with the pitch motion's natural frequency.

6

Conclusions & Recommendations

This final chapter presents the conclusions drawn from the study's findings and suggests recommendations for future work. It is structured into three sections: Section 6.1 offers a discussion that addresses the sub-research questions, then section 6.2 presents the conclusion of the main research question and the objective of the report. Finally, section 6.3 outlines recommendations for future work based on the challenges encountered and insights gained throughout the report.

6.1. Research question discussion

This study was structured around two sub-questions to accomplish the primary objective and address the main research question outlined in chapter 1. The two sub-question have two follow-up questions used to give extra structure and a simple understanding of the report. This section addresses and presents the answers to the questions as follow:

1. How is a CFD model setup and validated to simulate the MaRINET2 semi-submersible floater?

This question is addressed in chapter 4 in detail, which provides an explanation of the simulation setup used. In general, the CFD model was configured using the inteFoam solver within OpenFOAM. The inteFoam solver is specifically designed for simulating two incompressible, isothermal, and immiscible fluids. To represent the semi-submersible floater's geometry, an STL file is employed, and the floater is simulated as a rigid body.

For validation against experimental wave basin results, free decay simulations were used, a method commonly used in similar studies. In this thesis, the model is validated against experimental data obtained from the UoS wave tank facilities, as reported in the Gueydon et al. [24] paper. The free decay simulations utilize the *sixDoFRigidBodyMotion* solver within the dynamicMesh dictionary, allowing to input parameters for both the floaters and mooring lines.

The principle behind free decay simulations involves initially displacing the moored floater from its equilibrium position and subsequently observing its decay in motion. This process serves as a means to validate the numerical model.

To gain a better understanding of the mesh used and the modeling of mooring lines, the following two sub-questions are formulated:

1.1. How are the mooring lines simulated to be able to validate the model?

To address this research sub-question, it was decided to use an approach considering the simulation accuracy needed while optimizing computational resources. The goal was to closely replicate the conditions outlined in the validating papers, thus ensuring the reliability and accuracy of the numerical model. To this end, the mooring lines were simulated as linear springs within a quasi-static model. This choice was taken to find a balance between the required level of accuracy for validation while maintaining model simplicity.

This approach has been used successfully in previous research papers.

A significant difference from traditional SS floater mooring systems was made. SS floaters normally use a catenary configuration for mooring lines. This report opted for an aerial mooring system. This choice was driven by the fact that the wave basin experiment used for validation also implemented an aerial mooring system. It was a priority to this study's objectives that the simulation closely mirrored the experimental setup, thus justifying the modeling of the mooring lines in the same manner.

Furthermore, the reference paper [24] provided details on two distinct mooring systems, each with sufficient information for modeling and results for comparative validation. It was decided to use the smaller of the two mooring systems. By selecting the smaller mooring system, it was possible to scale down the computational domain effectively and reduce computational resources without compromising the result's accuracy. A stiffness study was also undertaken to pinpoint the stiffness parameter that yielded results most congruent with those observed in the wave basin experiments.

In summary, the approach to simulating mooring lines was structured to align with the conditions in the validating paper while minimizing computational demands. The representation of mooring lines as linear springs within a quasi-static model, the emulation of an aerial mooring system, the selection of a smaller mooring system, and the stiffness study all contributed to a smaller computational domain without compromising the accuracy of our results.

1.2. How should the mesh be defined for the simulation to be grid-independent and achieve accurate results?

Achieving accurate results in CFD simulations is highly dependent on the mesh's quality and refinement level. In addition, interFoam, the chosen solver within OpenFOAM, is known for its sensitivity to mesh quality. However, the pursuit of an excessively refined mesh can take a substantial amount of computational resources and simulation time, creating the need for an optimal balance.

To find this balance, a structured approach was adopted. First, the areas of interest within the simulation domain were refined. These regions include the air-water interface, the floater, the heave plates, and the buoyancy columns. Then to ascertain the minimal mesh refinement required to maintain result accuracy, a mesh convergence study was conducted. This study aimed to identify the most optimal refinement mesh for this report's proposes. The established parameter was the commonly accepted threshold of a 5% error margin, ensuring that any selected mesh configuration would deliver results within this acceptable range.

A challenge in this mesh study was the absence of experimental data for direct result comparison. For that, a reference point was established using the most refined mesh configuration. This reference point was assumed to yield accurate results, serving as a baseline for comparison. It is important to acknowledge that this assumption was made out of necessity due to the lack of experimental data, and it is sustained with literature where it is mentioned that more refined meshes yield better results.

Following an examination of various mesh refinements, a mesh of approximately 4.5 million cells was selected as the optimal choice. This mesh configuration has a maximum cell size of 0.0133 meters and a total of eight refinement regions in the zones of interest. The detailed mesh description is presented in chapter 4.3, providing further insights into its composition and structure.

2. How are the added mass and drag coefficient obtained from a CFD simulation?

To address this sub-question, the two follow-up questions are explored before answering this one. By doing so, it can provide a clearer understanding of the process involved in obtaining the added mass and drag coefficient from a CFD simulation.

2.1. What type of simulation is required to obtain the hydrodynamic parameters for different amplitudes and frequencies?

To determine the necessary simulation approach for obtaining the desired hydrodynamic parameters across various amplitudes and frequencies, it is important to consider the methodology employed. In the report, the forced oscillatory simulations were used, with the ”displacementLaplacian” solver within the dynamicMesh dictionary. These simulations perform controlled oscillations and offer a means to calculate the essential hydrodynamic coefficients.

For the analysis, our forced oscillatory simulations subject the floater to continuous oscillations with defined frequencies and amplitudes in pre-defined motion directions. This dynamic simulation setup facilitates the calculation of the hydrodynamic coefficients essential to the research.

2.2. What methodology should be followed to obtain the added mass and drag coefficient from the simulation outcomes?

Understanding the methodology for extracting the added mass and drag coefficients from simulation outcomes is important. The process begins with the generation of a data-set detailing the total forces acting on the floater obtained with the forced oscillatory simulations.

As explained in chapter 5, the Fourier-averaged method is used to calculate these coefficients. This method focuses on a single time period of hydrodynamic force data. Added mass coefficients are determined using equations 5.3 and 5.4, while drag coefficients are computed through equations 5.5 and 5.5.

However, it must be recognized that the simulation outcomes encompass the cumulative effect of all forces acting on the floater. To isolate the hydrodynamic forces, the hydrostatic restoring forces are subtracted from the total force. This step is necessary as the dominant effects experienced by SS floaters primarily consist of viscous drag. This leads to the assumption that the sum of hydrostatic restoring forces and hydrodynamic forces constitutes the total force acting on the floater.

With the knowledge of the preceding two questions, it is possible to address the primary research sub-question: ”How are the added mass and drag coefficients obtained from CFD simulations at different amplitudes and frequencies?”

To obtain the added mass and drag coefficients from CFD simulations at varying amplitudes and frequencies, the process involves conducting a forced oscillatory simulation, which yields a dataset of total forces acting on the floater. From this dataset, hydrodynamic forces are extracted by subtracting hydrostatic restoring forces. Utilizing the Fourier-averaged method for a single time period, added mass and drag coefficients can then be calculated.

6.2. Conclusions

The discussion of the previous research sub-question structured the study to accomplish the main objective of this thesis, which is restated here for convenience:

To analyze the added mass and drag coefficients of the MaRINET2 semi-submersible floater when subjected to forced oscillatory motion using a validated CFD model.

The objective was generated from the following main research question, which was answered with the research findings.

How do a semi-submersible floater’s added mass and drag coefficients behave and vary under the influence of forced oscillatory motions with different amplitudes and frequencies?

The objective was achieved by developing a nonlinear Navier-Stokes numerical CFD model within the OpenFOAM software, utilizing the interFoam solver. The model was validated against experimental data from the UsO wave tank to ensure the result's accuracy. Subsequently, this validated CFD model was employed to calculate the semi-submersible floater's added mass and drag coefficients through forced oscillatory simulations. The main findings answering the main question of the behavior of the hydrodynamic parameters of the floater are outlined in the following points:

- The model was effectively validated against the UoS experiments' data using free decay simulations. The results comparison had a low error rate of less than 3% in predicting the natural period of pitch motion. Pitch motion had the highest prediction error among the three motion parameters tested.
- Through stiffness calibration testing, it was determined that the optimal stiffness value for the small mooring system used to validate the model is 21.1N/m.
- Heave added mass coefficients were found to be sensitive to both oscillation amplitude and period, with coefficients increasing as both parameters increased. Drag coefficients, on the other hand, had a relatively low influence on shorter periods but showed an increase at longer periods, possibly due to outlier data points. Also, heave drag coefficients presented a trend where higher amplitudes were associated with lower coefficients.
- Surge added mass coefficients exhibited a dependence on the oscillation period, with longer periods resulting in higher coefficients. Additionally, these coefficients increased with higher oscillation amplitudes. The first trend in surge added mass coefficients agreed with a reference paper, but the second trend was opposite to that paper's findings.
- For high amplitude oscillations, surge drag coefficients remained relatively constant regardless of the oscillation period. However, longer periods increased coefficient values for mid and low amplitudes, showing that surge drag coefficients generally depended on oscillation time except for high amplitudes.
- Pitch-added mass coefficients were found to be unaffected by oscillation amplitude but increased with longer periods.
- The Pitch drag coefficient exhibited a significant increase in the 25-second data set, corresponding to the pitch motion's natural frequency. Also, it was seen that pitch drag coefficients decrease if oscillation amplitude increases.

In conclusion, this report presents a validated CFD numerical setup suitable for both free decay and forced oscillation simulations. It conducts a mesh convergence study to identify the optimal mesh configuration that balances computational resources while maintaining result accuracy. Moreover, the report provides an extensive analysis of the hydrodynamic characteristics of the MaRINET2 SS floater subjected to different oscillation amplitudes and periods. These hydrodynamic parameters are then compared with those from two distinct reference papers, revealing notable similarities as well as some discrepancies in the trends. It is challenging to attribute these deviations to differences in floater geometry or simulation accuracy, particularly since the reference papers focus on a very different SS floater. The comparison was performed against these two reference papers due to the lack of experimental data for our floater. To enhance the analysis, more detailed information about the current floater is essential. Therefore, the subsequent section offers recommendations for future research to facilitate further investigation and more meaningful comparisons.

6.3. Recommendations

This section outlines recommendations for future research aimed at enhancing the insights and robustness of the findings in this project. These recommendations have a range of areas, from improving the understanding of mooring lines' dynamics to conducting more detailed simulations and gathering additional data for the MaRINET2 SS floater. With these recommendations, researchers can contribute to a deeper understanding of the hydrodynamic behavior of FOWT structures.

- **Model Mooring Lines with a Dynamic Model:** A first recommendation for future work is to explore the use of a dynamic model to simulate mooring lines. This would provide a better understanding of

their dynamics and their impact on the SS floater. Comparative analysis with the current static model can reveal significant insights into the system's behavior.

- **More Detailed Mesh Convergence Study:** While the existing mesh convergence study yielded valuable insights, it is advisable to conduct a more detailed analysis. This could involve optimizing mesh quality to balance percent error against simulation time. Such a study would provide a deeper understanding of how mesh refinement impacts accuracy in CFD numerical models.
- **Waves Simulation:** To better understand the drag behavior near the air-water interface, it is recommended to conduct a series of different wave simulations. These simulations can provide insights into how wind-generated waves affect the hydrodynamic characteristics of the SS floater near the air-water interface.
- **Pitch Free Decay Test:** Given that pitch motion presents challenges during this report, conducting additional pitch free decay simulations can enhance the understanding of this particular motion. Insights into pitch behavior contribute to a more comprehensive analysis of the SS floater's dynamics.
- **Surge Simulations:** To address the observed discrepancy in surge added mass trends compared to other reports, it is important to conduct more surge simulations. Varying oscillation amplitudes and periods can help to find the factors influencing this behavior and provide clarity on the observed trends. And clarify if the differences are caused by the floater geometry difference or by a numerical challenge.
- **Heave Simulations:** To support the observed behavior of heave drag coefficients, it is recommended to conduct additional heave simulations with varying time periods. This will help determine whether the trend towards higher coefficients at T=50s is consistent or if it may be attributed to outlier data points.
- **Gather More Information from the Specific SS Floater:** The primary recommendation is to gather additional data and results for the MaRINET2 SS floater for comparison and validation purposes. Two viable approaches include utilizing a mid-fidelity numerical method like PFT in combination with the Morrison equation for comparative analysis and conducting further experimental research on the floater. These will enhance the reliability of the findings and strengthen the overall value of this report.
- **Validate the hydrodynamic coefficients obtained:** perform experiments with the MaRINET2 SS floater to validate the obtained coefficients and also obtain the coefficients for the natural frequency with the free decay tests and compare them.

These recommendations collectively aim to advance the understanding of the MaRINET2 SS floater's hydrodynamic behavior, contribute to the knowledge in this field, and facilitate more accurate comparisons and analysis in future research.

References

[1] Bin Chen et al. *Pathways for sustainable energy transition*. Aug. 2019. DOI: 10.1016/j.jclepro.2019.04.372.

[2] IPCC. *AR6 Synthesis Report: Climate Change 2023 — IPCC*. Mar. 2023. URL: https://www.ipcc.ch/report/sixth-assessment-report-cycle/.

[3] UNFCCC. *Paris Agreement*. Dec. 2015. URL: https://unfccc.int/sites/default/files/english_paris_agreement.pdf.

[4] United Nations. *THE 17 GOALS | Sustainable Development*. 2015. URL: https://sdgs.un.org/goals.

[5] Gabriela Ileana Iacobuță et al. "Aligning climate and sustainable development finance through an SDG lens. The role of development assistance in implementing the Paris Agreement". In: *Global Environmental Change* 74 (May 2022). DOI: 10.1016/j.gloenvcha.2022.102509.

[6] IEA. *Wind Electricity*. Tech. rep. Paris: IEA, 2022. URL: https://www.iea.org/reports/wind-electricity.

[7] GWEC et al. "Global Wind Report 2021". In: *Global Wind Energy Council* (Jan. 2022). URL: https://gwec.net/global-wind-report-2021/.

[8] GWEC. *Global Wind Report 2022*. Tech. rep. Brussels, 2022. URL: https://gwec.net/global-wind-report-2022/.

[9] Gordon Stewart et al. "Aerodynamic Simulation of the MARINTEK Braceless Semisubmersible Wave Tank Tests". In: *Journal of Physics: Conference Series*. Vol. 749. 1. Institute of Physics Publishing, Sept. 2016. DOI: 10.1088/1742-6596/749/1/012012.

[10] Gordon Stewart et al. "A Review and Comparison of Floating Offshore Wind Turbine Model Experiments". In: *Energy Procedia*. Vol. 94. Elsevier Ltd, 2016, pp. 227–231. DOI: 10.1016/j.egypro.2016.09.228.

[11] I Bayati et al. "The effects of second-order hydrodynamics on a semisubmersible floating offshore wind turbine". In: *Journal of Physics: Conference Series* 524.1 (June 2014), p. 012094. DOI: 10.1088/1742-6596/524/1/012094. URL: https://iopscience.iop.org/article/10.1088/1742-6596/524/1/012094%20https://iopscience.iop.org/article/10.1088/1742-6596/524/1/012094/meta.

[12] Lu Wang et al. "OC6 phase I: Improvements to the OpenFAST predictions of nonlinear, low-frequency responses of a floating offshore wind turbine platform". In: *Renewable Energy* 187 (Mar. 2022), pp. 282–301. DOI: 10.1016/J.RENENE.2022.01.053.

[13] Lu Wang et al. "OC6 Phase Ia: CFD Simulations of the Free□Decay Motion of the DeepCwind Semisubmersible". In: *Energies* 15.1 (Jan. 2022). DOI: 10.3390/en15010389.

[14] SSE Renewables. *World's deepest offshore wind turbine foundation installed in Scottish waters*. Apr. 2023. URL: https://www.sserenewables.com/news-and-views/2023/04/world-s-deepest-offshore-wind-turbine-foundation-installed-in-scottish-waters/#:~:text=The%5C%20installation%5C%20of%5C%20the%5C%20jacket,a%5C%20depth%5C%20of%5C%2058.6%5C%20metres..

[15] Jean-Paul Ducrotoy et al. *The North Sea*. Tech. rep. 2000, pp. 5–23. URL: https://www.sciencedirect.com/science/article/pii/S0025326X00000990.

[16] S Butterfield et al. *Engineering Challenges for Floating Offshore Wind Turbines*. Tech. rep. 2007. URL: https://www.osti.gov/biblio/917212.

[17] Gordon R. Fulton et al. “Design of a semi-submersible platform for a 5MW wind turbine”. In: *Collection of Technical Papers - 44th AIAA Aerospace Sciences Meeting*. Vol. 16. AIAA International, 2006, pp. 11943–11963. DOI: 10.2514/6.2006-997.

[18] W Musial et al. *Feasibility of Floating Platform Systems for Wind Turbines: Preprint*. Tech. rep. 2004. URL: http://www.osti.gov/bridge.

[19] Matthew Lackner. “How Do Floating Wind Turbines Work?” In: (Dec. 2022). URL: https://www.oedigital.com/news/501527-how-do-floating-wind-turbines-work.

[20] J. R. Browning et al. “Calibration and validation of a spar-type floating offshore wind turbine model using the FAST dynamic simulation tool”. In: *Journal of Physics: Conference Series*. Vol. 555. 1. Institute of Physics Publishing, 2014. DOI: 10.1088/1742-6596/555/1/012015. URL: https://www.researchgate.net/publication/285926032_Calibration_and_validation_of_a_spar-type_floating_offshore_wind_turbine_model_using_the_FAST_dynamic_simulation_tool.

[21] John Marius Hegseth et al. “Integrated design optimization of spar floating wind turbines”. In: *Marine Structures* 72 (July 2020). DOI: 10.1016/j.marstruc.2020.102771. URL: https://www.sciencedirect.com/science/article/pii/S0951833920300654.

[22] Jochem Tacx. *Floating Wind Structures and Mooring Types; Energy Facts*. Apr. 2022. URL: https://www.energyfacts.eu/floating-wind-structures-and-mooring-types/.

[23] G R Fulton et al. *Semi-Submersible Platform and Anchor Foundation Systems for Wind Turbine Support*. Tech. rep. 2005. URL: http://www.osti.gov/bridge.

[24] Sebastien Gueydon et al. “Round robin laboratory testing of a scaled 10 mw floating horizontal axis wind turbine”. In: *Journal of Marine Science and Engineering* 9.9 (Sept. 2021). DOI: 10.3390/jmse9090988. URL: https://www.mdpi.com/2077-1312/9/9/988.

[25] John Nicholas Newman. *Marine Hydrodynamics*. 1999.

[26] Aaron Du. *Floating Wind. Semi-Submersible, Spar, TLP - How to select floating wind foundation types?* Aug. 2021. URL: https://www.empireengineering.co.uk/semi-submersible-spar-and-tlp-floating-wind-foundations/.

[27] Thanh Toan Tran et al. “The coupled dynamic response computation for a semi-submersible platform of floating offshore wind turbine”. In: *Journal of Wind Engineering and Industrial Aerodynamics* 147 (Dec. 2015), pp. 104–119. DOI: 10.1016/j.jweia.2015.09.016.

[28] Alessandro Bettini. *A Course in Classical Physics 2, Fluids and Thermodynamics*. 2016.

[29] Irene Rivera-Arreba. “Computation of Nonlinear Wave Loads on Floating Structures (MSc thesis)”. In: *TU Delft University* August (2017), p. 105.

[30] Soumya Chakraborty. “Ship stability; introduction to hydrostatics and stability of surface ships”. In: *Marine Insight* (Feb. 2022). URL: https://www.marineinsight.com/naval-architecture/ship-stability-introduction-hydrostatics-stability-surface-ships/.

[31] DNV AS. *Support structures for wind turbines DNV AS*. Tech. rep. 2021.

[32] Ian R. Young. *Wind Generated Ocean Waves*. 1999.

[33] Victor Shrira et al. “Potential Wave Theory, Instability of Wave Trains”. In: *Encyclopedia of Maritime and Offshore Engineering*. John Wiley & Sons, Ltd, Apr. 2017, pp. 1–11. DOI: 10.1002/9781118476406.emoe072.

[34] Edwin Frank George van Daalen. *Numerical and theoretical studies of water waves and floating bodies*. s.n.], 1993.

[35] Matthieu Parenteau et al. “Nonlinear frequency-domain solver for vortex lattice method”. In: *AIAA Journal* 56.6 (2018), pp. 2242–2251. DOI: 10.2514/1.J056704.

[36] Nallayarasu Seeninaidu et al. “Hydrodynamic response of spar hulls with heave damping plate using simplified approach”. In: *Ships and Offshore Structures* 9 (June 2014). DOI: 10.1080/17445302.2013.841331.

[37] Marek Jaszczur et al. *A general review of the current development of mechanically agitated vessels*. Aug. 2020. DOI: 10.3390/PR8080982.

[38] José Azcona et al. “Aerodynamic thrust modelling in wave tank tests of offshore floating wind turbines using a ducted fan”. In: *Journal of Physics: Conference Series*. Vol. 524. 1. Institute of Physics Publishing, 2014. DOI: 10.1088/1742-6596/524/1/012089.

[39] Bonjun J. Koo et al. “Model tests for a floating wind turbine on three different floaters”. In: *Journal of Offshore Mechanics and Arctic Engineering* 136.2 (Mar. 2014). DOI: 10.1115/1.4024711.

[40] A Robertson et al. *Definition of the Semisubmersible Floating System for Phase II of OC4*. Tech. rep. 2014. URL: www.nrel.gov/publications..

[41] Irene Rivera-Arreba et al. “Modeling of a Semisubmersible Floating Offshore Wind Platform in Sev[1] I. Rivera-Arreba, N. Bruinsma, E. E. Bachynski, A. Viré, B. T. Paulsen, and N. G. Jacobsen, “Modeling of a Semisubmersible Floating Offshore Wind Platform in Severe Waves,” J. Offshor”. In: *Journal of Offshore Mechanics and Arctic Engineering* 141.6 (Dec. 2019). DOI: 10.1115/1.4043942. URL: http://asmedigitalcollection.asme.org/offshoremechanics/article-pdf/141/6/061905/6419647/omae_141_6_061905.pdf.

[42] Likhitha Ramesh Reddy et al. *Validation of CFD determined hydrodynamic coefficients for a semisubmersible floating offshore wind turbine*. Tech. rep. 2022.

[43] Romain Pinguet et al. *Validation of Open-Source Overset Mesh Method Using Free-Decay Tests of Floating Offshore Wind Turbine*. Oct. 2020. URL: www.isope.org.

[44] Romain Pinguet. “Hydrodynamics of semi-submersible floater for offshore wind turbines in highly nonlinear waves using Computational Fluid Dynamics (CFD), and validation of overset meshing technique in a numerical wave tank PhD Examination Committee :” in: (2021).

[45] Yuanchuan Liu. “A CFD Study of Fluid-Structure Interaction Problems for Floating Offshore Wind Turbines”. In: June (2018).

[46] Nimmy Philip et al. “Damping Characteristics of Heave Plates Attached to Spar Hull”. In: *Proceedings of the International Conference on Offshore Mechanics and Arctic Engineering - OMAE* 1 (July 2012). DOI: 10.1115/OMAE2012-83290.

[47] Shining Zhang et al. “Numerical study of hydrodynamic coefficients of multiple heave plates by large eddy simulations with volume of fluid method”. In: *Ocean Engineering* 163 (Sept. 2018), pp. 583–598. DOI: 10.1016/j.oceaneng.2018.03.060.

[48] Haoran Li et al. “Experimental and numerically obtained low-frequency radiation characteristics of the OC5-DeepCwind semisubmersible”. In: *Ocean Engineering* 232 (July 2021). DOI: 10.1016/j.oceaneng.2021.109130.

[49] Henrik Rusche. “Computational Fluid Dynamics of Dispersed Two-Phase Flows at High Phase Fractions”. PhD thesis. Jan. 2002.

[50] OpenFOAM. *User Guide: InterFoam*. URL: https://www.openfoam.com/documentation/guides/latest/doc/guide-applications-solvers-multiphase-interFoam.html.

[51] C W Hirt et al. *Volume of Fluid (VOF) Method for the Dynamics of Free Boundaries**. Tech. rep. 1981, pp. 201–225.

[52] OpenFOAM. *User Guide: Schemes*. URL: https://www.openfoam.com/documentation/guides/latest/doc/guide-schemes.html.

[53] Paula Doubrawa et al. “Load response of a floating wind turbine to turbulent atmospheric flow”. In: *Applied Energy* 242 (May 2019), pp. 1588–1599. DOI: 10.1016/j.apenergy.2019.01.165.

[54] M. Somoano et al. “Influence of turbulence models on the dynamic response of a semi-submersible floating offshore wind platform”. In: *Ocean Engineering* 237 (Oct. 2021). DOI: 10.1016/j.oceaneng.2021.109629.

[55] Thanh Toan Tran et al. “Fully coupled aero-hydrodynamic analysis of a semi-submersible FOWT using a dynamic fluid body interaction approach”. In: *Renewable Energy* 92 (July 2016), pp. 244–261. DOI: 10.1016/j.renene.2016.02.021.

[56] F. R. Menter. “Two-equation eddy-viscosity turbulence models for engineering applications”. In: *AIAA Journal* 32.8 (1994), pp. 1598–1605. DOI: 10.2514/3.12149.

[57] OpenFOAM. *5.3 Turbulence models*. 2022. URL: https://www.openfoam.com/documentation/user-guide/5-models-and-physical-properties/5.3-turbulence-models.

[58] OpenFOAM. *4.4 Mesh generation with the snappyHexMesh utility*. URL: https://www.openfoam.com/documentation/user-guide/4-mesh-generation-and-conversion/4.4-mesh-generation-with-the-snappyhexmesh-utility.

[59] M. Islam et al. “Data analysis methodologies for hydrodynamic experiments in waves”. In: *Journal of Naval Architecture and Marine Engineering* 13.1 (2016), pp. 1–15. DOI: 10.3329/jname.v13i1.25347.

Appendix A

This appendix contains the extra figures of the mesh.

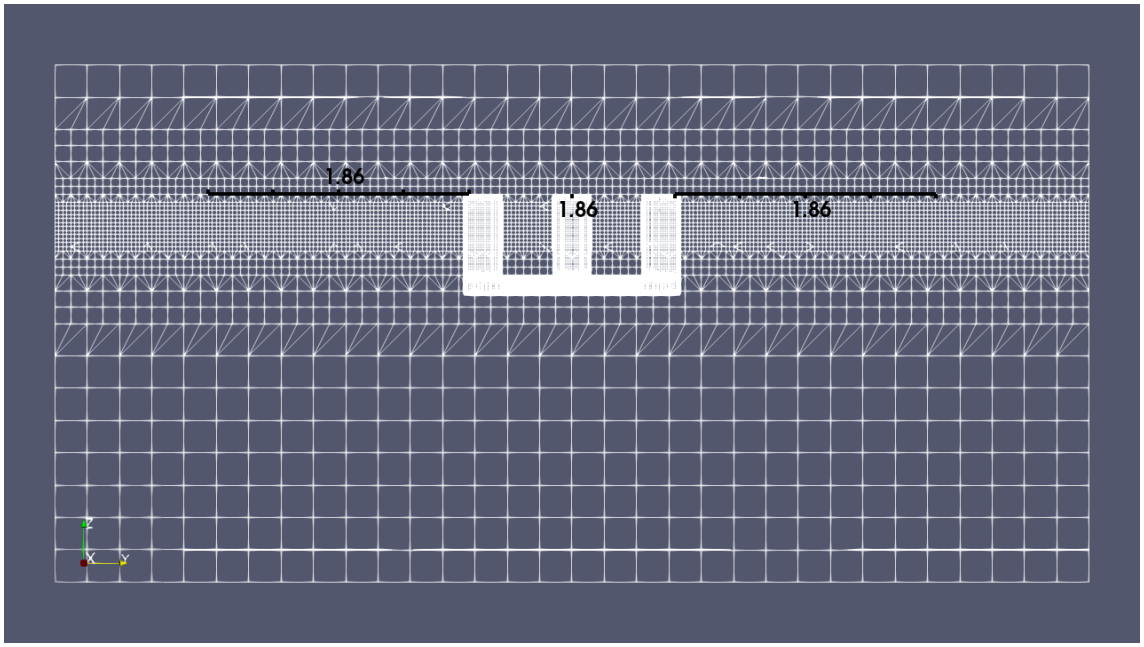

Figure A.1: Mesh with the representation of the mooring lines, yz plane view.

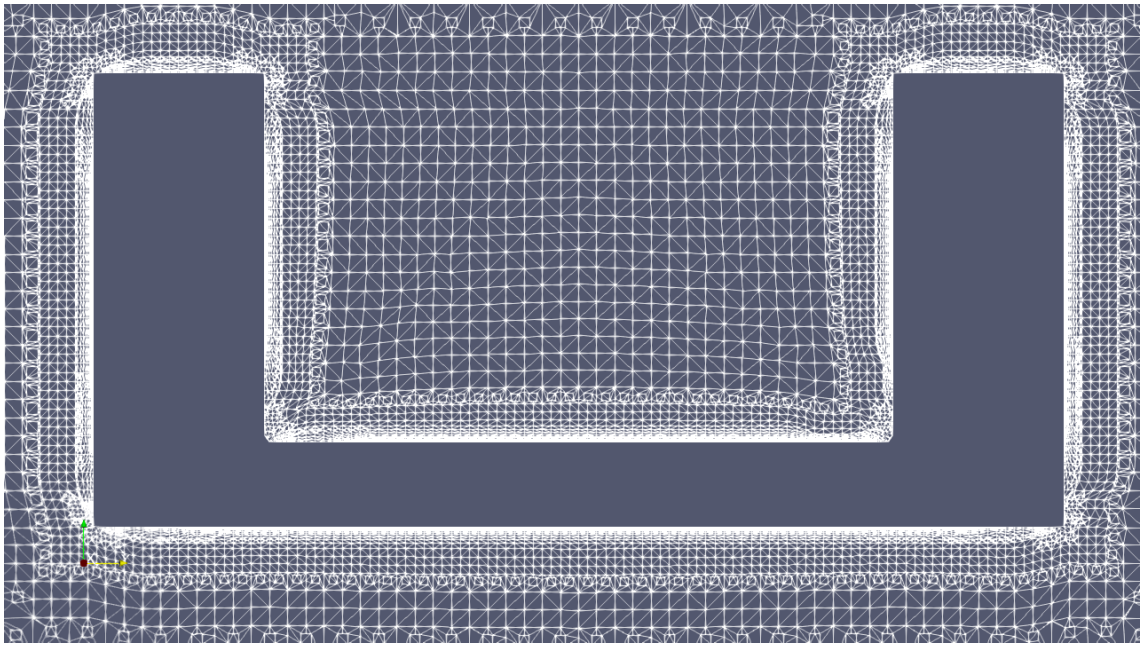

Figure A.2: Mesh closeup to the back heave plate, yz plane view.

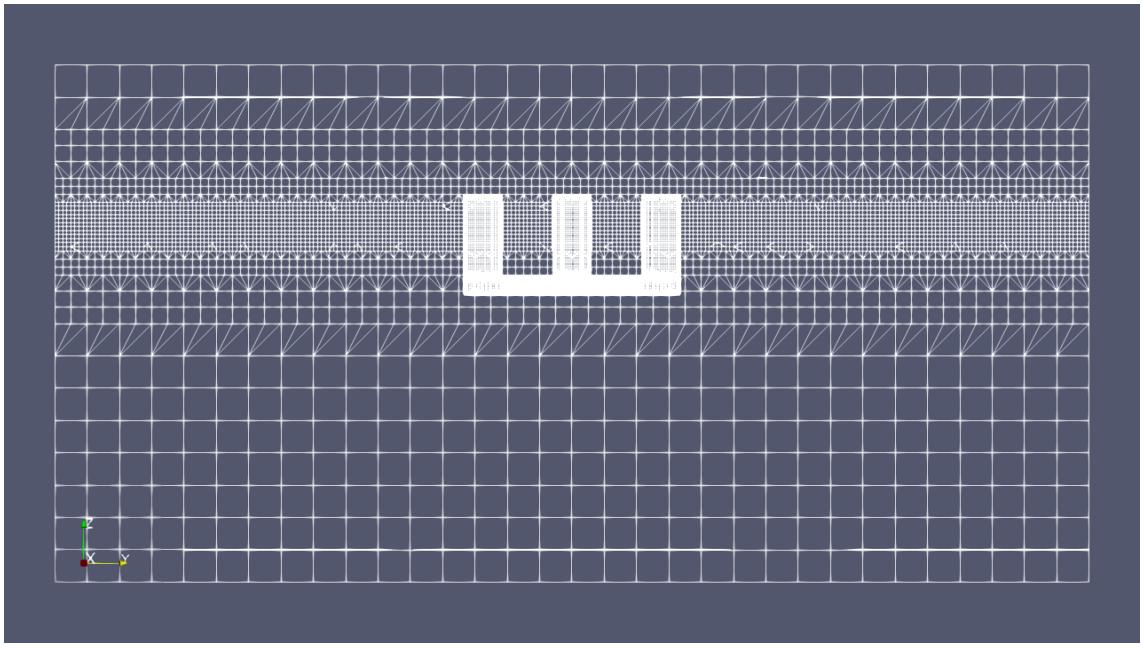

Figure A.3: Mesh, yz plane view.

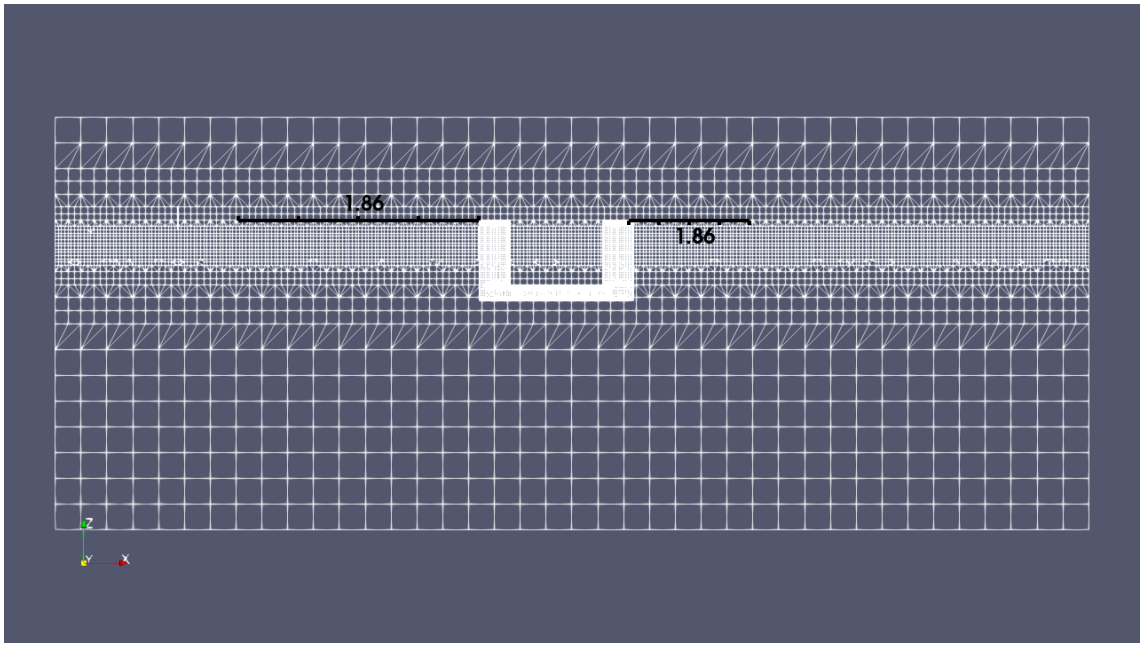

Figure A.4: Mesh with the representation of the mooring lines, xz plane view.

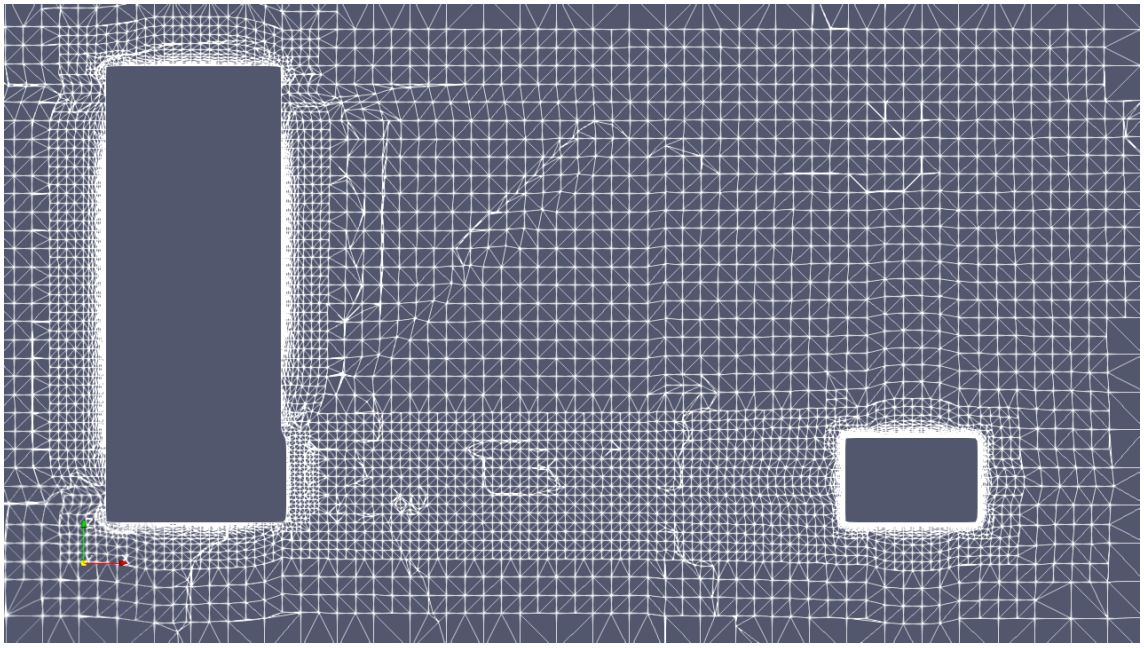

Figure A.5: Mesh closeup to the center of the floater, xz plane view.

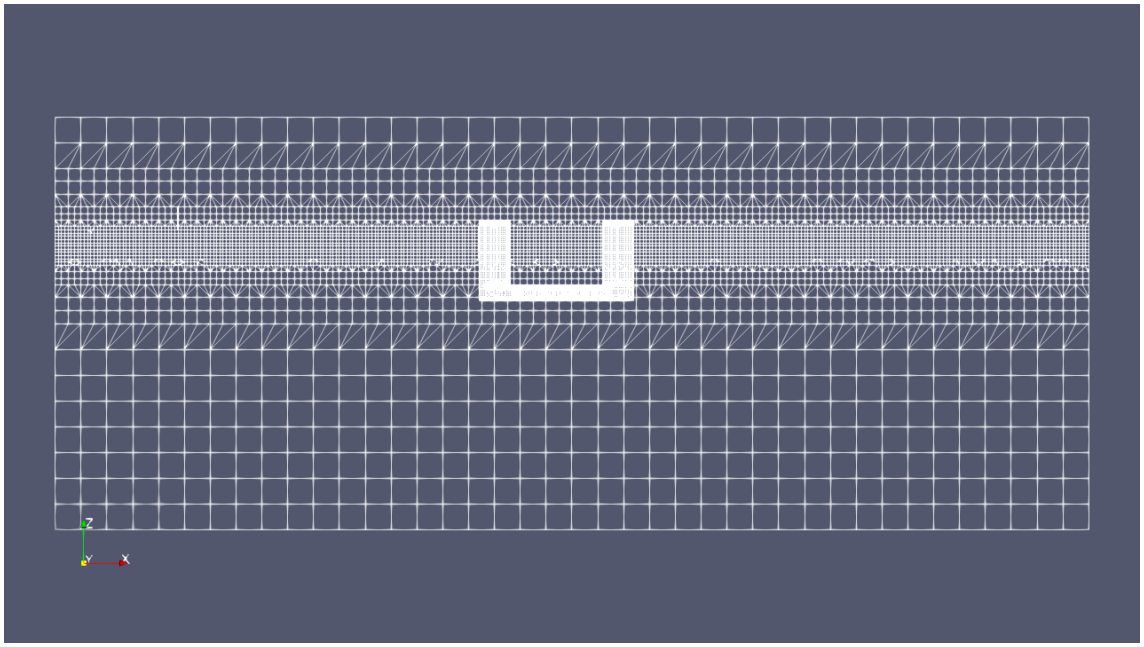

Figure A.6: Mesh, xz plane view.

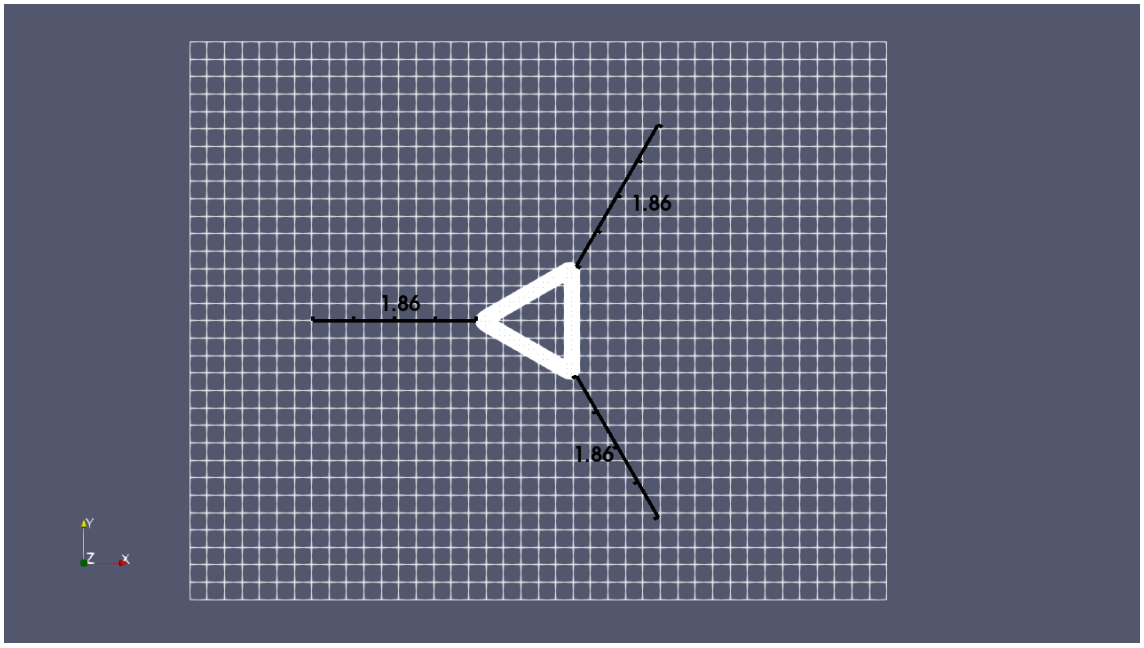

Figure A.7: Mesh with the representation of the mooring lines, aerial view, xy plane view.

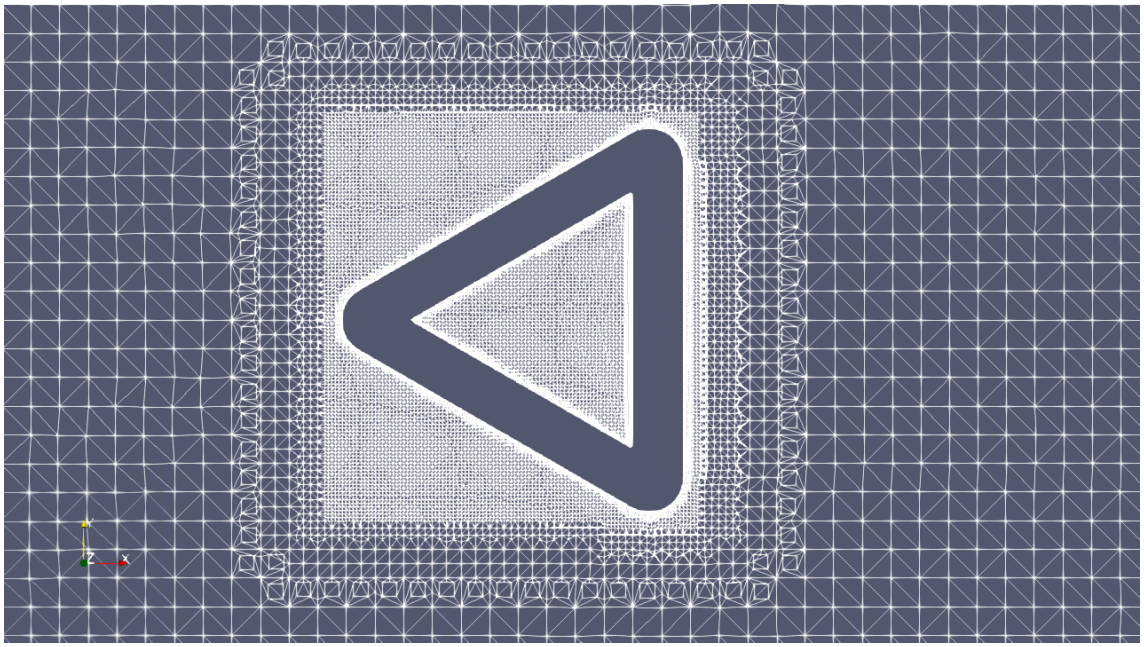

Figure A.8: Mesh closeup to the bottom of the floater, xy plane view.

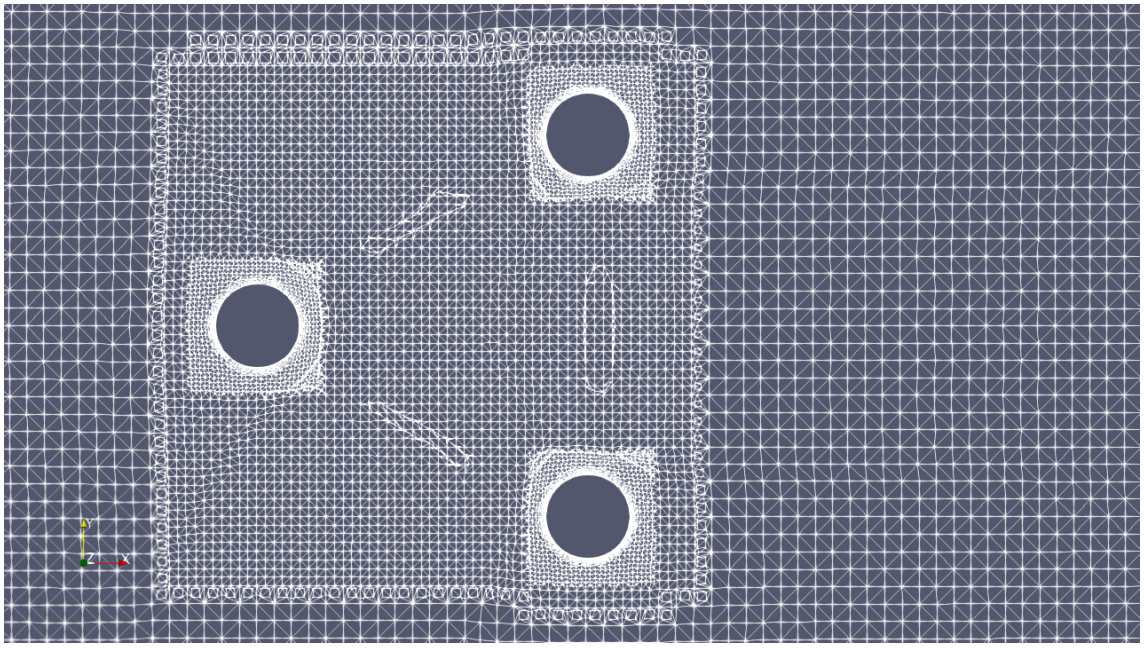

Figure A.9: Mesh closeup to the floater at the SWL, xy plane view.

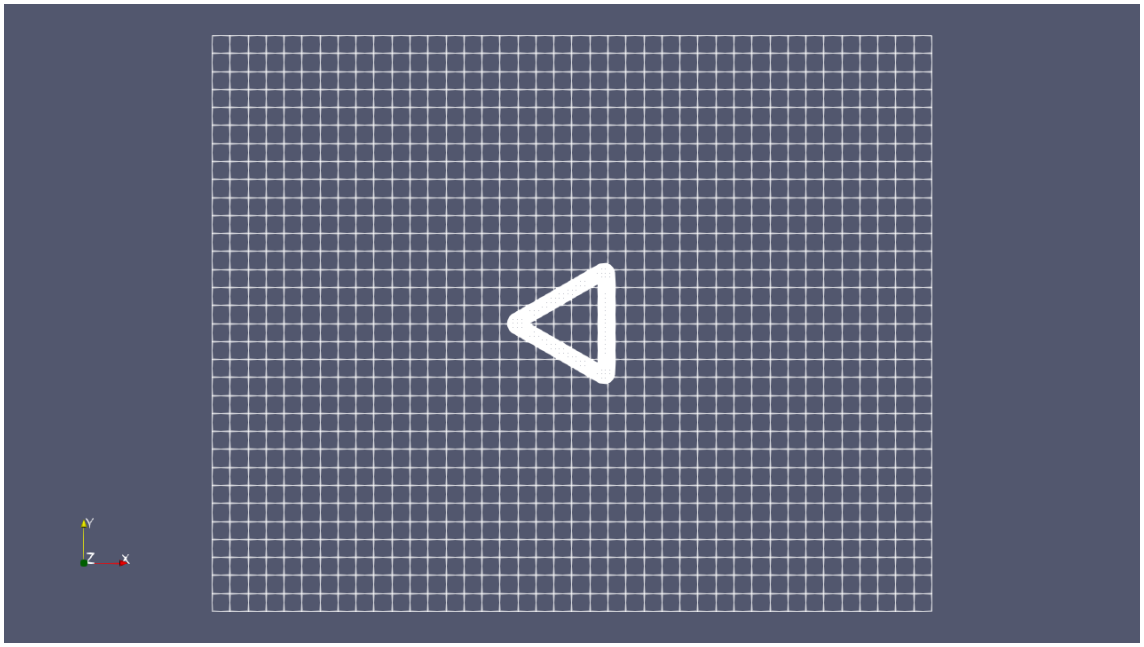

Figure A.10: Aerial view of the mesh, xy plane view.

B

Appendix B

This appendix contains the extra figures of the mesh convergence study.

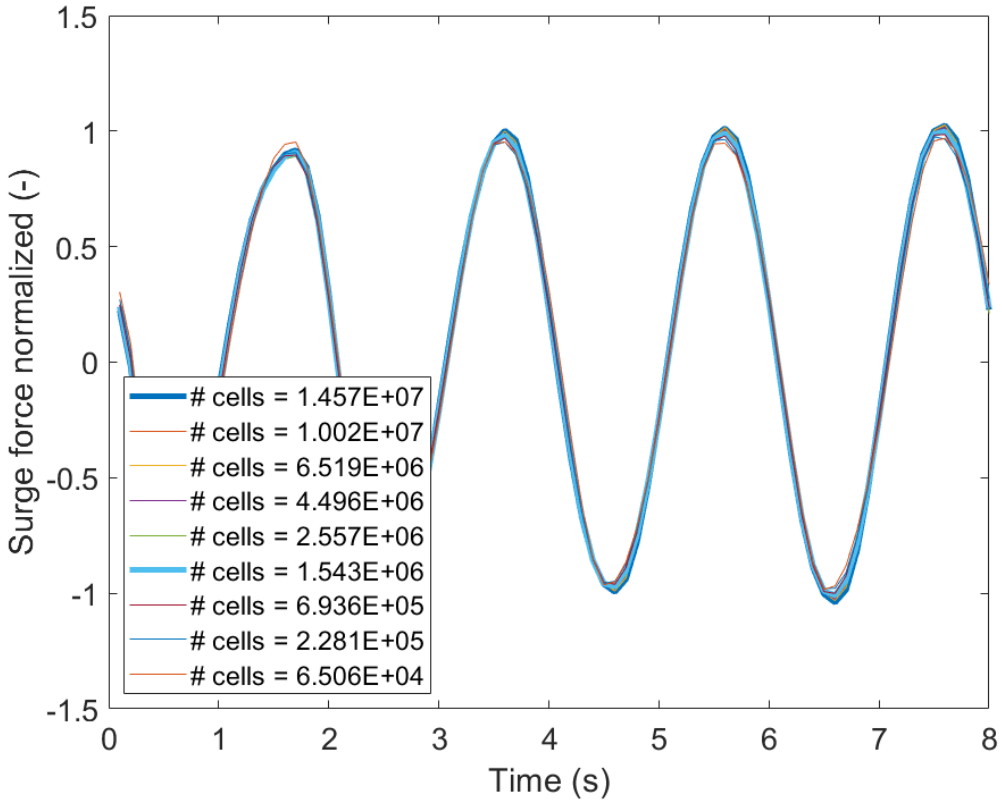

Figure B.1: Surge mesh convergence simulations

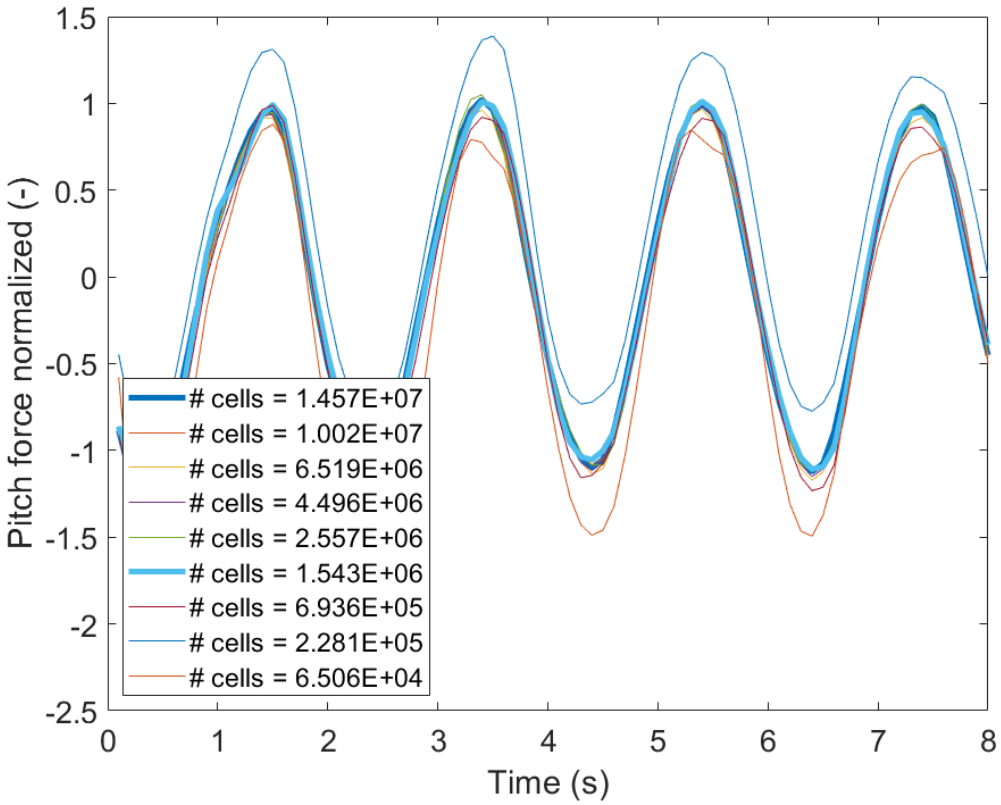

Figure B.2: Pitch mesh convergence simulations